Towards a mechanistic understanding of the palaeoclimatological proxy δ^{13}C in benthic foraminifera

Vom Fachbereich für Physik und Elektrotechnik

der Universität Bremen

zur Erlangung des akademischen Grades eines

Doktor der Naturwissenschaften (Dr. rer. nat.)

genehmigte Dissertation

von

Tilman Hesse

geb. in Hamburg

1. Gutachter:	Prof. Dr. Gerrit Lohmann
2. Gutachter:	Prof. Dr. Dieter Wolf-Gladrow

Eingereicht am:	14. Februar 2013
Tag des Promotionskolloquiums:	8. Mai 2013

Abstract

The proxy δ^{13}C as derived from benthic foraminiferal shells is widely used by palaeoceanographers to reconstruct the distribution of past water masses. The biogeochemical processes involved in forming the benthic foraminiferal δ^{13}C signal ($\delta^{13}C_{foram}$), however, have not been fully understood yet, and a sound mechanistic description is still lacking. This thesis attempts to make progress towards the long-standing goal of a mechanistic understanding and description of δ^{13}C in benthic foraminifera. Furthermore, the still debated state of the glacial ocean circulation and water mass distribution is assessed using δ^{13}C.

First, a compilation of 220 sediment core δ^{13}C reconstructions from the glacial Atlantic Ocean is compared with three-dimensional ocean circulation simulations including a marine carbon cycle model. Second, a reaction-diffusion model for calcification in foraminifera is adapted for the use in benthic foraminifera. This model is able to quantify the effects of different physical, chemical and biological processes on the δ^{13}C signal of an idealised benthic foraminiferal shell ($\delta^{13}C_{foram}$). Sensitivity experiments with the stand-alone calcification model are performed. Third, the three-dimensional ocean circulation simulations are used to drive the foraminifera calcification model in order to have a spatial representation of $\delta^{13}C_{foram}$ in the glacial ocean. The results are employed in another model-data comparison in the glacial Atlantic Ocean.

The ocean model captures the general δ^{13}C pattern indicated by present-day water column data and Late Holocene sediment cores, but underestimates intermediate and deep water values in the South Atlantic. The best agreement with glacial reconstructions is obtained for a model scenario with an altered freshwater balance in the Southern Ocean, which has a shoaled and weakened North Atlantic Deep Water flow and intensified Antarctic Bottom Water export. Results from the foraminifera calcification model indicate that temperature, respiration rate, and pH have a significant impact on $\delta^{13}C_{foram}$. The results from the coupled ocean circulation/carbon cycle model and the foraminifera calcification model improve the correlation with glacial recon-

structions for all simulations considered. Knowledge of vital parameters such as the respiration rate are important for constraining uncertainties in the formation of the $\delta^{13}C_{foram}$ signal.

The results show that an interdisciplinary approach to assessing palaeoclimate is both valuable and useful for advancing our understanding of the climate system.

Acknowledgements

This thesis would not have been possible without the support of a lot of people. First of all I would like to thank Gerrit Lohmann for his on-going support, guidance and good humour during the PhD project. I would also like to thank Dieter Wolf-Gladrow for his continued support and commitment. Thanks to all my co-authors for their help, contributions and fruitful discussions (be it in English oder auf deutsch): Andreas Mackensen, Dieter Wolf-Gladrow, Gerrit Lohmann, Jelle Bijma, Martin Butzin, Richard Zeebe, and Torsten Bickert. I'd also like to thank Peter Köhler, Lennart de Nooijer, Martin Glas and Nina Keul for sharing their insights on δ^{13}C and benthic foraminifera. I am indebted to Claudia Hanfland, Claudia Sprengel, Dörte Burhop, Jelle Bijma, and POLMAR as a whole: they made life a lot easier by running such a fantastic graduate school and allowing me to participate in numerous conferences, workshops, soft skill trainings, PhD Days, etc. I would like to thank the Palaeoclimate Dynamics group members (past and present) for all the lunches, group meetings, discussions, and Christmas market visits. I would also like to thank Wolfgang Cohrs and the Rechenzentrum for their on-going technical support. I am extremely grateful to Eberhard Fahrbach, Gerd Rohardt and Gerrit Lohmann for making it possible to be part of ANTXXVII/2, a cruise I am not going to forget. Special thanks to my DokTeam colleagues Judith, Nina, Shuang, Thomas and Xiaoping for being such a great team with lots of good ideas and the stamina to see them through. Finally, thank you to my friends, family and Annalena.

Contents

Chapter 1

Introduction

In 1990 the Intergovernmental Panel on Climate Change (IPCC) published its first assessment report [IPCC , 1990], which firmly established the issue of a changing climate on the political and scientific agendas. Understanding the complex climate system with its many different components and interactions (see Figure 1.1) and predicting its future behaviour is of immense importance to mankind. In order to understand how the system functions and to be able to predict its behaviour, climate scientists have traditionally taken two approaches. On the one hand, they have formulated models of the climate system, that try to capture all the physical, chemical and biological processes involved. In parallel with increasing computer power these models have increased dramatically in complexity over the years, from simple atmospheric and ocean box models to highly complex coupled Earth system models, that not only include atmospheric and oceanic components, but also land ice, sea ice, vegetation, and sediment components, to name but a few. On the other hand, climate scientists have looked into the historical and geological past, where there is a wealth of data allowing us to reconstruct past changes of the climate system. Models are what climate scientists use for predicting future climate changes. In order to proof the quality of any given model, it should pass the test of (geological) history. This is where the

two approaches for understanding the climate system meet: modellers make use of observation-based climate reconstructions in order to verify their models' abilities, while data gatherers rely on model output in order to test the feasibility of their reconstruction-based hypotheses. A third and more recent approach includes the validation of proxies (see below) in laboratory studies. In the laboratory, proxy signal formation can be tested under controlled conditions in sensitivity experiments. The results can then be used to constrain the interpretation of proxy material from the geological past.

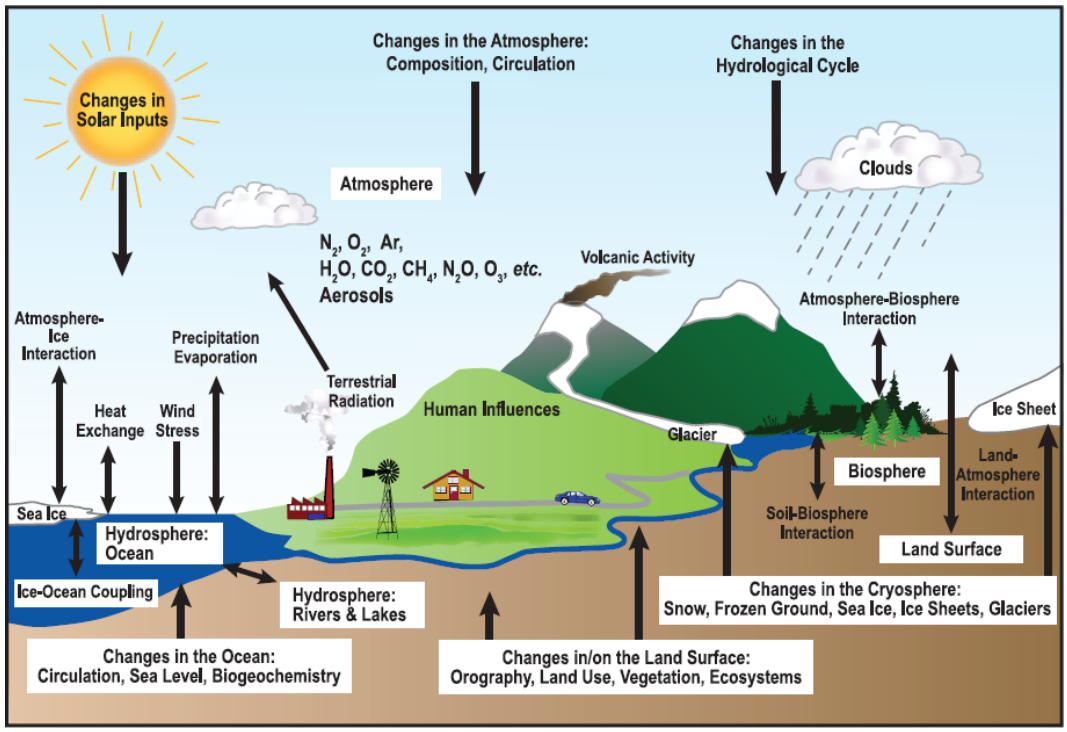

Figure 1.1: Components and interactions of the climate system, after IPCC [2007].

Palaeoclimatology

Climate reconstructions face the problem that, as we go back in time, less and less data is available. We know from instrumental records what happened in the last 100 to 150 years, for instance from thermometers measuring temperature. Going further back in time where there are no in-

strumental records, we have to rely on observations that have been recorded in books, sometimes very precisely as, for example, in the field of phenology where the blooming, flowering and wilting of certain plants has been recorded for centuries, which allows for a semi-quantitative assessment of temperature. Even further back in time, we can make use of the ratio of oxygen isotopes in order to reconstruct temperatures with the help of a so-called transfer function. A transfer function translates the original signal (here temperature) into a signal that is preserved in the geological record (here δ^{18}O), which can be measured at a later point in time. This is an example of a so-called proxy.

Proxies

Proxies are indicators of certain not directly measurable parameters such as temperature, carbon dioxide (CO_2) levels, or the distribution of water masses in the ocean. Tree rings, for instance, are a proxy for temperature, stomatal density on plant leaves is a proxy for CO_2 levels, and the ratio of carbon-13 (^{13}C) to carbon-12 (^{12}C), written as δ^{13}C, is among other things a proxy for the distribution of water masses in the ocean. The focus of this thesis is on δ^{13}C.

$\boldsymbol{\delta^{13}}$C

The proxy δ^{13}C is an indicator not only of the distribution of water masses in the past, but also of nutrient availability in the oceans. It is measured on shells of calcium carbonate-forming organisms such as foraminifera. One advantage of δ^{13}C is that it is widely available, both in space and in time. Thus, it is a popular proxy as it is possible to reconstruct large scale patterns in the ocean as well as their evolution through time. Since the oceans are a major component of the climate system, acting as one of the largest reservoirs for both heat and carbon (Figure 1.2), understanding their behaviour is of critical importance for understanding the climate system as a whole.

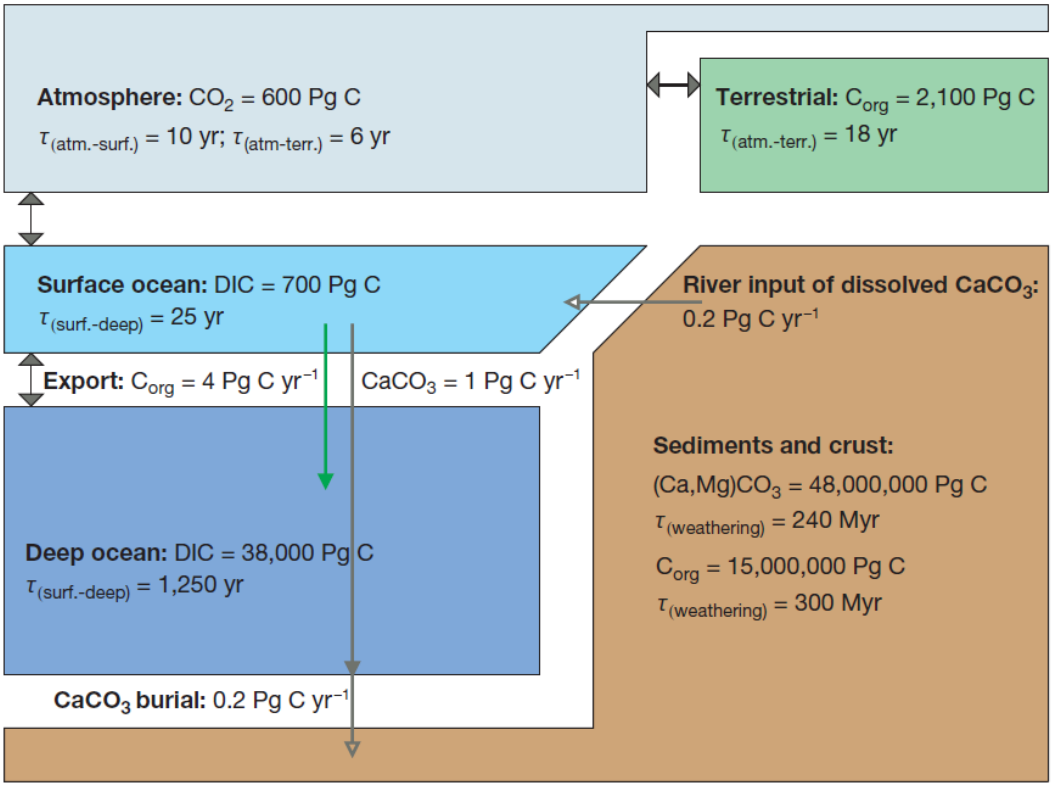

Figure 1.2: Carbon reservoirs and residence times of the climate system, after Sigman and Boyle [2000].

Ocean circulation

The observed ocean circulation at the present day is characterised by circulation of currents at the surface and circulation of intermediate, deep and bottom waters at depth (Figure 1.3). Drivers of the ocean circulation are (1) the wind stress at the surface, which mostly affects the surface ocean circulation, but can also link the deep ocean with the surface by Ekman-induced upwelling, (2) changes in the density of the ocean waters, e.g. due to changes in the thermohaline properties of the seawater, and (3) diapycnal mixing (i.e. mixing across density gradients) caused by bottom currents that flow across rough topography on the seafloor (e.g. Garabato et al. [2004]).

The global ocean circulation in simple terms is often described as a huge conveyor belt that, starting in the North Atlantic, transports cold and saline waters at depth southwards until it joins

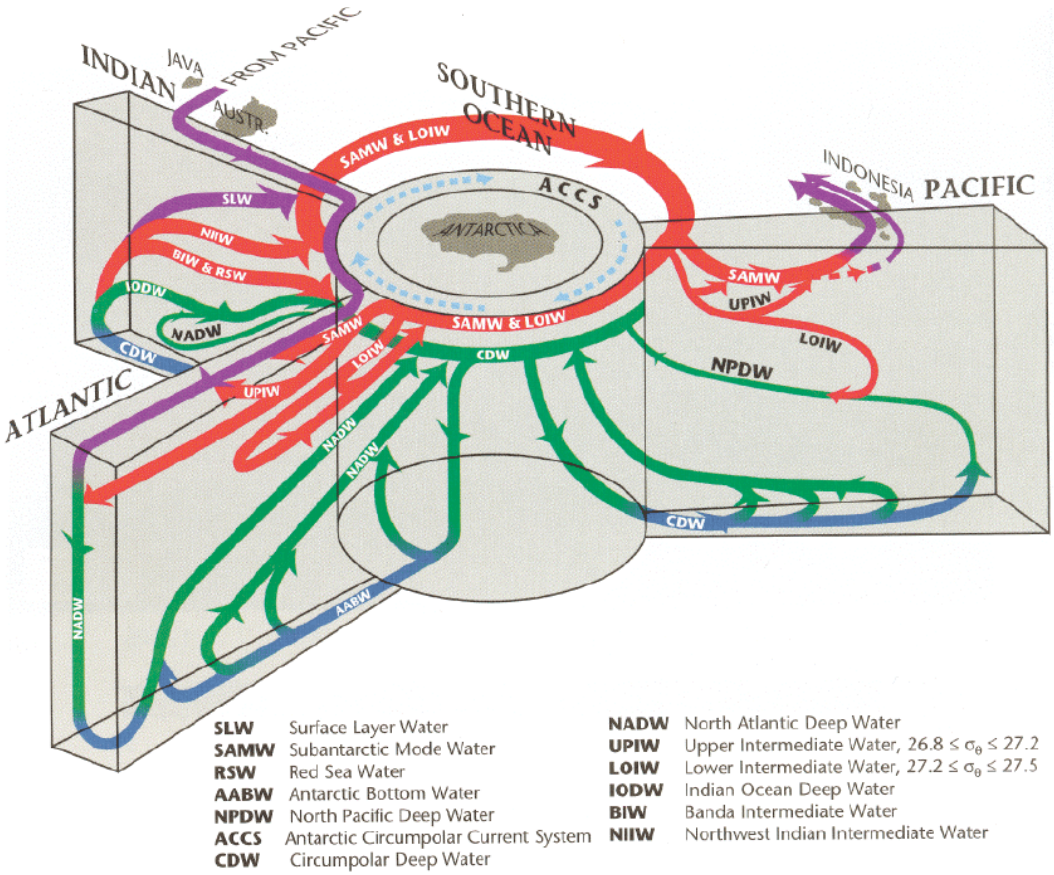

Figure 1.3: A schematic representation of the water mass flow paths in the world oceans. In this representation the Atlantic, Pacific and Indian Ocean all hinge on the Southern Ocean's Antarctic Circumpolar Current (ACC). All ocean basins are filled by Antarctic Bottom Waters (AABW) at depth. Note that deep water formation only occurs in the North Atlantic Ocean and in the Southern Ocean. Adapted from Schmitz [1996].

the Antarctic Circumpolar Current (ACC) from where it is transported northwards into the Indian and Pacific Ocean basins, still at depth, before it is then rising up to the surface where it warms. Then, following the Pacific branch, it is transported westwards at the surface via the Indonesian archipelago, the Indian Ocean, around the southern tip of Africa and then northwards into the Atlantic Ocean following the known surface currents back to its original setting in the North Atlantic (Figure 1.3). The notion of a conveyor belt was first introduced by Wally Broecker [Broecker and Peng, 1982]. It was originally based on the observations gathered during the Geochemical Ocean Sections Study (GEOSECS) campaigns. One feature of the conveyor belt is that

over time North Atlantic Deep Water (NADW), after leaving the surface, becomes more depleted in oxygen, while at the same time becoming more enriched in CO_2. This process is called water mass aging and can be traced using δ^{13}C, as was first done by Kroopnick [1985]. Figure 1.4 shows the δ^{13}C distribution of dissolved inorganic carbon (DIC) in the Western Atlantic.

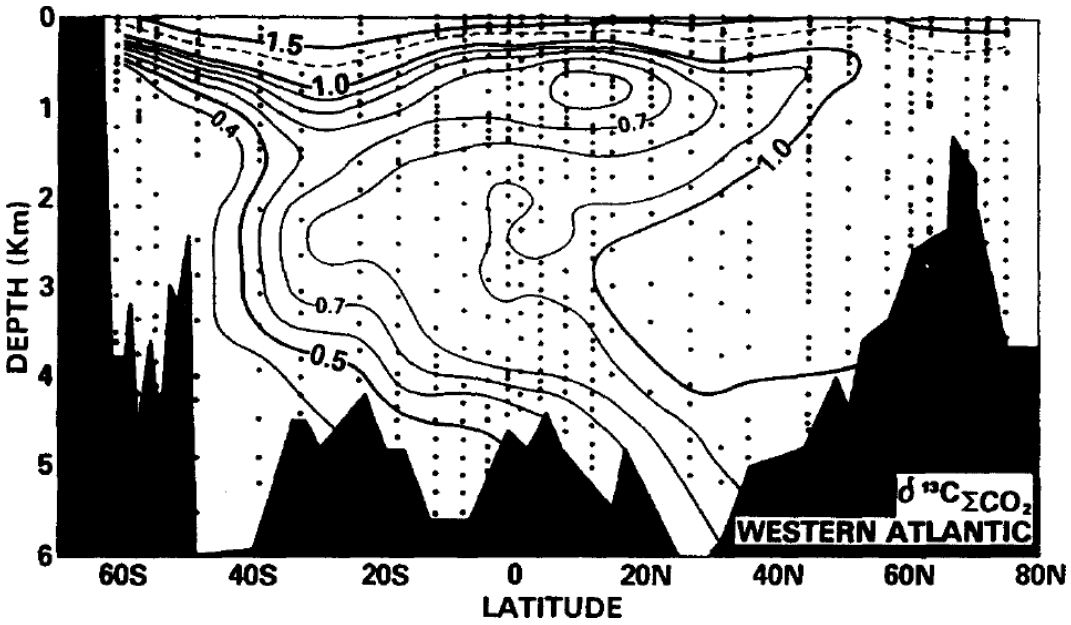

Figure 1.4: Distribution of δ^{13}C of dissolved inorganic carbon in the Western Atlantic Ocean. The relatively high δ^{13}C values at the surface are transported into the deep ocean following the NADW flowpath where they gradually become more depleted. Also visible are low-δ^{13}C Antarctic Intermediate Water (AAIW) and low-δ^{13}C Antarctic Bottom Water (AABW). After Kroopnick [1985].

Thesis motivation and outline

The aim of this thesis is (1) to come closer to a mechanistic description of the palaeoceanographic proxy δ^{13}C, and (2) to use this description to better assess the state of the glacial Atlantic Ocean. In other words the following questions will be investigated: how do foraminifera incorporate carbon isotopes into their shells, and what are the relevant processes? And: can we constrain the glacial Atlantic meridional overturning circulation (AMOC) from δ^{13}C reconstructions? If yes,

what are the most plausible AMOC scenarios? Finding the answers to these questions requires interdisciplinary thinking as well as an understanding and appreciation of the various processes and methods used in the different disciplines. I am using and combining knowledge from climate modellers, marine geologists, experimental biogeoscientists and chemical oceanographers. It is only within this framework that we can understand biological proxy signal formation in the oceans, interpret the signal sensibly, and draw meaningful conclusions. Each discipline on its own would struggle to achieve that goal.

The broad structure of the thesis is as follows. Chapters 2 to 6 provide the necessary background and preliminaries for the three main studies that are presented in Chapters 7 to 9. Chapter 10 summarises the main findings of the thesis and gives an outlook for possible future research.

In more detail: Chapter 2 is an introduction to carbonate chemistry in seawater as well as to carbon isotopes - prerequisites for understanding the δ^{13}C proxy basics. Chapter 3 gives an introduction into benthic foraminifera, which are the organisms recording the δ^{13}C proxy signal on the ocean floor. Chapter 4 moves on to describe what we know about the Last Glacial Maximum (LGM) and outlines the difficulties in assessing and understanding the glacial ocean. In Chapter 5 the different models used in this thesis are described. These include an ocean general circulation model (OGCM), an oceanic carbon cycle model, and a reaction-diffusion foraminifera calcification model (FCM). Chapter 6 then describes the δ^{13}C sediment data which are used for the model-data comparisons. Chapter 7 is the first of the three major studies: a model-data comparison of δ^{13}C in the glacial Atlantic Ocean.[1] Here three different glacial ocean scenarios are compared to reconstructions of δ^{13}C in order test which scenario is the most plausible. This is followed by Chapter 8: model sensitivity experiments with the FCM.[2] The chapter provides an assessment of the impact of various physical, chemical and biological processes on the signal formation of δ^{13}C in benthic foraminifera. Chapter 9 combines the approaches of the previous

[1] This chapter is based on Hesse et al. [2011], which has been published in *Paleoceanography*.

[2] This chapter is based on [Hesse et al., in review], which is currently in review at *Marine Micropaleontology*.

two chapters: the glacial ocean scenarios are combined with the FCM, and another model-data comparison is performed.[3] This is the first combination of such models and presents an important advance towards a fully mechanistic description of δ^{13}C signal formation. Finally, Chapter 10 concludes the thesis.

[3]This chapter forms the basis for a manuscript that is going to be submitted to *Climate of the Past* [Hesse et al., in preparation].

Chapter 2

Understanding δ^{13}C

2.1 Carbonate chemistry in seawater

Equilibrium

In order to understand δ^{13}C as a proxy it is essential to have an understanding of carbonate chemistry in seawater, where dissolved inorganic carbon (DIC) is typically present in three forms: as carbon dioxide (CO_2), bicarbonate ion (HCO_3^-), and carbonate ion (CO_3^{2-}). The total amount of DIC (often denoted as ΣCO_2) in the ocean is given by

$$[\Sigma CO_2] = [CO_2] + [HCO_3^-] + [CO_3^{2-}].^1 \tag{2.1}$$

In equilibrium the individual carbonate species are related by:

$$CO_2 + H_2O \overset{K_1}{\rightleftharpoons} HCO_3^- + H^+ \overset{K_2}{\rightleftharpoons} CO_3^{2-} + 2H^+, \tag{2.2}$$

[1] Square brackets refer to the concentration of a chemical species.

where K_1 and K_2 are the equilibrium or dissociation constants. They are given by

$$K_1 = \frac{[\mathrm{HCO_3^-}][\mathrm{H^+}]}{[\mathrm{CO_2}]} \tag{2.3}$$

and

$$K_2 = \frac{[\mathrm{CO_3^{2-}}][\mathrm{H^+}]}{[\mathrm{HCO_3^-}]}, \tag{2.4}$$

and depend on temperature, pressure and salinity. Figure 2.1 shows the distribution for the three carbonate species in seawater, and their dependence on temperature, pressure and salinity: at low pH almost all carbonate is in the form of CO_2, at intermediate pH HCO_3^- dominates, and at high pH levels CO_3^{2-} is the main carbonate species. The figure further shows that lowering temperature, lowering salinity, or decreasing pressure shifts the relative distribution of carbonate species to higher pH values. In other words, for a given pH more CO_2 is present under these circumstances (see Figure 2.1 for details).

Exchange with the atmosphere only occurs between dissolved $CO_{2(aq)}$ and atmospheric $CO_{2(g)}$. Therefore, bicarbonate and carbonate ions have to be exchanged via $CO_{2(aq)}$, effectively presenting a bottleneck for the air-sea gas exchange. This is the reason for the relatively long equilibration time of surface waters with the atmosphere, which takes about 240 days for a typical oceanic setting [Zeebe and Wolf-Gladrow, 2001]. The equilibration time is a measure of how long it takes to reduce the disequilibrium between atmospheric CO_2 partial pressure and ocean surface equilibrium CO_2 partial pressure to a fraction of $1/e$ of the initial difference. Looking into the details, the equilibration time depends on such things as the pH, the surface ocean mixed layer depth and the Revelle factor (see Zeebe and Wolf-Gladrow [2001]).

Kinetics

The chemical reactions for the carbonate system are:

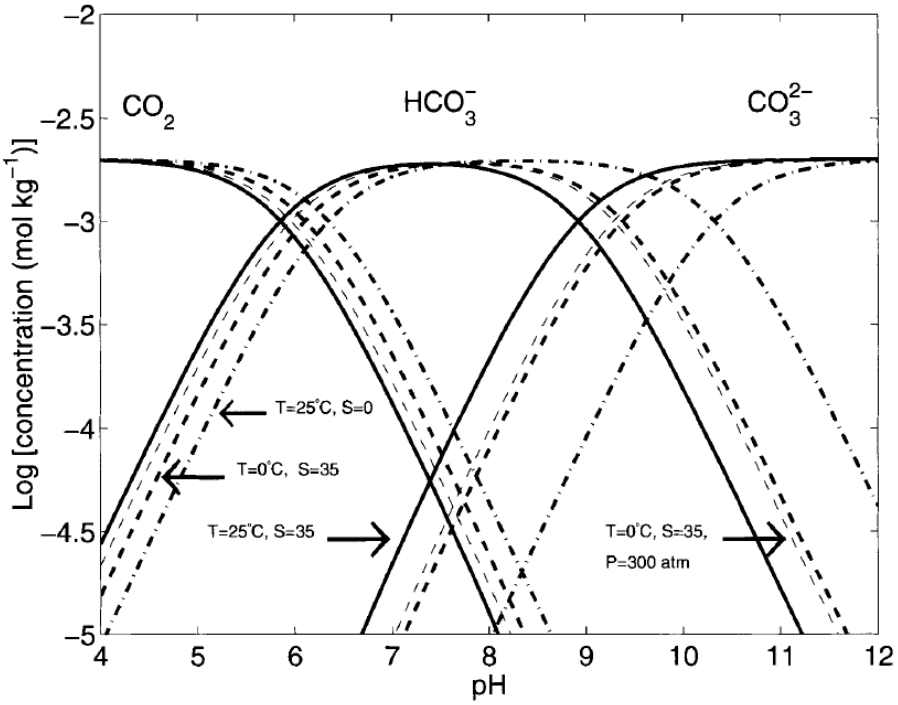

Figure 2.1: Bjerrum plot of the carbonate system in seawater. The solid line represents the reference case where temperature (T) is 25°C, salinity (S) is 35 and pressure (P) is 1 atm. Adapted from Zeebe and Wolf-Gladrow [2001].

$$\mathrm{CO_2 + H_2O} \underset{k_{-1}}{\overset{k_{+1}}{\rightleftharpoons}} \mathrm{H^+ + HCO_3^-} \tag{2.5}$$

$$\mathrm{CO_2 + OH^-} \underset{k_{-4}}{\overset{k_{+4}}{\rightleftharpoons}} \mathrm{HCO_3^-} \tag{2.6}$$

$$\mathrm{CO_3^{2-} + H^+} \underset{k_{-5}}{\overset{k_{+5}}{\rightleftharpoons}} \mathrm{HCO_3^-} \tag{2.7}$$

$$\mathrm{H_2O} \underset{k_{-6}}{\overset{k_{+6}}{\rightleftharpoons}} \mathrm{H^+ + OH^-} \tag{2.8}$$

$$\mathrm{B(OH)_3 + H_2O} \underset{k_{-7}}{\overset{k_{+7}}{\rightleftharpoons}} \mathrm{B(OH)_4^- + H^+}, \tag{2.9}$$

where k_+ and k_- are the reaction rate constants for the forward and backward reaction, respectively.[2] The hydration of CO_2 is achieved via the two reactions in Equations 2.5 and 2.6. Depending on pH, one or the other is more important: at low pH hydration via the reaction in Equation 2.5 is faster, at high pH the hydroxylation via Equation 2.6 dominates [Zeebe and Wolf-Gladrow, 2001]. The equilibrium constant K_1 is related to various kinetic constants by

$$K_1 = \frac{[\mathrm{H^+}][\mathrm{HCO_3^-}]}{[\mathrm{CO_2}]} = \frac{k_{+1}}{k_{-1}} = \frac{k_{+4}}{k_{-4}} K_W, \tag{2.10}$$

where K_W is the ion product of water, or $[H^+][OH^-]$ [Zeebe and Wolf-Gladrow, 2001].

2.2 Carbon isotopes

Carbon has three naturally occuring isotopes: ^{12}C, ^{13}C and ^{14}C. Their relative abundances on Earth are: 98.8922%, 1.1078%, and trace amounts, respectively. The stable isotopes are ^{12}C and ^{13}C, whereas ^{14}C is radioactive and decays with a half-life of 5,730 years.[3] The amount of ^{14}C is very small as it decays very fast with respect to the age of the Earth.[4] Because of their different atomic mass, isotopes have slightly different thermodynamic properties. For example, $^{13}CO_2$ has a higher mass and is therefore in a lower zero energy state than $^{12}CO_2$. This leads to isotopic equilibrium fractionation: it means that one isotope is preferentially found in one phase state, whereas the other isotope prefers another phase state. So when we are considering atmospheric CO_2 and dissolved CO_2 in the surface ocean in thermodynamical equilibrium, more $^{13}CO_2$ is found in the ocean, and conversely more $^{12}CO_2$ is in the atmosphere.

There are a number of non-equilibrium isotopic fractionation effects. These include incomplete or uni-directional processes (example: evaporation), kinetic effects in chemical reactions,

[2] Note: reaction rate constants (also calles kinetic constants) are typically written in lower case letters, whereas equilibrium (dissociation) constants are in upper case letters.

[3] This makes it a useful age determinator for the past 30,000 to 40,000 years.

[4] Radiocarbon is produced in the atmosphere by the collision of nitrogen with cosmic rays.

diffusion, and also metabolic effects [Zeebe and Wolf-Gladrow, 2001]. A metabolic effect is found during photosynthesis, for instance, where the lighter carbon isotope ^{12}C is preferentially taken up to form biomass.[5]

At this point it is useful to define the carbon isotopic ratio $\boldsymbol{\delta^{13}C}$: it is defined as the ratio of ^{13}C to ^{12}C of a sample, divided by the ratio of ^{13}C to ^{12}C of a standard, all minus 1. Since there is a lot more ^{12}C than ^{13}C, δ^{13}C is expressed in permil (‰):

$$\delta^{13}\mathrm{C} = \left[\frac{(^{13}\mathrm{C}/^{12}\mathrm{C})_{\text{sample}}}{(^{13}\mathrm{C}/^{12}\mathrm{C})_{\text{standard}}} - 1\right] \times 1000‰ \tag{2.11}$$

Measurements of δ^{13}C on calcitic shells are typically calibrated to the VPDB (Vienna Pee Dee Belemnite) scale [Mackensen, 2008].

Coming back to the equilibrium isotope fractionation in the carbonate system, it is important to remember that the distribution of δ^{13}C values of the different carbonate species depends on temperature and pH. The δ^{13}C distribution with changing pH can be seen in Figure 2.2. The heaviest chemical species (HCO_3^-) is the species most enriched in δ^{13}C, and the lightest species (CO_2) is the most depleted. The inter-species offset in δ^{13}C is constant across the pH range (there is no thermodynamic change as the pH is altered). The changes in δ^{13}C of the individual species is only related to the differing abundances at a given pH (cf. the Bjerrum plot in Figure 2.1).

Temperature-dependent carbon isotope fractionation in seawater is based on the following equilibrium fractionation coefficients (taken from Mook [1986], see Zeebe et al. [1999] for details):

[5] This is probably mediated by the enzyme Rubisco (Ribulose-1,5-bisphosphate carboxylase oxygenase) that oversees the first steps in carbon fixation during the photosynthesising process.

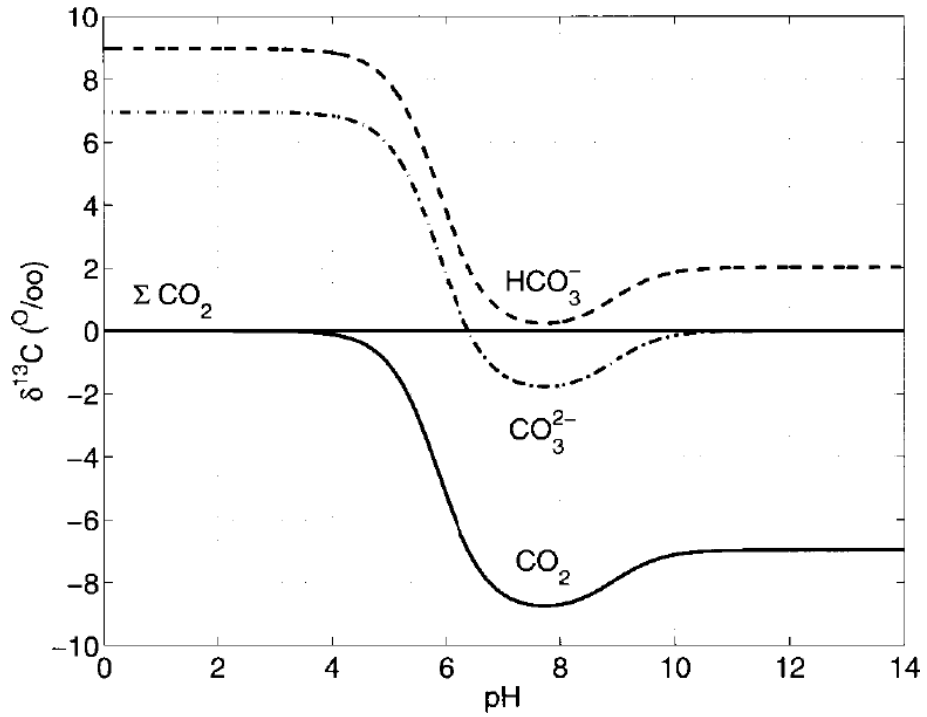

Figure 2.2: Distribution of the δ^{13}C values of the different carbon species as a function of pH at a temperature of 25°C. $\delta^{13}C_{\Sigma CO_2}$ is 0‰. At low pH all carbon is present in the form of CO_2, consequently $\delta^{13}C_{CO_2}$ is 0‰. Equally, for very high pH values, all carbon is converted to CO_3^{2-} and therefore $\delta^{13}C_{CO_3^{2-}}$ is at 0‰. At intermediate pH values HCO_3^- is the dominant species, which is the reason for $\delta^{13}C_{HCO_3^-}$ to approach 0‰. For different temperatures the differences in δ^{13}C between the carbon species may shift. Adapted from Zeebe and Wolf-Gladrow [2001].

$$\varepsilon_1 = \varepsilon_{(CO_{2(g)}-HCO_3^-)} = -9483/T + 23.89 \tag{2.12}$$

$$\varepsilon_2 = \varepsilon_{(CO_{2(aq)}-CO_{2(g)})} = -373/T + 0.19 \tag{2.13}$$

$$\varepsilon_3 = \varepsilon_{(CO_{2(aq)}-HCO_3^-)} = -9866/T + 24.12 \tag{2.14}$$

$$\varepsilon_4 = \varepsilon_{(CO_3^{2-}-HCO_3^-)} = -867/T + 2.52 \tag{2.15}$$

$$\varepsilon_5 = \varepsilon_{(CaCO_{3(calc)}-HCO_3^-)} = -4232/T + 15.10 \tag{2.16}$$

$$\varepsilon_6 = \varepsilon_{(CaCO_{3(calc)}-CO_3^{2-})} = -3341/T + 12.54 \tag{2.17}$$

where T is absolute temperature in Kelvin. Figure 2.3 is a graphical representation of the temperature-dependent fractionation between the carbonate system species. Isotopic equilibrium fractionation will be important in interpreting the results of the foraminifera calcification model sensitivity experiments in Chapter 8.

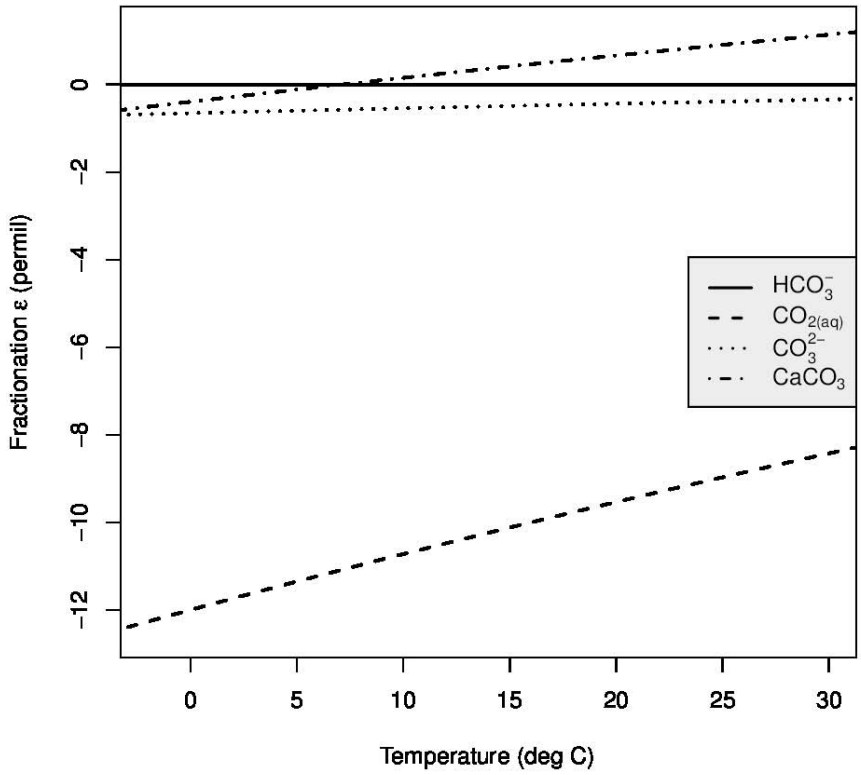

Figure 2.3: Fractionation between the different carbonate system species relative to HCO_3^- as a function of temperature. Replotted after Mook [1986].

2.3 Distribution of δ^{13}C in the oceans

In the surface ocean, the δ^{13}C value of dissolved inorganic carbon ($\delta^{13}C_{DIC}$) is controlled by the rate of air-sea exchange of CO_2, the time a particular water parcel is in contact with the

atmosphere, and biological activity by algae. Air-sea exchange is a function of temperature and wind speed [Wanninkhof and McGillis, 1999]. Higher wind speeds increase the roughness of the sea and therefore the surface area across which CO_2 molecules can be exchanged between ocean and atmosphere. At high wind speeds bubble formation and breaking waves complicate the picture further (see review by Wanninkhof et al. [2009] for details). As described above, a typical time to reach full carbon isotopic equilibrium between surface ocean and atmosphere is about 240 days [Zeebe and Wolf-Gladrow, 2001]. Therefore, depending on the initial δ^{13}C value of a water parcel that comes to the surface, by the time it leaves the surface ocean, it may or may not be in isotopic equilibrium. Broecker and Peng [1982] and Broecker and Maier-Reimer [1992] point out that there is no region in the world oceans where isotopic equilibrium is actually reached. The reason for this is that surface waters are replaced on faster timescales than the timescales needed for complete isotopic equilibrium. Algae prefer ^{12}C over ^{13}C. Typically, their biomass is therefore depleted in δ^{13}C and has a value range between -18 to $-23‰$ VPDB. Conversely, the $\delta^{13}C_{DIC}$ of the surrounding surface waters is enriched.

As mentioned above, equilibrium isotope fractionation between the atmosphere and the ocean causes the $\delta^{13}C_{DIC}$ to be heavier than atmospheric $\delta^{13}C_{CO_2}$, as ^{13}C with its lower zero energy is more likely to remain in the liquid phase. The surface ocean's $\delta^{13}C_{DIC}$ is about 8‰ heavier than atmospheric $\delta^{13}C_{CO_2}$ at 20°C. Additionally, because of an increased solubility of CO_2 with decreasing temperatures, $\delta^{13}C_{DIC}$ increases by 1‰ for a decrease in temperature by 10°C [Mackensen, 2008]. Given the atmospheric $\delta^{13}C_{CO_2}$ value has decreased from $-6.5‰$ VPDB in pre-industrial times to $\sim -8‰$ VPDB today due to the burning and release of fossil organic carbon, the range of surface ocean $\delta^{13}C_{DIC}$ today from equilibrium fractionation alone would be between -1 and $+2‰$ [Mackensen, 2008].

As water from the surface enters the deep ocean (see also Chapter 1 on ocean circulation), there is no exchange with the atmosphere anymore. Now $\delta^{13}C_{DIC}$ is affected by the remineralisation of organic matter sinking through the water column, and the amount of time the water

parcel stays out of contact with the atmosphere. Dead organic matter from the surface sinks into the ocean and is oxidised and remineralised along its trajectory.[6] This process releases the low δ^{13}C of the organic matter and thereby lowers $\delta^{13}C_{DIC}$. The longer a water parcel stays out of touch with the atmosphere, the lower its $\delta^{13}C_{DIC}$ value becomes, which explains the low $\delta^{13}C_{DIC}$ values found in the North Pacific, where waters come back to the surface (Figure 2.4).

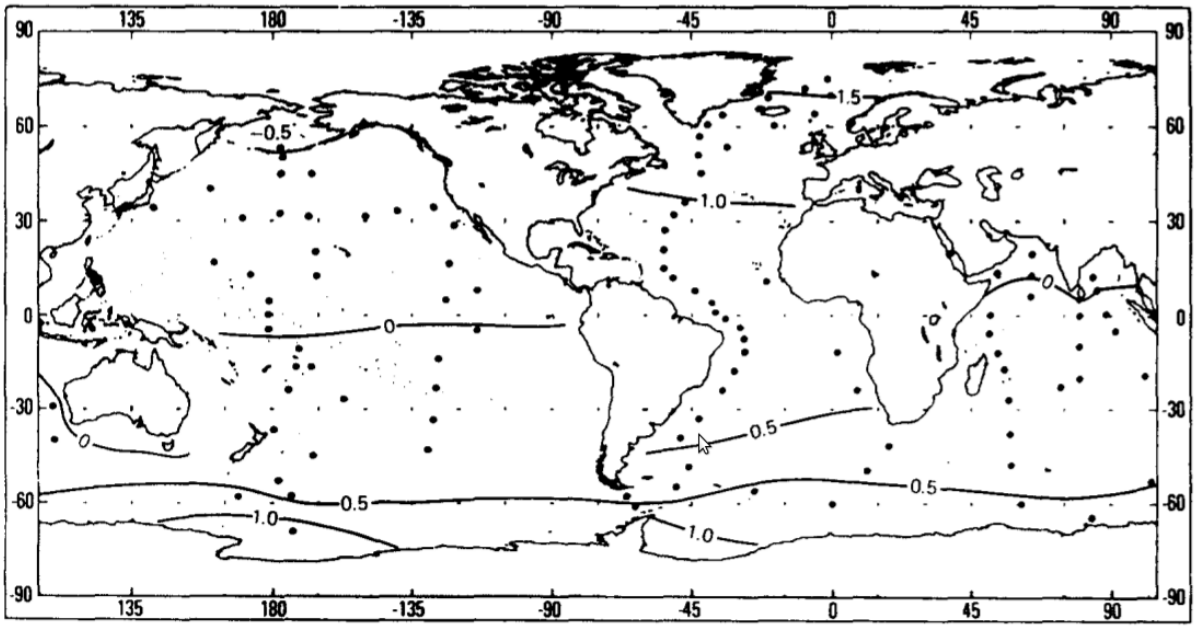

Figure 2.4: Horizontal projection of the δ^{13}C distribution at a depth of between 2000 and 2500 meters. The δ^{13}C values are highest in the North Atlantic and lowest in the North Pacific. After Kroopnick [1985].

With these basics in mind, we can now explain the distribution of $\delta^{13}C_{DIC}$ in the Atlantic Ocean that Kroopnick captured in Figure 1.4 [Kroopnick, 1985]. High δ^{13}C waters from the surface enter the deep North Atlantic and are transported as NADW southward at depth, gradually lowering $\delta^{13}C_{DIC}$ over time. Upon reaching the Southern Ocean NADW is mixed into relatively low δ^{13}C circumpolar waters, some of which make it back to the surface before being subducted again flowing northward as Antarctic Intermediate Water (AAIW). Since exchange of these wa-

[6]Typically only 1% of organic matter sinking from the surface ocean reaches the seafloor. The remaining 99% are remineralised and recycled in the ocean.

ters with the atmosphere is short, the subducted waters are far from being in isotopic equilibrium with the atmosphere (see also the discussion part of Chapter 7). Therefore their $\delta^{13}C_{DIC}$ value is substantially lower than the NADW's $\delta^{13}C_{DIC}$ value. Antarctic Bottom Water (AABW) has a similarly low δ^{13}C signature as surface waters in its formation region are not in atmospheric contact for long due to the sea-ice cover which prevents air-sea exchange, and their original δ^{13}C signature is low to begin with.

Chapter 3

Benthic foraminifera

Benthic foraminifera are one of the most abundant organisms living on the seafloor. Biologically they are single-celled, pre-dominantly marine organisms belonging to the phylum protista and forming the order foraminiferida [Murray, 2006]. They are taxonomically further subdivided based on their shell shape, structure, and composition [Murray, 2006]. Benthic foraminifera are typically split into those living above the water-sediment interface (epifaunal), and those living within the sediment (infaunal). They are typically symbiont-barren, in contrast to many of their planktonic relatives, which often host photosynthesising symbionts. Comparatively little is known about deep-sea benthic foraminifera due to their difficult-to-reach habitats.

The reason why palaeoceanographers are interested in benthic foraminifera is that the δ^{13}C value of their shells ($\delta^{13}C_{foram}$) can be used as a proxy for the distribution of water masses. Additionally, the difference in δ^{13}C between planktonic and benthic foraminifera at any given location serves as a proxy for the efficiency of the biological pump, i.e. the amount of organic carbon that is falling through the water column. A further advantage of benthic foraminifera is that they are found almost everywhere on the ocean floor, and that they are abundant. Furthermore, they have been on Earth for hundreds of millions of years [Culver, 1991], which makes them well placed

for studies both in the more recent geological past of the Pleistocene, as well as in the entire Cenozoic era.

Benthic $\delta^{13}C_{foram}$ values have been widely used as a proxy for reconstructing the distributions of past water masses in the world oceans, particularly in the Atlantic Ocean [Curry et al., 1988; Duplessy et al., 1988; Sarnthein et al., 1994; Mackensen et al., 2001; Bickert and Mackensen, 2004; Curry and Oppo, 2005; Hesse et al., 2011]. Implicit in these studies is the assumption that the $\delta^{13}C_{foram}$ value records the $\delta^{13}C_{DIC}$ of the water mass in which the foraminifera grow. Over the years there has been increasing evidence that different foraminiferal species record offsets of $\delta^{13}C_{foram}$ with respect to $\delta^{13}C_{DIC}$ depending on their habitat [Zahn et al., 1986; Mackensen et al., 1993]. Infaunal species tend to record lower $\delta^{13}C_{foram}$ values than epifaunal ones. Therefore, many authors of palaeoceanographic studies have focused on epifaunal species such as *Cibicidoides wuellerstorfi* (Schwager 1866) (see Figure 3.1), that record $\delta^{13}C_{DIC}$ more faithfully, if perhaps accidently, in a 1:1 relationship [Woodruff et al., 1980; Zahn et al., 1986; Duplessy et al., 1988; Hodell et al., 2001]. Another complication, however, is the fact that even these species record an offset in their $\delta^{13}C_{foram}$ signal with respect to $\delta^{13}C_{DIC}$ when they are exposed to certain environmental conditions, such as algal bloom-derived phytodetritus layers [Mackensen et al., 1993; Zarriess and Mackensen, 2011].

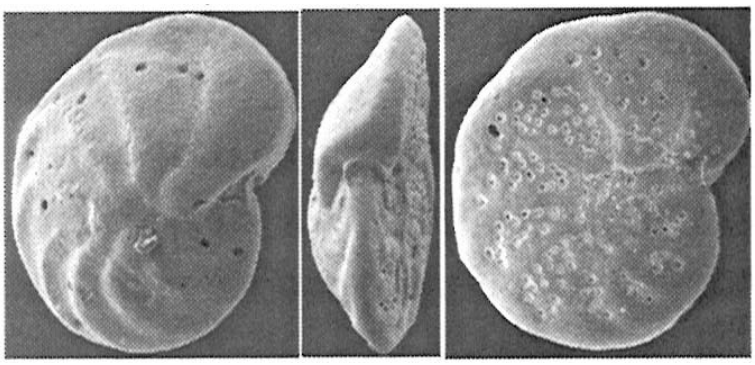

Figure 3.1: Images from scanning electron micrographs for *Cibicidoides wuellerstorfi*. The longest dimension (in μm) in each image is (from left to right) 360, 560, and 450. Adapted from Murray [2006].

In order to extract the δ^{13}C signal from foraminiferal shells, one is typically using specimen that build calcareous shells. Specimen are picked from sediment cores, the shells then sorted into certain size fractions, cleaned, crushed, and finally sent into a mass spectrometer where their isotopic composition is measured.

As mentioned above, not much is known about the biological life cycles and behaviour of deep-sea benthic foraminifera. In-situ measurements of respiration and calcification rates on deep-sea benthic foraminiferal species hardly exist. Some authors have measured these rates under laboratory conditions (e.g. Hannah et al. [1994]; Nomaki et al. [2007]; Geslin et al. [2011]; Glas et al. [2012]). Since it is notoriously difficult to culture deep-sea benthic foraminifera in the laboratory under in-situ conditions, culture experiments have often been limited to shallow-water species [Chandler et al., 1996], or specimen taken from water depths shallower than 250 m [Wilson-Finelli et al., 1998; Havach et al., 2001]. Culturing systems like those developed by Hintz et al. [2004] should allow for the much desired more systematic experiments on deep-sea benthic foraminifera. From a theoretical point of view, progress has mostly been made on planktonic foraminifera [Wolf-Gladrow et al., 1999; Zeebe et al., 1999]. In the benthic realm Zeebe [2007] pointed out in a modelling study that the impact of porewater on bottom water may need to be considered when interpreting $\delta^{13}C_{foram}$.

Ultimately, understanding the processes for δ^{13}C signal formation inside the foraminiferal cell is essential for the interpretation of the proxy signal. Our understanding of benthic foraminifera is still very limited, especially when it comes to the calcification process. The traditional view on the calcification process as summarised by Erez [2003] is that the calcium and DIC building blocks are taken up in seawater vacuoles via endocytosis. They are then kept in so-called pools where they become highly concentrated before being transfered to the site of calcification to form the calcium carbonate shell. More and more studies now try to assess the physiological processes in foraminifera, but a sound mechanistic description that satisfies all observations has not emerged yet. In laboratory experiments de Nooijer et al. [2009] studied changes in the pH

distribution inside a foraminiferal cell as it was calcifying a new chamber. They found that the pH increases dramatically towards the calcification site. Glas et al. [2012] looked at changes in pH outside the shell and found that pH levels drop substantially for the duration of chamber formation. How these observations combine in order to describe the calcification process fully has not been established yet.

Chapter 4

The Last Glacial Maximum

The Last Glacial Maximum (LGM) is the time period from 19,000 to 23,000 years ago, as defined by the EPILOG project [Mix et al., 2001]. It is characterised by the existence of huge ice sheets in the Northern Hemisphere, namely the Finno-Scandinavian ice sheet stretching across most of Northern Europe, the Laurentide ice sheet covering vast areas of North America, and possibly an ice sheet along parts of the Arctic rim of Asia [Clark et al., 2009]. Consequently, less water was available in the oceans causing sea-level to be lower by about 120 meters when compared to today [Fairbanks, 1989]. Temperatures were generally lower, though reconstructions and models partly disagree about the extent. In a recent study Clark et al. [2009] found that average deep ocean temperatures where lowered by 3.25 ± 0.55°C.

For the sea surface temperature reconstructions there have been various efforts in the past in order to assemble an ocean wide dataset. The major projects are the Climate Long Range Investigation, Mapping, and Prediction (CLIMAP) project of the 1970s and 1980s [CLIMAP Project Members, 1976, 1981], the Glacial Atlantic Ocean Mapping (GLAMAP) project (see Sarnthein et al. [2003] and references therein), and the Multiproxy Approach for the Reconstruction of the Glacial Ocean Surface (MARGO) project [Kucera et al., 2005; Waelbroeck et al., 2009]. Using

transfer functions for temperature based on microfossil assemblages, CLIMAP found a lowering of SSTs in the tropics of approximately 2°C, which was subsequently found to be too small a change (e.g. Anderson and Webb [1994]; Guilderson et al. [1994]; Mix et al. [1999]). CLIMAP further suggested perennial sea ice in the Nordic Seas [CLIMAP Project Members, 1981]. Compared to CLIMAP, GLAMAP SSTs are higher in the North Atlantic but lower in the tropical and South Atlantic. Correspondingly, GLAMAP suggests ice-free Nordic Seas in the summer and a winter sea ice margin similar to the CLIMAP sea ice boundary for summer. In the Southern Ocean, GLAMAP proposes more winter sea ice in Drake Passage, but less sea ice at the northern boundary of the Weddell Sea compared to CLIMAP. The MARGO project is the latest attempt at reconstructing glacial SSTs following a multiproxy approach that has more data points and a denser spatial coverage. MARGO annual mean cooling in the tropics confirms GLAMAP's findings [Waelbroeck et al., 2009]. Figure 4.1 shows the annual mean air temperature anomalies with respect to the present day from a coupled ocean-atmosphere model forced by CLIMAP and GLAMAP SSTs [Romanova et al., 2004]. The model runs were forced by SSTs from CLIMAP (with an extra 3°C cooling in the tropics, Figure 4.1, left hand side) and from GLAMAP (Figure 4.1, right hand side). The model simulations in Chapters 7 and 9 will further build on the different SST reconstructions described here.

The LGM is an ideal candidate for testing various climate hypotheses with the help of models. First, it is a distinct climate state in the not too distant past, where we have a lot of information from various proxy records. This is very useful for setting boundary conditions in climate models. Second, it is a very different climate state compared to today and the Holocene epoch. Climate models that capture both today's climate state and the LGM's climate state can be considered better at representing the climate system as a whole compared to those that can only represent one state or the other. Third, the LGM is considered to be a climate state close to equilibrium, which makes modelling easier, as models can be run until they reach equilibrium, too. Fourth, CO_2 levels, continental geography and orbital parameters, all of which are important

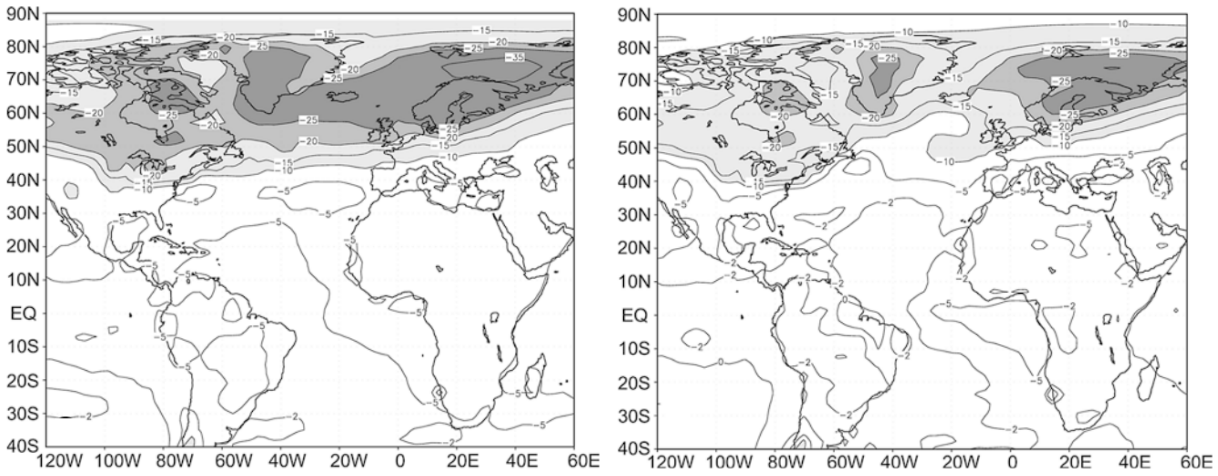

Figure 4.1: Glacial annual mean air temperature anomalies with respect to the present day, based on (left) the CLIMAP SST reconstruction [CLIMAP Project Members, 1981] with an additional 3°C cooling in the tropics [Lohmann and Lorenz, 2000], and (right) the GLAMAP SST reconstruction [Paul and Schäfer-Neth, 2003]. Adapted from Romanova et al. [2004].

basic boundary conditions for climate models, are well known [Mix et al., 2001].

Glacial ocean circulation

Since we know that (a) the glacial climate was distinctly different to today's climate, and (b) the oceans are one of the major reservoirs for both heat and carbon, reconstructing the glacial ocean and its circulation is an important step towards a full understanding of the LGM climate system. Traditionally, research has been focussed on the Atlantic Ocean. The North Atlantic today is one of the areas of deep water formation, where relatively salty and warm waters from the Gulf of Mexico arrive, cool down, and sink due to a density gradient with the surrounding less salty waters. More recently, the Southern Ocean's role has also received more attention (see below).

The state of deep water formation during the LGM has been debated by many and was reviewed recently [Lynch-Stieglitz et al., 2007]. Based on proxy data many authors have suggested that the formation rate of NADW was reduced during the LGM. This resulted in a shallower flow path of what is called Glacial North Atlantic Intermediate Water (GNAIW) [Duplessy et al., 1988; Curry and Oppo, 2005; Lynch-Stieglitz et al., 2007]. Figure 4.2 shows the distribution

of δ^{13}C as derived from benthic foraminiferal shells in the western Atlantic Ocean [Curry and Oppo, 2005]. The shoaled GNAIW flowpath is clearly visible. At the same time export of AABW from the Southern Ocean intensified, which has been inferred from grain size, radiocarbon, and ^{231}Pa/^{230}Th studies (e.g. Ledbetter and Johnson [1976]; Robinson et al. [2005]; Negre et al. [2010]).

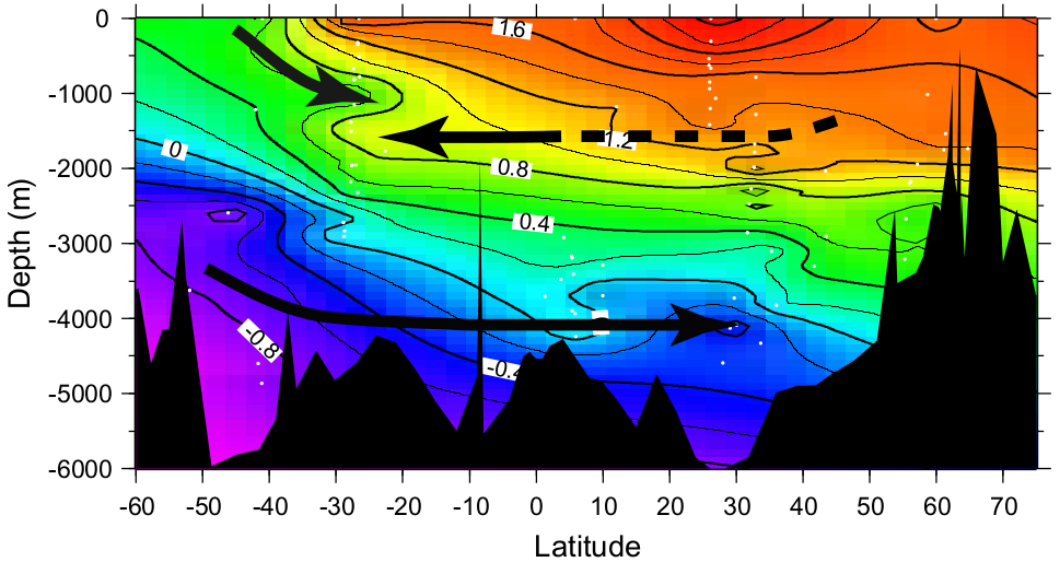

Figure 4.2: Distribution of δ^{13}C from benthic foraminifera in the glacial Western Atlantic Ocean. Data points are indicated by white dots. Present-day North Atlantic Deep Water is shoaled and now termed Glacial North Atlantic Intermediate Water. After Curry and Oppo [2005].

Coupled ocean-atmosphere model simulations of the LGM climate show a large spread. Otto-Bliesner et al. [2007] found large variations in the glacial circulation produced by four different coupled models, while the same models produced similar circulations for the present-day. Weber et al. [2007] compared the response of the Atlantic Meridional Overturning Circulation (AMOC) to LGM forcing in nine coupled models and found that model results differ widely. Coupled models even disagree as to whether the AMOC should have decreased or increased relative to the present-day [Hewitt et al., 2003; Meissner et al., 2003; Shin et al., 2003a; Roche et al., 2007].

Model-data comparisons

Model-data comparisons are ultimately the best tool for testing competing forward modelling scenarios. There are but a few attempts to directly model marine proxy data for the LGM deep ocean. Butzin et al. [2005] looked at radiocarbon in the glacial ocean simulated by different model scenarios. As radiocarbon measurements are relatively sparse, however, it is difficult to constrain simulations and the real LGM ocean. The more widely distributed palaeoproxy δ^{13}C is therefore more promising, even though it does not yield any kinematic information. This approach has been taken before to assess the glacial ocean (e.g. Winguth et al. [1999]; Matthies et al. [2004]; Tagliabue et al. [2009]). For the model-data comparisons in Chapters 7 and 9 a dataset of 220 δ^{13}C sediment cores in the entire Atlantic Ocean is used (see Chapter 6 for a description), which is unprecedented. Previous data compilations were restricted to particular Atlantic sub-areas (e.g. the western Atlantic [Curry and Oppo, 2005], the East Atlantic [Sarnthein et al., 1994], or the South Atlantic [Bickert and Mackensen, 2004]), or they were using a mixture of epifaunal and infaunal benthic foraminiferal species [Oliver et al., 2010].

Chapter 5

Description of models

This chapter provides an overview and a description of the models used in the thesis. The three models are the Hamburg Large Scale Geostrophic ocean general circulation model (LSG), the Hamburg Oceanic Carbon Cycle circulation model (HAMOCC), and the foraminifera calcification model (FCM). A description of the ocean model scenarios (based on Butzin et al. [2005]) that are used in Chapters 7 and 9 is also included. For this thesis, the FCM has been further developed from the original version by Wolf-Gladrow et al. [1999] and Zeebe et al. [1999] so that it can now be used for modelling calcification in benthic foraminifera (see also Chapter 8).

On a more general note, the LSG and HAMOCC versions used in this thesis have seen their heyday, and are not state-of-the-art models anymore. They do have some important advantages, though, which is why they were employed in this thesis. These include: (1) the possibility to integrate over long time scales of 10,000 - 100,000 years, and thereby (2) reaching an equilibrium state at relatively little computational cost. This is very useful for modelling the LGM, which is considered to be in a climatic equilibrium state (see Chapter 4), and for making many model simulations with competing scenarios.

To the best of my knowledge, the FCM is the only model of its kind. Since it includes vital

effects and considers the immediate microenvironment of the foraminifer, it is a crucial tool for palaeoceanographic studies, and is important for developing our theoretical understanding of proxy formation in foraminifera.

5.1 The Hamburg Large Scale Geostrophic (LSG) ocean general circulation model

In the thesis an updated version of the LSG ocean circulation model is used [Maier-Reimer et al., 1993]. This version includes a third-order advection scheme for tracers [Schäfer-Neth and Paul, 2001; Prange et al., 2003] as well as an overflow parametrisation for the bottom boundary layer [Lohmann, 1998; Lohmann and Schulz, 2000]. The set-up is described in further detail by Butzin et al. [2005]. Model resolution is 3.5° on an Arakawa-E grid in the horizontal and 22 levels in the vertical. The LSG model is calibrated in simulations of Δ^{14}C [Butzin et al., 2005]. The ocean is driven by ten-year averaged monthly fields of wind stress, surface air temperature, and freshwater flux which will be discussed below. A surface heat flux formulation based on an atmospheric energy balance model permits that SSTs can freely adjust to ocean circulation changes [Rahmstorf and Willebrand, 1995; Prange et al., 2003; Butzin et al., 2005]. The hydrological cycle is closed by a runoff scheme which allows that Sea Surface Salinities (SSSs) can freely evolve. The model uses an implicit method for the integration of the momentum equations with a time step of one month, and it is integrated over 20,000 years to quasi steady-state conditions.

The forcing fields for the LSG are derived in simulations using the atmospheric circulation model ECHAM3/T42 (carried out by Lohmann and Lorenz [2000] and Prange et al. [2004]), which by itself is forced with prescribed values of glacial insolation, CO_2, ice-sheet cover and SSTs. We employ two different reconstructed glacial SST fields (see Chapter 4) for which we make two experiments each. The first SST field is based on the CLIMAP reconstruction [CLIMAP Project Members, 1981] with an additional cooling of 3°C in the tropics between

30°N and 30°S [Lohmann and Lorenz, 2000], which is used for scenarios CB (**C**LIMAP **B**asic glacial) and CS (**C**LIMAP **S**outhern Ocean freshwater changes). The second SST field is taken from the Glacial Atlantic Ocean Mapping (GLAMAP) reconstruction (see Sarnthein et al. [2003] and references therein) in the globally extended version of Paul and Schäfer-Neth [2003], which is used for scenarios GB (**G**LAMAP **B**asic glacial) and GS (**G**LAMAP **S**outhern Ocean freshwater changes). In addition to the atmospheric forcing provided by ECHAM3, scenarios CS and GS feature a modified freshwater balance of the Southern Ocean which mimics additional brine release due to enhanced northward sea ice export, as suggested by recent LGM climate modeling studies [Shin et al., 2003b; Schmittner, 2003]. This results in a very cold and very saline abyssal Atlantic which is depleted in Δ^{14}C [Butzin et al., 2005], and improves the agreement with marine ^{14}C records and with other marine proxy data evidence for the LGM (Adkins et al. [2002]; see Lynch-Stieglitz et al. [2007] for a review). Experiment CB is not described further as temperature, salinity and radiocarbon distributions of this run are unrealistic [Butzin et al., 2005].

The study described in Chapter 7 is using glacial scenarios GB, GS and CS. In the study in Chapter 9 only GB and GS are considered.

5.2 The Hamburg Oceanic Carbon Cycle circulation model (HAMOCC), version HAMOCC2s

HAMOCC2s is used for simulating the distribution of $\delta^{13}C_{DIC}$ in the glacial ocean [Heinze and Maier-Reimer, 1999; Heinze et al., 1999]. The model considers the dissociation of carbonic acid and the borate buffer as well as particulate organic carbon, calcium carbonate, and opal. In addition, HAMOCC2s includes a 10-layer sediment module (following Archer et al. [1993]) which accounts for chemical reactions of biogenic particulate matter with pore waters, diffusive processes in pore and bottom waters, vertical sediment advection as well as sediment accumula-

tion, and bioturbation. Input of terrigenous matter is prescribed by present-day dust deposition [Andersen et al., 1998] and by global-mean, present-day weathering fluxes at the sea surface, which are asymptotically approached by the integrated sediment accumulation during the model run. There is no iron limitation in HAMOCC2s. The model is able to diagnose atmospheric CO_2 as affected by processes in the ocean and yields a preindustrial concentration of 283 ppmV for $^{12}CO_2$. We do not attempt to capture the carbon-isotopic response to glacial-interglacial carbon cycle changes (e.g. in the terrestrial carbon pool, ocean alkalinity or the biological pump) but seek to investigate the isolated effect of various glacial ocean overturning scenarios on marine $\delta^{13}C$. For this reason all glacial model runs employ biogeochemical parameter settings identical to pre-industrial time.

HAMOCC2s is driven by annual-mean thermohaline circulation fields provided by the LSG ocean circulation model, which are used 'off-line', i.e. the fields are used for tracer advection without further dynamic computations (see England and Maier-Reimer [2001] for a review of tracer modeling). HAMOCC2s adopts the spatial resolution of the LSG (see Figure 5.1 for a representation of the horizontal resolution), but uses a different time step of one year. A parametrisation for convective mixing retains seasonality effects which would get lost otherwise [Heinze and Maier-Reimer, 1999]. The total integration time for the experiments in HAMOCC2s is 70,000 - 100,000 years.

5.3 The foraminifera calcification model (FCM)

5.3.1 General model description

The FCM is a reaction-diffusion model of the carbonate system in seawater around an idealised foraminiferal shell in spherical geometry. Wolf-Gladrow et al. [1999] developed the original model version, which includes equations for total carbon (^{12}C and ^{13}C) only. It was intended

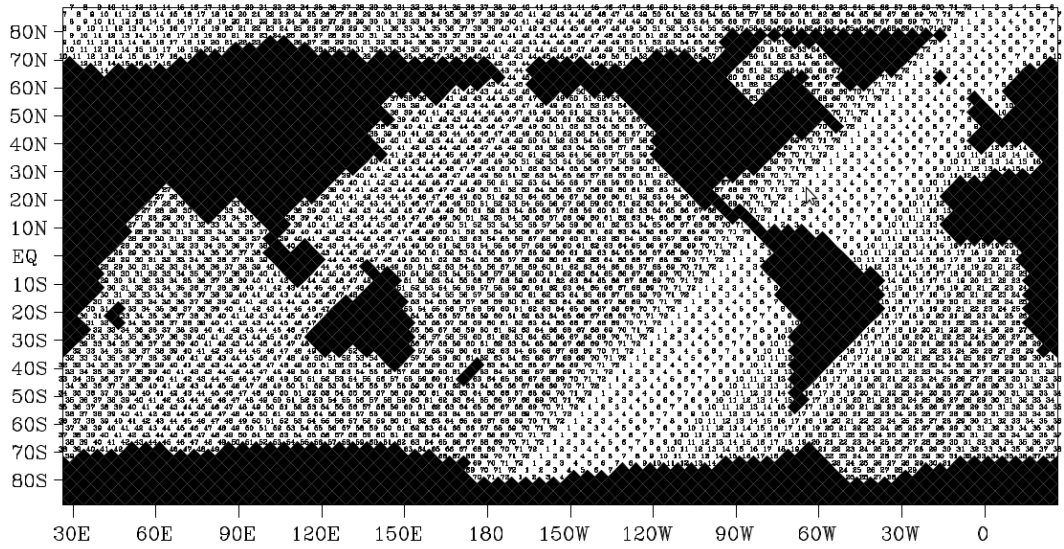

Figure 5.1: HAMOCC2s grid resolution for the present-day (adapted from Heinze and Maier-Reimer [1999]).

to simulate the distribution of carbonate species with distance from the shell of planktonic foraminifera, for symbiont-bearing and symbiont-barren species, in dark and light conditions. Carbon isotopes have been included in the model by Zeebe et al. [1999], which allows for the simulation of the shell's final $\delta^{13}C_{foram}$ value. Boundary conditions are, on the one hand, set by the bulk seawater conditions far away from the shell (outer boundary condition set at a distance of ten times the shell radius), and, on the other hand, by the rates of exchange across the simulated shell surface (inner boundary condition, see Figure 5.2 for a schematic drawing of the model geometry). Bulk seawater properties used as model input are temperature, salinity, pressure, pH, $\delta^{13}C_{DIC}$, $\delta^{13}C_{POC}$ (the $\delta^{13}C$ of particulate organic carbon, i.e. the foraminifer's food, which is important for respiration), and total alkalinity (TA). Foraminifer-specific model input are respiration rate and calcification rate. Given these inputs, the model iteratively calculates the concentrations of H^+, OH^-, CO_2, HCO_3^-, CO_3^{2-}, $B(OH)_3$ and $B(OH)_4^-$ as well as the $\delta^{13}C$ values of the carbonate system species (CO_2, HCO_3^-, CO_3^{2-}) with distance from the shell, and the final $\delta^{13}C_{foram}$. Concentration calculations are based on molecular diffusion, the reactions between

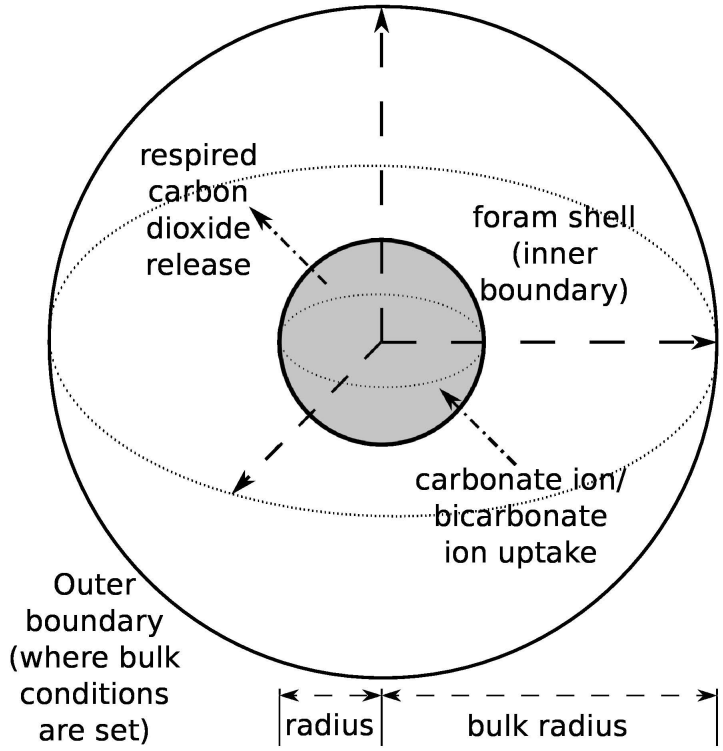

Figure 5.2: Schematic representation of the foraminifera calcification model.

the different carbonate system species, and sources or sinks for certain chemical species at the boundary of the modelled calcite shell (see Wolf-Gladrow et al. [1999] for details). The general form of the equations for the concentration $c(r,t)$ of a carbonate system species is:

$$0 = \frac{\partial c(r,t)}{\partial t} = \text{Diffusion} + \text{Reaction} + \text{Uptake},$$

where r is the distance from the centre of the shell and t is time. The full diffusion-reaction equations for total carbon (C = ^{13}C + ^{12}C) are [Wolf-Gladrow et al., 1999]:

For CO_2:

$$\begin{aligned} 0 =& \frac{D_{CO_2}}{r^2}\frac{\mathrm{d}}{\mathrm{d}r}\left(r^2\frac{\mathrm{d}[CO_2]}{\mathrm{d}r}\right) + (k_{-1}[H^+] + k_{-4})[HCO_3^-] \\ & - (k_{+1} + k_{+4}[OH^-])[CO_2] + f_{\text{res}}^{CO_2}, \end{aligned} \tag{5.1}$$

where D_{CO_2} is the diffusion coefficient of CO_2, r is the distance to the centre of the simulated foraminiferal shell, and the reaction rate constants are k_i.

Likewise for HCO_3^-:

$$\begin{aligned} 0 =& \frac{D_{HCO_3}}{r^2}\frac{\mathrm{d}}{\mathrm{d}r}\left(r^2\frac{\mathrm{d}[HCO_3^-]}{\mathrm{d}r}\right) + k_{+1}[CO_2] - k_{-1}[H^+][HCO_3^-] \\ &+ k_{+4}[CO_2][OH^-] - k_{-4}[HCO_3^-] + k_{+5}[H^+][CO_3^{2-}] - k_{-5}[HCO_3^-] \end{aligned} \tag{5.2}$$

For CO_3^{2-}:

$$0 = \frac{D_{CO_3}}{r^2}\frac{\mathrm{d}}{\mathrm{d}r}\left(r^2\frac{\mathrm{d}[CO_3^{2-}]}{\mathrm{d}r}\right) + k_{-5}[HCO_3^-] - k_{+5}[H^+][CO_3^{2-}] \tag{5.3}$$

For H^+:

$$\begin{aligned} 0 =& \frac{D_H}{r^2}\frac{\mathrm{d}}{\mathrm{d}r}\left(r^2\frac{\mathrm{d}[H^+]}{\mathrm{d}r}\right) + (k_{-5} - k_{-1}[H^+])[HCO_3^-] + k_{+1}[CO_2] - k_{+5}[H^+][CO_3^{2-}] \\ &+ k_{+6} - k_{-6}[H^+][OH^-] + k_{+7}[B(OH)_3] - k_{-7}[H^+][B(OH)_4^-] \end{aligned} \tag{5.4}$$

For OH^-:

$$0 = \frac{D_{OH}}{r^2}\frac{\mathrm{d}}{\mathrm{d}r}\left(r^2\frac{\mathrm{d}[OH^-]}{\mathrm{d}r}\right) + k_{-4}[HCO_3^-] - k_{+4}[CO_2][OH^-] + k_{+6} - k_{-6}[H^+][OH^-] \tag{5.5}$$

For $B(OH)_3$:

$$0 = \frac{D_{B(OH)_3}}{r^2}\frac{\mathrm{d}}{\mathrm{d}r}\left(r^2\frac{\mathrm{d}[B(OH)_3]}{\mathrm{d}r}\right) - k_{+7}[B(OH)_3] + k_{-7}[H^+][B(OH)_4^-] \tag{5.6}$$

For $B(OH)_4^-$:

$$0 = \frac{D_{B(OH)_4}}{r^2}\frac{\mathrm{d}}{\mathrm{d}r}\left(r^2\frac{\mathrm{d}[B(OH)_4^-]}{\mathrm{d}r}\right) + k_{+7}[B(OH)_3] - k_{-7}[H^+][B(OH)_4^-] \tag{5.7}$$

For the ^{13}C calculations, only the reactions for $^{13}CO_2$, $H^{13}CO_3^-$ and $^{13}CO_3^{2-}$ need to be considered [Zeebe et al., 1999]:

For $^{13}CO_2$:

$$\begin{aligned} 0 =& \frac{D_{^{13}CO_2}}{r^2}\frac{\mathrm{d}}{\mathrm{d}r}\left(r^2\frac{\mathrm{d}[^{13}CO_2]}{\mathrm{d}r}\right) + (k'_{-1}[H^+] + k'_{-4})[H^{13}CO_3^-] \\ & - (k'_{+1} + k'_{+4}[OH^-])[^{13}CO_2] + f_{\text{res}}^{^{13}CO_2} \end{aligned} \tag{5.8}$$

For $H^{13}CO_3^-$:

$$\begin{aligned} 0 =& \frac{D_{H^{13}CO_3}}{r^2}\frac{\mathrm{d}}{\mathrm{d}r}\left(r^2\frac{\mathrm{d}[H^{13}CO_3^-]}{\mathrm{d}r}\right) + k'_{+1}[^{13}CO_2] - k'_{-1}[H^+][H^{13}CO_3^-] \\ & + k'_{+4}[^{13}CO_2][OH^-] - k'_{-4}[H^{13}CO_3^-] + k'_{+5}[H^+][^{13}CO_3^{2-}] - k'_{-5}[H^{13}CO_3^-] \end{aligned} \tag{5.9}$$

For $^{13}CO_3^{2-}$:

$$0 = \frac{D_{^{13}CO_3}}{r^2}\frac{\mathrm{d}}{\mathrm{d}r}\left(r^2\frac{\mathrm{d}[^{13}CO_3^{2-}]}{\mathrm{d}r}\right) + k'_{-5}[H^{13}CO_3^-] - k'_{+5}[H^+][^{13}CO_3^{2-}] \tag{5.10}$$

The kinetic rate constants for ^{13}C (k'_i) are used to take into account kinetic fractionation effects (see Zeebe et al. [1999] for details). Temperature-dependent equilibrium fractionation between the carbonate system species in bulk seawater are treated like in Zeebe et al. [1999]. The model is capable of simulating both HCO_3^- and CO_3^{2-} uptake.

5.3.2 Pressure dependence of dissociation constants

We are using the model in order to make sensitivity simulations for deep-sea benthic foraminifera (see Chapter 8 and Hesse et al. [in review]). Since the model has so far only been used for planktonic foraminifera living close to the sea surface, we introduced the dissociation constants'

Acid	$-a_0$ $\frac{m^3}{mol}$	a_1 $\frac{m^3}{°C\ mol}$	$a_2 \times 10^3$ $\frac{m^3}{°C^2 mol}$	$-b_0$ $\frac{m^3}{Pa\ mol}$	b_1 $\frac{m^3}{Pa\ °C\ mol}$
H_2CO_3	25.50	0.1271		3.08	0.0877
HCO_3^-	15.82	−0.0219		−1.13	−0.1475
$B(OH)_3$	29.48	−0.1622	−2.608	2.84	
H_2O	25.60	0.2324	−3.6246	5.13	0.0794
HSO_4^-	18.03	0.0466	0.316	4.53	0.0900

Table 5.1: Pressure dependent coefficients for the dissociation constants of acids in seawater, after Millero [1995]. For boric acid, $a_2 \times 10^3$ has been changed from 2.608 to −2.608 ($m^3\ °C^{-2}\ mol^{-1}$) [Rae et al., 2011].

pressure dependence based on Millero [1995]:

$$ln\left(\frac{K_i^P}{K_i^0}\right) = -\left(\frac{\Delta V_i}{RT}\right)P + 0.5\left(\frac{\Delta \kappa_i}{RT}\right)P^2, \tag{5.11}$$

where K_i is the dissociation constant for reaction i between two carbonate system species, P the pressure in bars, R = 8.314 m^3 Pa K^{-1} mol^{-1} the gas constant, T the absolute temperature in Kelvin, ΔV_i the associated molal volume change in (m^3 mol^{-1}), and $\Delta \kappa_i$ the associated compressibility change in (m^3 Pa^{-1} mol^{-1}). The latter two are calculated as follows:

$$\Delta V_i = a_0 + a_1 T_c + a_2 T_c^2 \tag{5.12}$$

and

$$\Delta \kappa_i = b_0 + b_1 T_c, \tag{5.13}$$

where T_c is temperature in °C and the coefficients are shown in Table 5.1. Additionally, we could remove the original model's symbiotic algae component, since deep-sea benthic foraminifera do not host photosynthesising symbionts.

5.3.3 Coupling to HAMOCC2s

In order to calculate the bulk concentrations of the different carbonate system species, the FCM takes the following input parameters from the HAMOCC2s output: temperature, salinity, pressure, total alkalinity or DIC, pH, $\delta^{13}C_{DIC}$, and $\delta^{13}C_{POC}$.

Chapter 6

Sediment core δ^{13}C data

Drilling sediment cores and analysing the sedimentary material in them is a long established technique that marine geologists use to assess palaeoclimate. As more and more cores have been drilled and analysed over the years, the spatial coverage across the world's oceans has increased substantially, especially in the Atlantic Ocean. This is a welcome development for the climate modelling community as it means that there are more, and more widely distributed observational data available that can be compared to climate models. Since measuring δ^{13}C values of foraminiferal shells is a common procedure when analysing sedimentary material, lots of δ^{13}C records are available. So in order to be able to compare model output to observations (see Chapters 7 and 9), we established a database of δ^{13}C values in the Atlantic Ocean.

We combined carbon isotope data from various compilations (Sarnthein et al. [1994], Bickert and Mackensen [2004], Curry and Oppo [2005], Marchal and Curry [2008]), and from the PANGAEA and National Climatic Data Center databases (http://www.pangaea.de and http://www.ncdc.noaa.gov/paleo). As far as possible the original authors within the compilations were traced back and referenced. We only considered sediment cores containing *C. wuellerstorfi* which is known to be the most reliable recorder of $\delta^{13}C_{DIC}$ in the ocean [Woodruff et al., 1980;

Belanger et al., 1981; Zahn et al., 1986; Hodell et al., 2001]. Some cores include a few other benthic species (*Planulina ariminensis* or *C. kullenbergi*), which are also used as they are thought to have an epibenthic habitat, too [Lutze and Thiel, 1989].

For each core we calculated the average δ^{13}C value of the Late Holocene (LH) and LGM time slice (see below). Phytodetritus corrections like those used in Bickert and Mackensen [2004] were not applied to any of the data. We corrected the depth at which sediment cores were drilled by 120 meters in order to account for changes in sea level at the LGM [Fairbanks, 1989]. The final dataset is shown in Table 6.1 and available at the PANGAEA database (doi:10.1594/PANGAEA.758334).

To test whether $\delta^{13}C_{DIC} = \delta^{13}C_{foram}$ we used sediments from the LH (0-4 ka BP[1]). Although there is evidence for variations in δ^{13}C during the Holocene period [Oppo et al., 2003], our LH dataset compares well with $\delta^{13}C_{DIC}$ measurements taken from GEOSECS and collected in the Global Ocean Data Analysis Project (GLODAP). Calculations on a subset of 58 cores in this period yielded an average standard deviation of δ^{13}C of 0.16‰ VPDB (see Section 7.1).

Here our definition of the LGM extends from 18-24 ka. Previously, authors have used different time constraints for the LGM, e.g. Curry and Oppo [2005] considered data from 18 to 21 ka BP (following the maximum positive peak in δ^{18}O), whereas Bickert and Mackensen [2004] used the time interval from 19-23 ka BP (i.e. the glacial sea level lowstand [Mix et al., 2001]). Other authors extended this range even further to 24 ka [Ninnemann and Charles, 2002] or 26.5 ka [Clark et al., 2009]. Calculations on a subset of 64 cores (from PANGAEA) show that the average standard deviation of δ^{13}C within the cores used is 0.15‰ VPDB for the 18-24 ka range. Since this only represents a minor δ^{13}C variation during the LGM we believe that our definition is justified. Age models for each core were taken from the original investigator(s).

[1]BP = before present; present = 1950

Table 6.1: Sediment core information

Station	Latitude	Longitude	Depth	Late Holocene			Last Glacial Maximum			Precision	Age model	Reference
				δ^{13}C	SD	n	δ^{13}C	SD	n			
	°*North*	°*East*	*meters*	‰ *VPDB*	‰ *VPDB*		‰ *VPDB*	‰ *VPDB*		‰ *VPDB*		
108-658	20.75	−18.58	2274	0.83	0.09	5	0.51	0.05	15	0.04	C-14 control pts, O-18 cor	Tiedemann [1991]
108-659	18.08	−21.03	3082	0.98	0.22	2	0.23	0.13	4	0.04	C-14 control pts, O-18 cor	Tiedemann [1991]
162-980	55.48	−14.70	2180	0.98	0.14	18	0.82	0.11	7	0.04	O-18 SPECMAP cor	McManus et al. [1999]
162-982*	57.20	−15.88	1145	0.98	0.10	7	1.40	0.06	3	0.05	O-18 cor	Venz et al. [1999]
175-1084[b,f]	−25.51	13.03	1992	0.47			0.25			0.06	no info	Lynch-Stieglitz et al. [2006]
175-1085A[e]	−29.37	13.99	1713	0.87			0.57			0.05	O-18 SPECMAP cor	Bickert and Mackensen [2004], [Vidal (unpubl.)]
175-1087A	−31.46	15.31	1372	0.44	0.11	4	0.40	NA	1	0.02	O-18 cor, interp	Pierre et al. [2001]
68-502_Site	11.49	−79.38	3051	0.87	NA	1	1.29	NA	1	0.04	O-18, paleomag, orbital	deMenocal et al. [1992]
AII60-13APC	−31.99	−36.65	3739	1.18	0.15	2				0.11	O-18 cor	Curry and Lohmann [1982]
ALB-226[e]	17.95	−21.05	3100	0.88			0.19			0.05	O-18 SPECMAP cor	Sarnthein et al. [1994]
BOFS11K	55.19	−20.35	2004	1.43	NA	1				0.10	O-18 cor on C-14 core BOFS5K	Bertram et al. [1995]
BOFS14K	58.63	−19.43	1756	0.95	0.10	2	1.44	0.07	9	0.10	O-18 cor on C-14 core BOFS5K	Bertram et al. [1995]
BOFS26/6K	24.45	−19.84	3680	1.00	0.08	2	0.30	0.14	6	0.10	O-18 cor on C-14 BOFS core	Beveridge et al. [1995]
BOFS28/3M	24.62	−22.76	4900	1.02	0.08	2	0.01	NA	1	0.10	O-18 cor on C-14 BOFS core	Beveridge et al. [1995]
BOFS29/1K	20.52	−21.12	4000	0.80	0.07	3	0.02	0.04	5	0.10	O-18 cor on C-14 BOFS core	Beveridge et al. [1995]
BOFS30/3K	19.75	−20.72	3580	0.96	0.04	2	0.21	0.09	5	0.10	O-18 cor on C-14 BOFS core	Beveridge et al. [1995]
BOFS31/1K	19.00	−20.16	3300	0.92	0.06	3	0.23	0.06	7	0.10	O-18 cor on C-14 BOFS core	Beveridge et al. [1995]
BOFS5K[c,f]	51.00	−22.00	3547	1.02			0.50			0.10	C-14	Bertram et al. [1995]
CH71-07[e]	4.38	−20.87	3083	1.08			0.32			0.05	O-18 SPECMAP cor	Sarnthein et al. [1994]
CH73-139C	54.63	−16.35	2209	0.94	0.03	5	0.54	0.19	5	0.10	C-14	Duplessy [1982]
CHN115-70PC	−29.92	−35.66	2340	0.96	0.15	2	0.77	NA	1	0.11	O-18 cor	Curry and Lohmann [1982]
CHN115-88PC	−30.92	−36.08	2941	0.68	NA	1	0.34	0.1	2	0.11	O-18 cor	Curry and Lohmann [1982]
CHN115-89PC	−30.88	−38.20	3152				0.36	0.29	3	0.11	O-18 cor	Curry and Lohmann [1982]
CHN115-90PC	−30.85	−38.37	3384				0.22	NA	1	0.11	O-18 cor	Curry and Lohmann [1982]
CHN115-91PC	−30.83	−38.43	3576	0.46	0.22	2	0.29	NA	1	0.11	O-18 cor	Curry and Lohmann [1982]
CHN115-92PC	−30.84	−38.84	3934				−0.43	NA	1	0.11	O-18 cor	Curry and Lohmann [1982]
CHN82-24*	43.47	−30.66	3070	1.08	0.16	7	0.59	0.11	3	0.10	O-18 cor	Boyle and Keigwin [1985]
CHN824115[e]	43.37	−28.23	2151				1.20			0.10	O-18 cor	Boyle and Keigwin [1987]
DSDP-552[d]	56.05	−23.23	2311				0.90			0.05	palaeomag	Sarnthein et al. [1994]
EN066-0010PG	6.64	−21.90	3527	0.82	NA	1	0.46	0.09	2	0.10	O-18 cor on V19-30	Curry and Lohmann [1982]
EN066-0016PG	5.45	−21.14	3160	0.94	NA	1	0.39	0.06	4	0.10	O-18 cor on V19-30	Curry and Lohmann [1982]
EN066-0021PG	4.23	−20.63	3792	0.80	0.04	2	0.16	0.05	2	0.10	O-18 cor on V19-30	Curry and Lohmann [1982]
EN066-0026PG	3.09	−20.02	4745	0.84	NA	1	−0.03	0.18	2	0.10	O-18 cor on V19-30	Curry and Lohmann [1982]
EN066-0029PG	2.46	−19.76	5105	0.84	0.01	2	−0.16	NA	1	0.10	O-18 cor on V19-30	Curry and Lohmann [1982]
EN066-0032PG	2.47	−19.73	4998	0.86	NA	1	−0.07	0.20	3	0.10	O-18 cor on V19-30	Curry and Lohmann [1982]
EN066-0036PG	4.31	−20.21	4095	0.75	0.34	2	0.12	0.09	2	0.10	O-18 cor on V19-30	Curry and Lohmann [1982]
EN066-0038PG	4.92	−20.50	2937	1.04	0.09	2	0.69	NA	1	0.10	O-18 cor on V19-30	Curry and Lohmann [1982]
EN066-0044PG	5.26	−21.71	3423				0.46	0.07	3	0.10	O-18 cor on V19-30	Curry and Lohmann [1982]

Table 6.1: (cont.)

Station	Latitude	Longitude	Depth	Late Holocene			Last Glacial Maximum			Precision	Age model	Reference
				δ^{13}C	SD	n	δ^{13}C	SD	n			
	°*North*	°*East*	*meters*	‰ *VPDB*	‰ *VPDB*		‰ *VPDB*	‰ *VPDB*		‰ *VPDB*		
EN120-1GGC[b,d]	33.67	−57.62	4450	0.30			−0.30			0.10	O-18 cor on C-14 core KNR31-GPC5	Boyle and Keigwin [1987]
EW9302-14JPC[d]	61.42	−24.11	1653				1.50			0.03	O-18 SPECMAP cor, magn susc.	Oppo et al. [1997]
GeoB1028-5	−20.10	9.19	2209	0.62	0.12	2	0.13	0.16	2	0.05	C-14	Bickert and Mackensen [2004]
GeoB1031-4	−21.88	7.10	3105	0.76	NA	1	0.21	0.18	3	0.05	O-18 SPECMAP cor	Sarnthein et al. [1994]
GeoB1032-2/3	−22.92	6.04	2505	0.90	0.06	3	0.00	0.14	2	0.05	O-18 SPECMAP cor	Bickert and Wefer [1996]
GeoB1034-1/3	−21.74	5.42	3772	0.57	0.29	3	0.05	0.03	2	0.05	O-18 SPECMAP cor	Bickert and Wefer [1996]
GeoB1035-3/4	−21.59	5.03	4456	0.74	0.21	2	−0.13	0.04	2	0.05	O-18 SPECMAP cor	Bickert and Wefer [1996]
GeoB1041-1/3	−3.48	−7.60	4033	0.78	0.12	7	−0.34	0.25	3	0.05	O-18 SPECMAP cor	Bickert and Wefer [1996]
GeoB1101-4/5	1.66	−10.98	4588	0.91	0.17	3	−0.64	NA	1	0.05	O-18 SPECMAP cor	Bickert and Wefer [1996]
GeoB1105-3/4	−1.67	−12.43	3225	0.98	0.12	6	−0.16	0.12	11	0.05	O-18 SPECMAP cor	Bickert and Wefer [1996]
GeoB1112-3/4	−5.78	−10.75	3125	0.82	0.20	3	0.37	0.10	4	0.05	O-18 SPECMAP cor	Bickert and Wefer [1996]
GeoB1113	−5.75	−11.04	2374	0.93			0.44			0.05	O-18 SPECMAP cor	Sarnthein et al. [1994]
GeoB1115-3/4	−3.56	−12.56	2921	1.02	0.06	9	0.01	0.13	5	0.05	O-18 SPECMAP cor	Bickert and Wefer [1996]
GeoB1117-2/3	−3.82	−14.90	3984	0.78	0.19	9	−0.41	0.11	7	0.05	O-18 SPECMAP cor	Bickert and Wefer [1996]
GeoB1118-2/3	−3.56	−14.90	4675	0.24	0.37	4	−0.44	0.15	6	0.05	O-18 SPECMAP cor	Bickert and Wefer [1996]
GeoB1211-1/3	−24.47	7.53	4084	0.24	0.34	3	0.25	NA	1	0.05	O-18 SPECMAP cor	Bickert and Wefer [1996]
GeoB1214-1/2	−24.69	7.24	3210	0.68	0.01	2	0.22	0.01	2	0.05	O-18 SPECMAP cor	Bickert and Wefer [1996]
GeoB1220-1	−24.03	5.31	2265				0.46	0.12	2	0.05	O-18 SPECMAP cor	Bickert and Mackensen [2004]
GeoB1306-1/2	−35.21	−26.76	4057				−0.39	0.08	2	0.05	O-18 SPECMAP cor	Bickert and Mackensen [2004]
GeoB1312-2	−31.66	−29.65	3436				0.11	NA	1	0.05	O-18 SPECMAP cor	Bickert and Mackensen [2004]
GeoB1417-1	−15.54	−12.71	2845				0.49	0.07	4	0.05	O-18 SPECMAP cor	Bickert and Mackensen [2004]
GeoB1419-2	−15.54	−17.07	4024				0.11	0.14	2	0.05	O-18 SPECMAP cor	Bickert and Mackensen [2004]
GeoB1501-4	−3.68	−32.01	4257				0.05	0.18	4	0.05	O-18 SPECMAP cor	Bickert and Mackensen [2004]
GeoB1503-1	2.31	−30.65	2306				0.77	0.10	4	0.05	O-18 SPECMAP cor	Bickert and Mackensen [2004]
GeoB1505-1/2	2.27	−33.01	3705	0.91			−0.13			0.07	O-18 SPECMAP cor	Zabel et al. [1999]
GeoB1508-4	5.33	−34.03	3682	0.87	NA	1	0.27	0.12	4	0.05	O-18 SPECMAP cor	Bickert and Mackensen [2004]
GeoB1515-1/2	4.24	−43.67	3129	1.26	0.23	4	0.41	0.20	10	0.05	C-14	Vidal et al. [1999]
GeoB1520-1/2	4.59	−41.93	3911	0.66	0.36	3	0.10	0.16	4	0.05	O-18 SPECMAP cor	Bickert and Mackensen [2004]
GeoB1523-1/2	3.83	−41.62	3291	1.30	0.05	3	0.49	0.06	4	0.05	O-18 SPECMAP cor	Bickert and Mackensen [2004]
GeoB1710-2/3	−23.43	11.70	2987	0.61	0.10	6	−0.29	0.15	9	0.05	O-18 SPECMAP cor	Bickert and Wefer [1999]
GeoB1711-4/5	−23.32	12.38	1967	0.64	0.22	8	0.23	0.16	11	0.05	O-18 SPECMAP cor	Bickert and Wefer [1999]
GeoB1721-6/7	−29.17	13.08	3044	0.43	0.19	3	−0.09	0.19	3	0.05	O-18 SPECMAP cor	Bickert and Mackensen [2004]
GeoB1722-1/3	−29.45	11.75	3973	0.29	0.24	3	−0.13	0.06	2	0.05	O-18 SPECMAP cor	Mollenhauer et al. [2002]
GeoB1903-3	−8.68	−11.85	3161				0.35	0.07	4	0.05	O-18 SPECMAP cor	Bickert and Mackensen [2004]
GeoB1905-3	−17.14	−13.99	2974				0.66	0.04	2	0.05	O-18 SPECMAP cor	Bickert and Mackensen [2004]
GeoB2004-2	−30.87	14.34	2569	0.80	0.04	2	−0.10	0.08	6	0.05	O-18 SPECMAP cor	Bickert and Mackensen [2004]
GeoB2016-1	−31.90	−1.33	3385	0.64	NA	1	0.38	0.06	2	0.05	O-18 SPECMAP cor	Bickert and Mackensen [2004]
GeoB2019-1	−36.06	−8.78	3825				0.11	0.16	3	0.05	O-18 SPECMAP cor	Bickert and Mackensen [2004]

Table 6.1: (cont.)

Station	Latitude	Longitude	Depth	Late Holocene			Last Glacial Maximum			Precision	Age model	Reference
				δ^{13}C	SD	n	δ^{13}C	SD	n			
	°*North*	°*East*	*meters*	‰ *VPDB*	‰ *VPDB*		‰ *VPDB*	‰ *VPDB*		‰ *VPDB*		
GeoB2109-1	−27.91	−45.88	2504	1.23	0.11	2	0.25	0.32	4	0.05	O-18 SPECMAP cor	Vidal et al. [1999]
GeoB2204-1/2	−8.53	−34.02	2072	1.26	0.01	3	0.24	NA	1	0.05	O-18 SPECMAP cor	Bickert and Mackensen [2004]
GeoB2215-10	0.01	−23.50	3711				0.05			0.05	O-18 SPECMAP cor	Bickert and Mackensen [2004]
GeoB2819-1	−30.85	−38.34	3435				0.15	0.16	2	0.05	O-18 SPECMAP cor	Bickert and Mackensen [2004]
GeoB3104-1	−3.67	−37.72	767	1.43			0.90			0.05	C-14	Arz et al. [1998]
GeoB3603-2	−35.13	17.54	2840	0.55	NA	1	0.14	0.05	2	0.05	O-18 SPECMAP cor	Bickert and Mackensen [2004]
GeoB3722-2	−25.25	12.02	3506	0.69			−0.21			0.05	O-18 SPECMAP cor	Mollenhauer et al. [2002]
GeoB3801-6	−29.51	−8.31	4546	0.55	NA	1	−0.12	NA	1	0.05	O-18 SPECMAP cor	Bickert and Mackensen [2004]
GeoB3808-6	−30.81	−14.71	3213	1.01			0.57	0.12	5	0.05	O-18 SPECMAP cor	Bickert and Mackensen [2004]
GeoB3813-3	−32.27	−21.97	4331	0.55			0.08	NA	1	0.05	O-18 SPECMAP cor	Bickert and Mackensen [2004]
GeoB4216-1	30.63	−12.40	2324	1.05	NA	1	0.51	0.14	11	0.05	O-18 SPECMAP cor	Freudenthal et al. [2002]
GeoB4240-2	28.89	−13.23	1358				1.06	0.24	7	0.05	O-18 SPECMAP cor	Freudenthal et al. [2002]
GeoB4403-2	6.13	−43.44	4503	0.64	0.29	5	−0.09	0.12	8	0.05	O-18 SPECMAP cor	Bickert and Mackensen [2004]
GeoB5115-2	−24.14	−14.04	3291	1.01	0.06	5	0.70	0.14	10	0.05	O-18 SPECMAP cor	Bickert and Mackensen [2004]
GeoB5121-2	−24.17	−12.36	3486	0.98			0.55			0.05	O-18 SPECMAP cor	Bickert and Mackensen [2004]
GeoB7920-2	20.75	−18.58	2278	0.76	0.15	8	0.48	0.08	11	0.05	O-18 cor on MD95 4024	Tjallingii et al. [2008]
GeoB9508-5	15.50	−17.95	2384	0.81	0.24	11	0.29	0.13	28	0.07	C-14	Mulitza et al. [2008]
GeoB9528-3	9.17	−17.66	3057				0.31	0.13	18	0.07	C-14	Castañeda et al. [2009]
GIK11944[e]	35.65	−8.06	1765	1.21			1.01			0.05	O-18 SPECMAP cor	Sarnthein et al. [1994]
GIK12309-2[e]	26.84	−15.11	2820	1.10			0.27			0.05	O-18 SPECMAP cor	Sarnthein et al. [1994]
GIK12310-3/4[e]	23.50	−18.72	3080	1.06			−0.07			0.05	O-18 SPECMAP cor	Sarnthein et al. [1994]
GIK12328[e]	21.15	−18.57	2778	0.86			0.35			0.05	O-18 SPECMAP cor	Sarnthein et al. [1994]
GIK12329-6[e]	19.37	−19.93	3320	0.82			0.20			0.05	O-18 SPECMAP cor	Sarnthein et al. [1994]
GIK12337-4/-5[a]	15.95	−18.13	3094	0.60						0.05	O-18 SPECMAP cor	Sarnthein et al. [1994]
GIK12345[e]	15.48	−17.36	945	0.75			0.92			0.05	O-18 SPECMAP cor	Sarnthein et al. [1994]
GIK12347-1/-2[a,d]	15.83	−17.86	2510	0.80			0.40			0.05	O-18 SPECMAP cor	Sarnthein et al. [1994]
GIK12379[e]	23.14	−17.75	2136	1.06			0.43			0.05	O-18 SPECMAP cor	Sarnthein et al. [1994]
GIK13239-1	13.88	−18.31	3156				0.07	0.14	11	0.05	O-18 SPECMAP cor	Sarnthein et al. [1994]
GIK13289[e]	18.07	−18.01	2490	0.95			0.50			0.05	C-14	Sarnthein et al. [1994]
GIK13519-1	5.67	−19.85	2862				0.47	0.05	5	0.05	Orbital, ?	Zahn et al. [1986]
GIK13521[e]	3.02	−22.03	4504				−0.42			0.05	O-18 SPECMAP cor	Sarnthein et al. [1994]
GIK15612[e]	44.69	−26.54	3050	1.24			0.51			0.05	O-18 SPECMAP cor	Sarnthein et al. [1994]
GIK15627-3	29.17	−12.09	1024				1.37	0.10	7	0.05	O-18 SPECMAP cor	Sarnthein et al. [1994]
GIK15637-1	27.01	−18.99	3849				0.04	NA	1	0.05	O-18 SPECMAP cor	Sarnthein et al. [1994]
GIK15666[e]	34.96	−7.12	803	1.27			1.76			0.05	O-18 SPECMAP cor	Sarnthein et al. [1994]
GIK15669-1	34.89	−7.82	2022	1.09	NA	1	0.88	0.09	27	0.05	O-18 SPECMAP cor	Sarnthein et al. [1994]
GIK15670-5[a,d]	34.91	−7.58	1482	1.00			1.30			0.05	O-18 SPECMAP cor	Sarnthein et al. [1994]
GIK15672-1/2[e]	34.86	−8.12	2455	1.14			0.65			0.05	O-18 SPECMAP cor	Sarnthein et al. [1994]

Table 6.1: (cont.)

Station	Latitude	Longitude	Depth	Late Holocene			Last Glacial Maximum			Precision	Age model	Reference
				δ^{13}C	SD	n	δ^{13}C	SD	n			
	°*North*	°*East*	*meters*	‰ *VPDB*	‰ *VPDB*		‰ *VPDB*	‰ *VPDB*		‰ *VPDB*		
GIK16004[e]	29.98	−10.65	1512	1.19			1.11			0.05	O-18 SPECMAP cor	Sarnthein et al. [1994]
GIK16006[e]	29.27	−11.50	796	1.20			1.48			0.05	O-18 SPECMAP cor	Sarnthein et al. [1994]
GIK16017[e]	21.25	−17.80	812	0.99			1.08			0.05	O-18 SPECMAP cor	Sarnthein et al. [1994]
GIK16030[e]	21.24	−18.06	1500	0.89			0.86			0.05	O-18 SPECMAP cor	Sarnthein et al. [1994]
GIK16402[e]	14.42	−20.57	4203	0.64			−0.18			0.05	O-18 SPECMAP cor	Sarnthein et al. [1994]
GIK16408[e]	9.01	−21.50	4336	0.71			−0.25			0.05	O-18 SPECMAP cor	Sarnthein et al. [1994]
GIK16415[e]	9.57	−19.11	3841	0.55			0.07			0.05	O-18 SPECMAP cor	Sarnthein et al. [1994]
GIK16453[e]	4.73	−20.95	2675	1.17			0.43			0.05	O-18 SPECMAP cor	Sarnthein et al. [1994]
GIK16455-1[a,d]	5.27	−22.87	4160	0.70			−0.10			0.05	O-18 SPECMAP cor	Sarnthein et al. [1994]
GIK16457-1	5.39	−21.72	3291	1.11	0.10	3	0.17	0.23	3	0.05	O-18 SPECMAP cor	Sarnthein et al. [1994]
GIK16458[e]	5.34	−22.06	3518	0.90			0.02			0.05	O-18 SPECMAP cor	Sarnthein et al. [1994]
GIK16459-1	7.28	−26.19	4835	0.58	0.18	2	−0.03	0.11	6	0.05	O-18 SPECMAP cor	Sarnthein et al. [1994]
GIK16771-2	0.82	−15.51	2764	1.26	NA	1	0.30	0.04	2	0.05	O-18 SPECMAP cor	Sarnthein et al. [1994]
GIK16772-1	−1.34	−11.97	3911	0.86	0.12	5				0.05	O-18 SPECMAP cor	Sarnthein et al. [1994]
GIK16772-2	−1.35	−11.96	3912				−0.25	0.07	3	0.05	O-18 SPECMAP cor	Sarnthein et al. [1994]
GIK16773-1[a]	−0.97	−9.44	4662	0.90						0.05	O-18 SPECMAP cor	Sarnthein et al. [1994]
GIK17045	52.43	−16.66	3663	0.79	0.07	4	0.17	0.15	10	0.05	C-14	Sarnthein et al. [1994]
GIK17048	54.31	−18.18	1859	1.28	0.10	9	1.14	0.15	8	0.05	O-18 SPECMAP cor	Sarnthein et al. [1994]
GIK17049	55.26	−26.73	3331	0.73	0.27	6	0.48	0.17	10	0.04	C-14, O-18 cor	Sarnthein et al. [1994]
GIK17050	55.47	−27.89	2795	0.51	NA	1	0.39	0.32	5	0.05	O-18 SPECMAP cor	Sarnthein et al. [1994]
GIK17051	56.16	−31.99	2295	1.02	0.03	2	0.84	0.15	14	0.04	C-14, O-18 cor	Sarnthein et al. [1994]
GIK17055-1	48.22	−27.06	2558	1.07	0.37	3	1.11	NA	1	0.05	O-18 SPECMAP cor	Winn et al. [1991]
GIK23258-2	75.00	13.97	1768	1.22	0.09	28				0.05	C-14	Sarnthein et al. [2003]
GIK23258-3	75.00	13.97	1781	1.13	0.10	40				0.05	C-14	Sarnthein et al. [2003]
GIK23414	53.54	−20.29	2196	1.13	NA	1	0.90	0.08	8	0.05	O-18 SPECMAP cor	Sarnthein et al. [1994]
GIK23415	53.18	−19.15	2472	1.10	0.12	9	0.55	0.15	13	0.04	C-14, O-18 cor	Jung [1996]
GIK23416	51.57	−20.00	3616	0.72	0.19	3	0.38	NA	1	0.04	C-14, O-18 cor	Jung [1996]
GIK23417	50.67	−19.43	3850				0.19	0.18	7	0.04	C-14, O-18 cor	Jung [1996]
GIK23418	52.33	−20.33	2841	1.06	0.12	9	0.32	0.05	5	0.04	C-14, O-18 cor	Jung [1996]
GIK23419	54.96	−19.76	1491	1.25	0.08	2	1.47	0.25	13	0.05	O-18 SPECMAP cor	Sarnthein et al. [1994]
GIK23519-4	64.80	−29.60	1903	1.07	0.24	22				0.05	O-18 cor on C-14 core	Millo et al. [2006]
GIK23519-5	64.80	−29.60	1893				1.39	0.20	109	0.05	O-18 cor on C-14 core	Millo et al. [2006]
IOW226920-3[e]	−22.45	12.36	1683	0.22			0.39			0.05	C-14, O-18 cor	Mollenhauer et al. [2002]
KNR110-50	4.87	−43.21	3995	0.85	0.28	4	0.21	0.17	18	0.10	O-18 cor on V19-30	Curry et al. [1988]
KNR110-55	4.95	−42.89	4556	0.37	0.38	13	0.00	0.17	12	0.10	O-18 cor on V19-30	Curry et al. [1988]
KNR110-58	4.79	−43.04	4341	0.64	0.26	12	−0.01	0.12	7	0.10	O-18 cor on V19-30	Curry et al. [1988]
KNR110-66	4.56	−43.38	3547	0.78	0.30	11	0.20	0.27	10	0.10	O-18 cor on V19-30	Curry et al. [1988]
KNR110-71	4.36	−43.70	3164	1.12	0.12	5	0.43	0.23	13	0.10	O-18 cor on V19-30	Curry et al. [1988]

Table 6.1: (cont.)

Station	Latitude	Longitude	Depth	Late Holocene			Last Glacial Maximum			Precision	Age model	Reference
				δ^{13}C	SD	n	δ^{13}C	SD	n			
	°*North*	°*East*	*meters*	‰ *VPDB*	‰ *VPDB*		‰ *VPDB*	‰ *VPDB*		‰ *VPDB*		
KNR110-75	4.34	−43.41	3063	0.99	0.40	5	0.29	0.23	13	0.10	O-18 cor on V19-30	Curry et al. [1988]
KNR110-82	4.34	−43.49	2816	1.09	0.16	4	0.30	0.25	16	0.10	O-18 cor on V19-30	Curry et al. [1988]
KNR110-91	4.76	−43.31	3810	0.72	0.25	6	0.10	0.18	11	0.10	O-18 cor on V19-30	Curry et al. [1988]
KNR140-12JPC[d]	29.08	−72.90	4250				−0.50			no info	C-14	Keigwin [2004]
KNR140-1JPC[b]	32.38	−76.38	2243	1.00						no info	no info	Keigwin [2004]
KNR140-22JPC[b,d]	28.03	−74.41	4712	1.20			−0.30			no info	C-14	Keigwin [2004]
KNR140-28GGC[b,d]	30.10	−73.84	4211	0.40			−0.50			no info	C-14	Keigwin [2004]
KNR140-29GGC[b]	30.02	−73.60	3978	1.00						no info	no info	Keigwin [2004]
KNR140-2JPC[d]	32.23	−76.29	2394				0.40			no info	C-14	Keigwin [2004]
KNR140-30GGC[b]	30.73	−74.47	3433	0.50						no info	no info	Keigwin [2004]
KNR140-37JPC[b,d]	31.69	−75.43	2972	0.90			0.40			no info	C-14	Keigwin and Schlegel [2002]
KNR140-39GGC[b,d]	31.67	−75.42	2975	1.40			0.30			no info	C-14	Keigwin and Schlegel [2002]
KNR140-43GGC[b,d]	32.02	−76.07	2590	1.10			0.90			no info	C-14	Keigwin [2004]
KNR140-51GGC[b,d]	32.78	−76.12	1790	0.90			1.20			no info	C-14	Keigwin [2004]
KNR140-64GGC[d]	32.74	−76.13	2101				1.20			no info	C-14	Keigwin [2004]
KNR140-66GGC[b]	32.50	−76.29	2155	1.00						no info	no info	Keigwin [2004]
KNR140-67JPC[d]	32.74	−76.13	2102				1.50			no info	C-14	Keigwin [2004]
KNR64-5[b,d]	16.52	−74.81	3047	1.00			1.20			no info	no info	Boyle and Keigwin [1987]
KW-31*[,e]	3.52	5.57	1515	0.69			0.48			0.05	O-18 SPECMAP cor	Sarnthein et al. [1994]
LYII-13A[e]	35.97	−7.82	1201				1.57			0.05	O-18 SPECMAP cor	Sarnthein et al. [1994]
M12392	25.17	−16.85	2575	1.00	0.12	10	0.35	0.13	12	0.10	O-18 SPECMAP cor	Shackleton [1977]; Zahn et al. [1986]
M35003*[,b,d]	12.09	−61.24	1299	0.90			1.20			0.02	C-14, O-18 SPECMAP cor	Zahn and Stüber [2002]
MD95-2039	40.58	−10.35	3381	0.92	0.16	3	0.11	0.07	38	0.02	C-14	Schönfeld et al. [2003]
MD95-2040	40.58	−9.86	2465	1.07	0.10	4	0.54	0.08	7	0.02	C-14	Schönfeld et al. [2003]
MD99-2334	37.80	−10.17	3166	0.97	0.04	5	0.18	0.16	21	0.06	C-14	Skinner and Shackleton [2004]
MG-237[f]	−5.20	11.33	1000	−0.11			−0.10			0.04	no info	Sarnthein et al. [1994]
NA87-22[e]	55.50	−14.70	2161	1.08			0.86			0.05	O-18 SPECMAP cor	Sarnthein et al. [1994]
OCE205-100GGC[b,d]	26.06	−78.03	1057	1.50			1.50			0.03	C-14	Slowey and Curry [1995]
OCE205-33GGC*[,b,d]	26.22	−77.67	783	1.20			1.70			0.03	C-14	Slowey and Curry [1995]
PS1243-1	69.37	−6.55	2711	1.41	0.04	5	1.08	0.27	11	0.04	C-14	Bauch et al. [2001]
PS1754-3[e]	−46.77	7.60	2476	0.54			−0.33			0.05	O-18 SPECMAP cor	Mackensen et al. [1994]
PS2082-1[e]	−43.22	11.75	4661	0.15			−0.68			0.05	O-18 SPECMAP cor	Mackensen et al. [1994]
PS2212-3	82.02	15.67	2531	1.42	NA	1				0.06	O-18 SPECMAP cor	Wollenburg et al. [2001]
RC13-229*	−25.49	11.31	4191	0.30	0.11	8	−0.38	0.13	13	0.10	O-18 cor on V19-30	Curry (2004, Pangaea)
RC15-93*[b,d]	−46.10	−13.22	2714	0.30			−1.00			no info	O-18 SPECMAP cor	Ninnemann and Charles [2002]
RC15-94*[,b,d]	−42.98	−20.85	3762	−0.20			−0.80			no info	O-18 SPECMAP cor	Ninnemann and Charles [2002]
RC16-119[e]	−27.70	−46.52	1567	1.10			0.59			0.03	C-14, O-18 SPECMAP cor	Oppo and Horowitz [2000]
RC16-84[e]	−26.70	−43.33	2438	1.08			0.16			0.03	C-14, O-18 SPECMAP cor	Oppo and Horowitz [2000]

Table 6.1: (cont.)

Station	Latitude	Longitude	Depth	Late Holocene			Last Glacial Maximum			Precision	Age model	Reference
				δ^{13}C	SD	n	δ^{13}C	SD	n			
	°*North*	°*East*	*meters*	‰ *VPDB*	‰ *VPDB*		‰ *VPDB*	‰ *VPDB*		‰ *VPDB*		
SO82_5-2	59.19	−30.90	1416				1.64	0.23	28	0.04	C-14, O-18 cor	Jung [1996]
SU92-21[e]	36.57	−23.74	4170				0.04			0.05	O-18 SPECMAP cor	Sarnthein et al. [1994]
T86-15P[e]	30.43	−37.07	3375	1.15			0.47			0.05	O-18 SPECMAP cor	Sarnthein et al. [1994]
TN057-20[*,b,d]	−42.00	1.00	1335	0.60			0.40			no info	O-18 SPECMAP cor	Ninnemann and Charles [2002]
TN057-21[*,b,d]	−41.13	7.82	4981	0.30			−0.80			no info	O-18 SPECMAP cor	Ninnemann and Charles [2002]
TTN057-6	−42.91	8.90	3702	0.50	NA	1	−0.44	0.25	2	0.01	O-18 SPECMAP cor	Hodell et al. [2003]
V12-70[*,b,f]	−6.48	11.43	450	0.58			0.59			0.06	no info	Lynch-Stieglitz et al. [2006]
V16-51[b,f]	−33.47	17.03	898	0.83			0.90			0.06	no info	Lynch-Stieglitz et al. [2006]
V19-236[f]	−33.88	17.63	280				1.50			0.06	no info	Lynch-Stieglitz et al. [2006]
V19-258[b,f]	−20.40	11.62	965	0.59			0.54			0.06	no info	Lynch-Stieglitz et al. [2006]
V19-259[b,f]	−19.87	11.03	1170	0.61			0.48			0.06	no info	Lynch-Stieglitz et al. [2006]
V22-108[*,b,d]	−43.18	−3.25	4171	0.10			−0.80			no info	O-18 SPECMAP cor	Ninnemann and Charles [2002]
V23-100[e]	21.30	−21.68	4579	0.59			0.07			0.05	O-18 SPECMAP cor	Sarnthein et al. [1994]
V23-81[e]	54.25	−16.83	2393	0.93			0.08			0.05	C-14	Sarnthein et al. [1994]
V24-253[e]	−26.95	−44.68	2069	1.10			0.08			0.05	C-14	Oppo and Horowitz [2000]
V25-59	1.37	−33.48	3824	0.89	0.06	5	0.02	0.11	4	0.06	C-14	Mix and Fairbanks [1985]
V26-176[*]	36.05	−72.38	3942	0.90	0.22	7	0.36	0.26	2	0.10	O-18 cor on V19-30	Curry et al. [1988]
V27-60[a]	72.18	8.58	2525	1.20						0.10	no info	Duplessy (WDCA)
V27-86[a]	66.57	1.12	2900	1.40						0.10	no info	Duplessy (WDCA)
V28-122[b,d]	11.93	−78.68	3623	0.77	0.12	8	1.15	0.07	7	no info	O-18 cor on V19-30, V35-04	Oppo and Fairbanks [1987]
V28-127[b,d]	11.65	−80.13	3237	0.75	0.13	6	1.18	0.07	8	no info	O-18 cor on V19-30, V35-04	Oppo and Fairbanks [1987]
V28-14	64.78	−29.57	1855	0.91	NA	1	1.22	0.22	6	0.10	O-18 cor on V19-30	Curry et al. [1988]
V28-73[b,d]	57.18	−20.87	2063	1.20			1.20			0.05	no info	Oppo and Lehman [1993]
V29-135[e]	−19.60	8.88	2675	0.65			0.12			0.05	O-18 SPECMAP cor	Sarnthein et al. [1994], [Abrantes (unpubl.)]
V29-193[*,e]	55.00	−19.00	1326	1.32			1.58			0.05	O-18 SPECMAP cor	Sarnthein et al. [1994]
V29-198[*,b,d]	58.73	−15.57	1139	1.10			1.40			0.05	no info	Oppo and Lehman [1993]
V29-202[b,d]	60.38	−20.97	2658	0.80			0.50			0.03	O-18 SPECMAP cor, magn susc.	Oppo et al. [1997]
V29-253[b,d]	−26.95	−44.68	2069	1.27			0.62			0.03	C-14, O-18 cor	Oppo and Horowitz [2000]
V30-40[e]	−0.20	−23.15	3706	0.91	NA	1	−0.11	0.04	3	0.05	O-18 SPECMAP cor	Sarnthein et al. [1994]
V30-49	18.43	−21.08	3093	0.86	0.06	3	0.24	0.16	7	0.06	C-14	Mix and Fairbanks [1985]

[*] species other than *C. wuellerstorfi*: *C. kullenbergi, Planulina ariminensis*)

[a] Late Holocene definition 0-3 ka

[b] Core-top value

[c] Other Late Holocene definition: BOFS5K (Holocene value)

[d] LGM definition 18-21 ka

[e] LGM definition 19-23 ka

[f] Other LGM definition: 175-1084 (δ^{18}O maximum), BOFS5K (Glacial value), MG-237 (18.3-19.3 ka), V12-70, V16-51, V19-236, V19-258, V19-259 (all δ^{18}O maximum)

Chapter 7

A model-data comparison of δ^{13}C in the glacial Atlantic Ocean

The study in this chapter is testing in numerical sensitivity experiments which AMOC scenario could be reconciled with observed modern and past δ^{13}C distributions in the Atlantic Ocean, and infering the climatic conditions and processes acting in the Atlantic Ocean during the LGM. For doing so, we compare three different LGM scenarios with a δ^{13}C dataset of 220 sediment cores. The models used are the LSG ocean circulation model and the HAMOCC2s carbon cycle model as described in Chapter 5. The δ^{13}C dataset is further described in Chapter 6.

The model-data comparison was done in three steps: First, the control simulation was compared to LH data. For comparing the sediment data with the model output, we found the model grid point that is closest to a sediment core and compared the two δ^{13}C values. Cores that were not within 500 km (meridionally), 1100 km (zonally) and 500 m depth of a model grid point were removed from the comparison, leaving 201 cores. One model grid point may correspond to more than one sediment core. The spatial limits of the comparison were chosen, such that we could impose reasonable oceanographic boundaries whilst at the same time keeping a maximum

number of sediment cores (note that the limits for the control run δ^{13}C to LH $\delta^{13}C_{foram}$ comparison are different from that of the present-day $\delta^{13}C_{DIC}$ to LH $\delta^{13}C_{foram}$ comparison below). Second, we compared the absolute values of both, the LGM model runs and the LGM sediment data. Third, we looked at the δ^{13}C differences (anomalies, or $\Delta\delta^{13}$C) between our control run and the three glacial runs, and compared them to the difference between LH and LGM sediment data.

7.1 Comparison of $\delta^{13}C_{DIC}$ data and Late Holocene sediment data

In order to estimate the uncertainty in LH $\delta^{13}C_{foram}$ values, we considered the $\delta^{13}C_{DIC}$ values as compiled by Kroopnick [1985] and measurements by P. Quay (University of Washington, collected in the GLODAP v1.1 bottle data set [Key et al., 2004; Sabine et al., 2005]). We calculated the Root Mean Square (RMS) difference between each DIC measurement which falls within a box of 500 km (meridionally) by 750 km (zonally) horizontally, by 250 m depth away from a sediment core measurement. These limits maximise the amount of data points, while at the same time ensuring reasonable oceanographic boundaries. The average RMS differences for the remaining 173 (GLODAP) and 200 (GEOSECS) measurements are 0.15 and 0.18‰ VPDB, respectively.

Figure 7.1 shows GLODAP δ^{13}C bottle data overlaying control run δ^{13}C as well as the δ^{13}C difference between control run and both, GLODAP data, and LH foraminifera. Model δ^{13}C values in the surface ocean and in the North Atlantic are higher compared to GLODAP. The control run underestimates the DIC measurements at intermediate depths around 1000 meters in the South Atlantic. This discrepancy will be addressed in detail below.

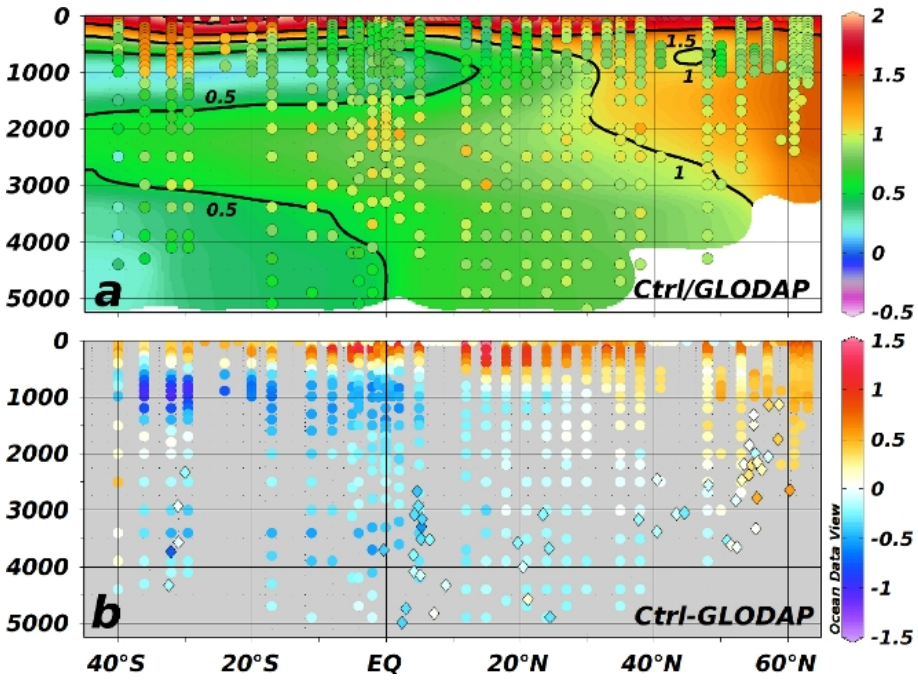

Figure 7.1: (a) Control run with GLODAP $\delta^{13}C_{DIC}$ bottle data overlay along the WHP A16 section, and (b) the difference in $\delta^{13}C$ between the control run and both, GLODAP $\delta^{13}C_{DIC}$ (circles), and Late Holocene $\delta^{13}C_{foram}$ values (diamonds).

7.2 Model-data comparison results

Results are presented along four sections. We consider two meridional sections, one in the East Atlantic, the other in the West Atlantic with the Mid-Atlantic Ridge being the dividing line (see Figure 7.2). Two zonal sections (see Appendix B) run in the North Atlantic at approximately 37.5°N (the section line follows World Ocean Circulation Experiment Hydrographic Programme (WHP) section A3) and the South Atlantic at 30°S (WHP section A10).

7.2.1 Control run

The AMOC of our control run shows a maximum positive overturning strength of 16 Sv at a depth of 1 km between 20-50°N (Figure 7.3a). There is a sharp gradient in flow strength above the Greenland-Scotland Ridge at 67°N. Negative transport rates are associated with inflow of

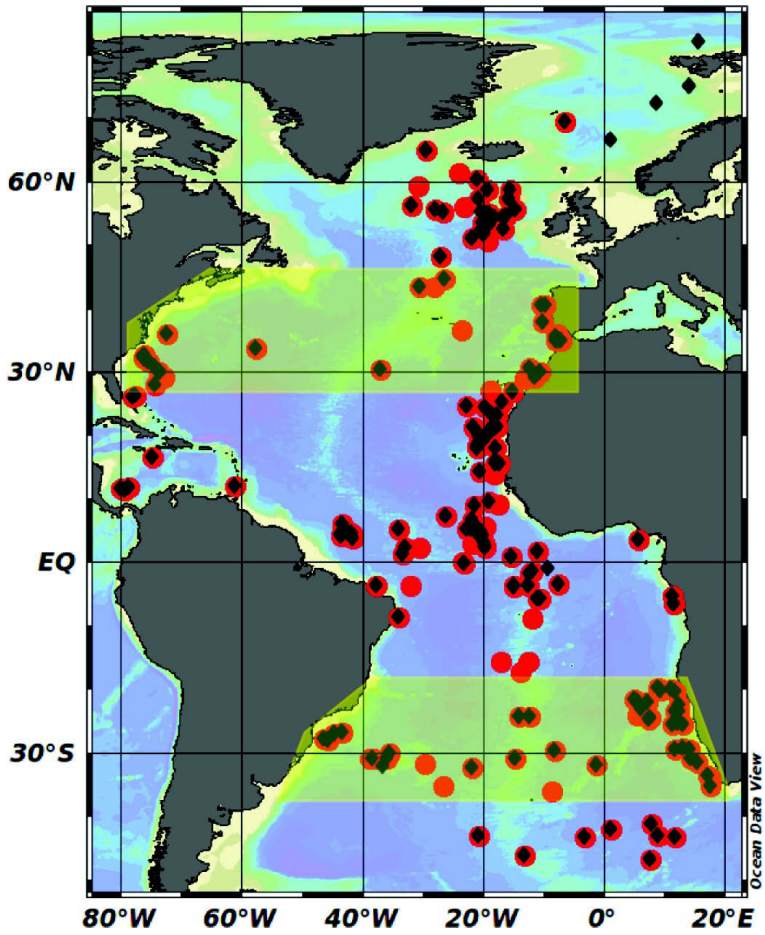

Figure 7.2: Sediment cores and section lines used in this study. Red dots (black diamonds) show core locations with Last Glacial Maximum (Late Holocene) δ^{13}C values. Meridional sections in the East and West Atlantic integrate data selected from east and west of the Mid-Atlantic Ridge, respectively. Zonal section lines and the area from which data are used in the North and South Atlantic are indicated in yellow (Figures S2 and S3 in supplementary material).

southerly-sourced water masses. CO_2 concentrations for the control run are at 283 ppmV.

The control run shows three distinct δ^{13}C signatures in the Atlantic Ocean (see Figure 7.4): high δ^{13}C water extends from the North Atlantic into the South Atlantic down to 40°S, the main signal being at depths between 1.5-3.5 km. Low δ^{13}C water dominates the Southern Ocean and reaches as far north as the equator at a depth of 4 km. Another low δ^{13}C signature is observed at depths of around 1 km in the Southern Ocean, which extends northward to 20°N. The zonal section in the South Atlantic (see Appendix B, Figure B.1) shows that a relatively high δ^{13}C body

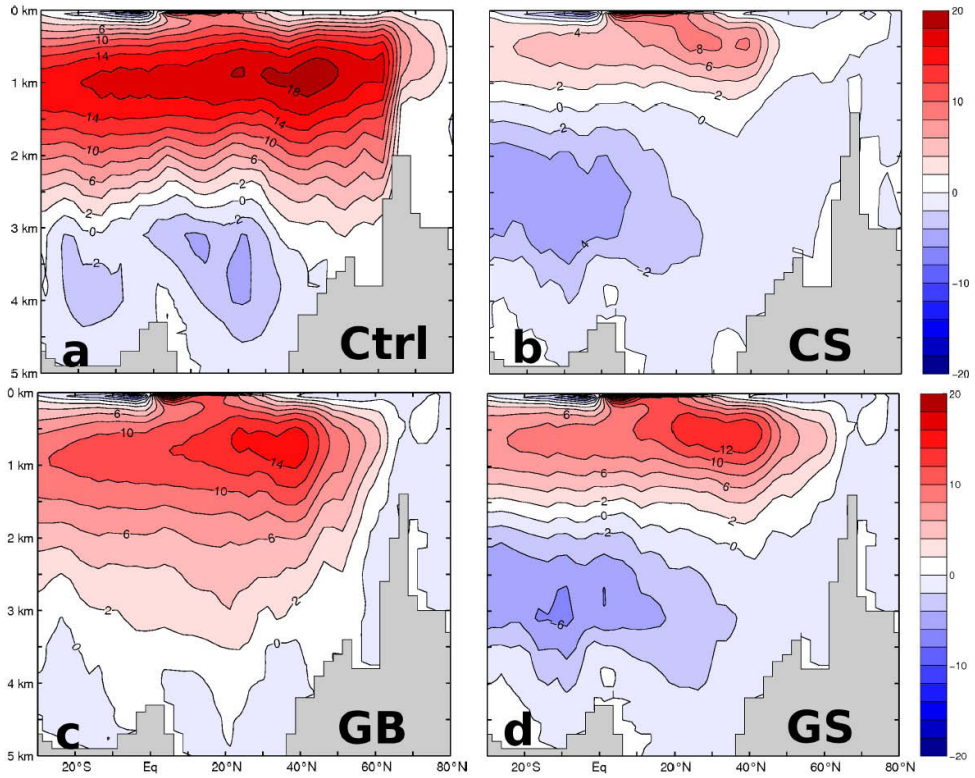

Figure 7.3: Meridional overturning circulation in the Atlantic Ocean (AMOC) for the control run (a) and LGM runs CS, GB, and GS (b to d, see Chapter 4 for a description). Numbers are volume transport rates in *Sv* (10^6 ms^{-1}).

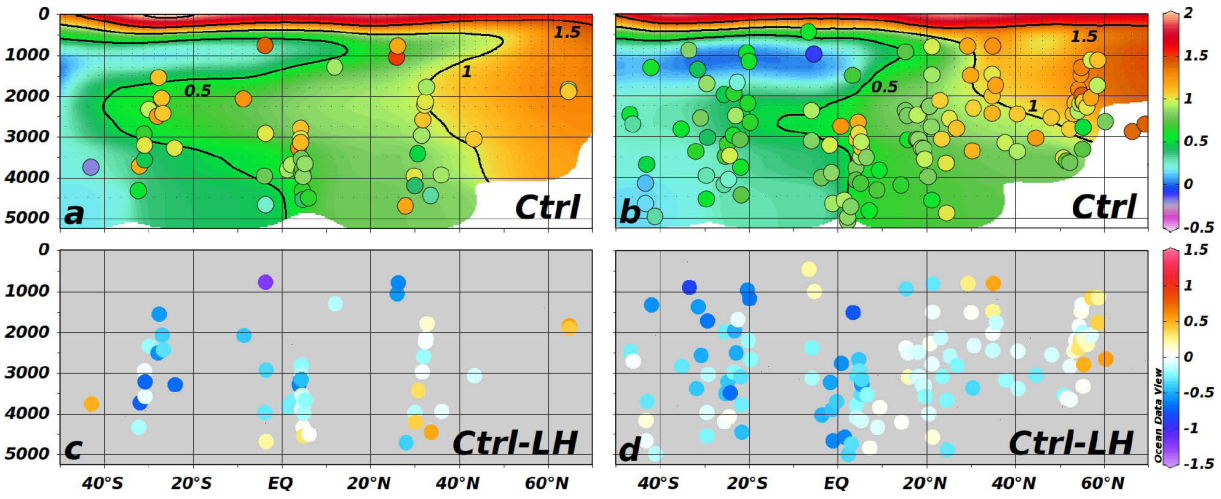

Figure 7.4: (a) Control run with Late Holocene $\delta^{13}C_{foram}$ data overlay for the West Atlantic, and (c) the difference between control run $\delta^{13}C$ and Late Holocene $\delta^{13}C_{foram}$. (b, d) like in (a, c), but along the East Atlantic section. Positive numbers in (c, d) indicate model $\delta^{13}C$ values that are higher than Late Holocene $\delta^{13}C_{foram}$ values.

dominates the western South Atlantic at a depth of 2.5 km, whereas in the eastern South Atlantic lower δ^{13}C water is more widespread.

The difference plots between control run and LH sediment values (Figures 7.4 and B.1) show that the control run yields lower δ^{13}C values than the sediment cores in most of the South Atlantic, but especially in the upper 2 km south of 20°S. There, the average difference is 0.52‰ VPDB. In the North Atlantic model values are both, lower and higher than the sediment core δ^{13}C. The difference, however, is small and rarely exceeds 0.2‰ VPDB.

7.2.2 LGM runs

Presented are the results of the AMOC for the three LGM runs. Scenario CS shows a shoaled and weakened AMOC (see Figure 7.3b) compared to the control run. Maximum positive overturning is about 8 Sv at a depth of 500 m and between 20-40°N. In contrast, southerly-sourced waters are more widespread south of the equator at depths between 2-3 km. Scenario GB is characterised by strong, basin-filling transport of northerly-sourced waters (Figure 7.3c), with its maximum positive overturning (14 Sv) between 500-1000 m and 20-40°N. Negative overturning is only observed near the ocean floor and is nowhere stronger than 2 Sv. Scenario GS, finally, yields a shoaled positive AMOC cell with a maximum strength of 12 Sv centred between 400-900 m and at 20-40°N. The upper 1.5 km of the ocean basin are in the positive AMOC regime. Negative overturning is slightly stronger (6 Sv) than for CS, and it extends further north. As already mentioned in Chapter 5, HAMOCC2s can also diagnose atmospheric CO_2. The associated CO_2 concentrations (in ppmV) are 273 (GB), 244 (GS) and 225 (CS). The reduction is mostly due to increased formation of proto-AABW. It is beyond the scope of the study, however, to discuss the CO_2 concentrations in more detail.

All LGM runs show a similar large-scale pattern in the distribution of $\delta^{13}C_{DIC}$: the surface ocean contains the highest values, and the deep South Atlantic contains the lowest. CS shows the strongest meridional and vertical gradient in δ^{13}C values in the Atlantic Ocean (Figure 7.5 and

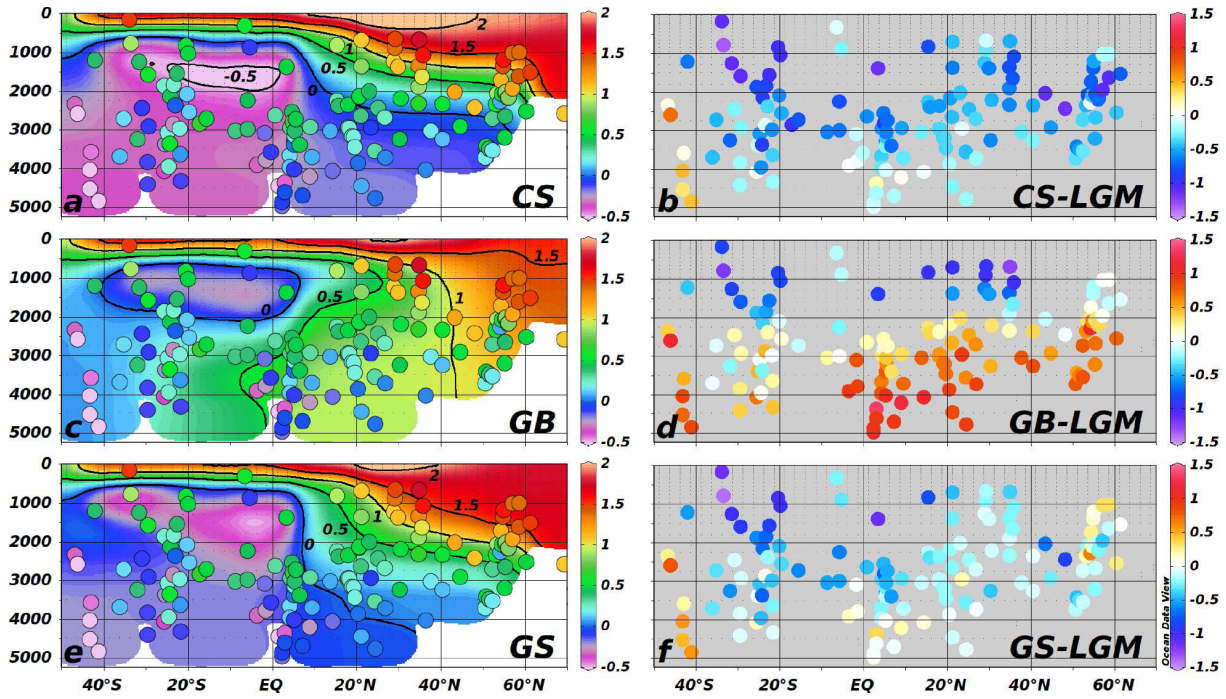

Figure 7.5: East Atlantic section: (a) CS δ^{13}C with LGM $\delta^{13}C_{foram}$ data overlay, and (b) model-data differences. In (b): Positive numbers indicate model δ^{13}C values that are higher than $\delta^{13}C_{foram}$ values. (c, d) and (e, f) like in (a, b), but for model runs GB and GS, respectively.

Figure 7.6). In GS the gradient is reduced slightly, whereas in GB the δ^{13}C gradient is similar to that of the control run. All LGM runs show a prominent water body at intermediate depths in the southern East Atlantic with very low δ^{13}C values (from -0.4‰ VPDB in GB to less than -0.5‰ VPDB in CS, see Figure 7.5). All runs also show a more or less pronounced tongue of low δ^{13}C water at depths of 750-1000 m in the western South Atlantic (Figure 7.6 and Figure B.3).

In CS high δ^{13}C values (greater than 1‰ VPDB) reach down to depths of 1.5 km in the eastern North Atlantic north of 40°N. For the western North Atlantic this high δ^{13}C body extends even further south to 20°N (Figure 7.6a). Conversely, low δ^{13}C (less than 0‰ VPDB) dominates the deep western South Atlantic below depths of 3 km reaching as far north as 50°N, whereas in the eastern Atlantic, south of 10°N low δ^{13}C fills the entire ocean basin below 1 km water depth (see Figure B.3a in Appendix B).

In GB the entire North Atlantic north of 40°N is dominated by high δ^{13}C, which extends

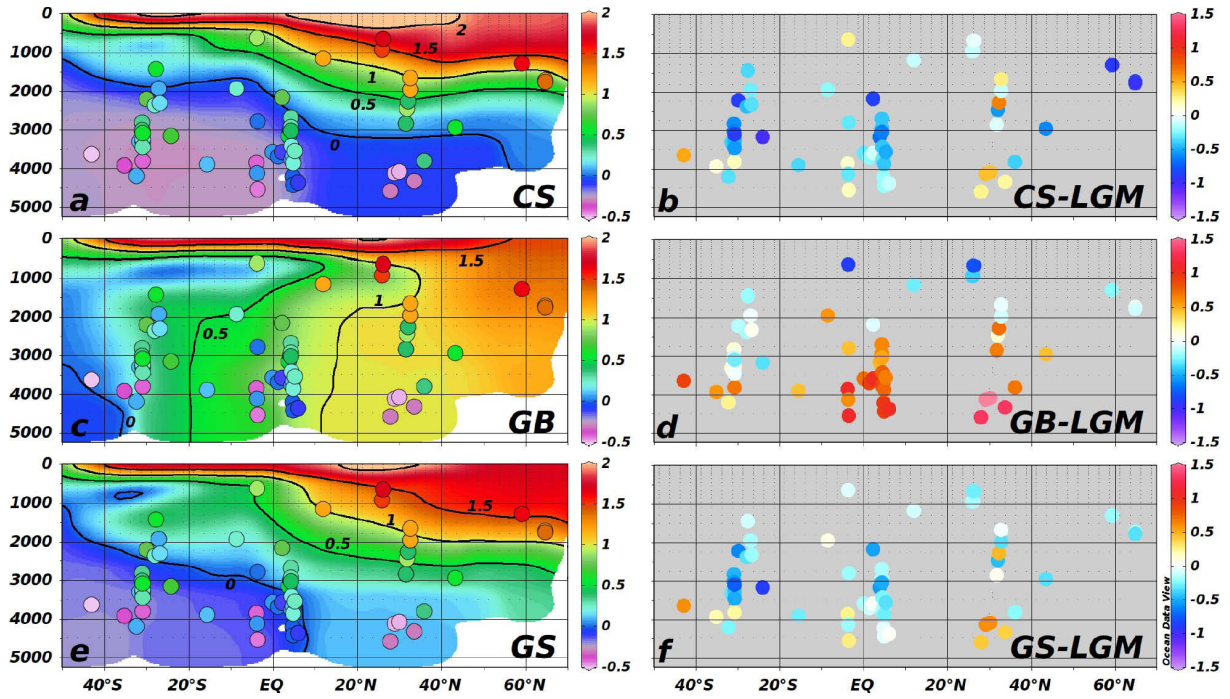

Figure 7.6: Like Figure 7.5, but along the West Atlantic section.

south to 15°N in the western North Atlantic. Values of δ^{13}C below 0‰ VPDB only exist in the western South Atlantic below 2 km water depth and south of 35-40°S, and in the intermediate eastern South Atlantic (Figure 7.5c).

GS shows δ^{13}C values higher than 1‰ VPDB in the North Atlantic in the upper 1.5 to 2 km extending south to 30°N in the eastern Atlantic, and to 10°N in the western Atlantic (cf. Figure 7.5e and Figure 7.6e). Low δ^{13}C values take up the western Atlantic below depths of 3 km reaching as far north as 8°N. Conversely, in the eastern Atlantic south of 8°N δ^{13}C is lower than 0‰ VPDB everywhere except for the upper 1 km of the water column.

The correlation coefficient r between δ^{13}C values of the three model runs and the glacial sediment core data is 0.72 for CS, 0.31 for GB, and 0.76 for GS. The RMS difference between model scenario and sediment data yields 0.70, 1.06 and 0.68‰ VPDB for CS, GB and GS, respectively. The Taylor diagram [Taylor, 2001] summarises the correlation coefficients and centred RMS differences for different areas of the Atlantic Ocean (Figure 7.7).

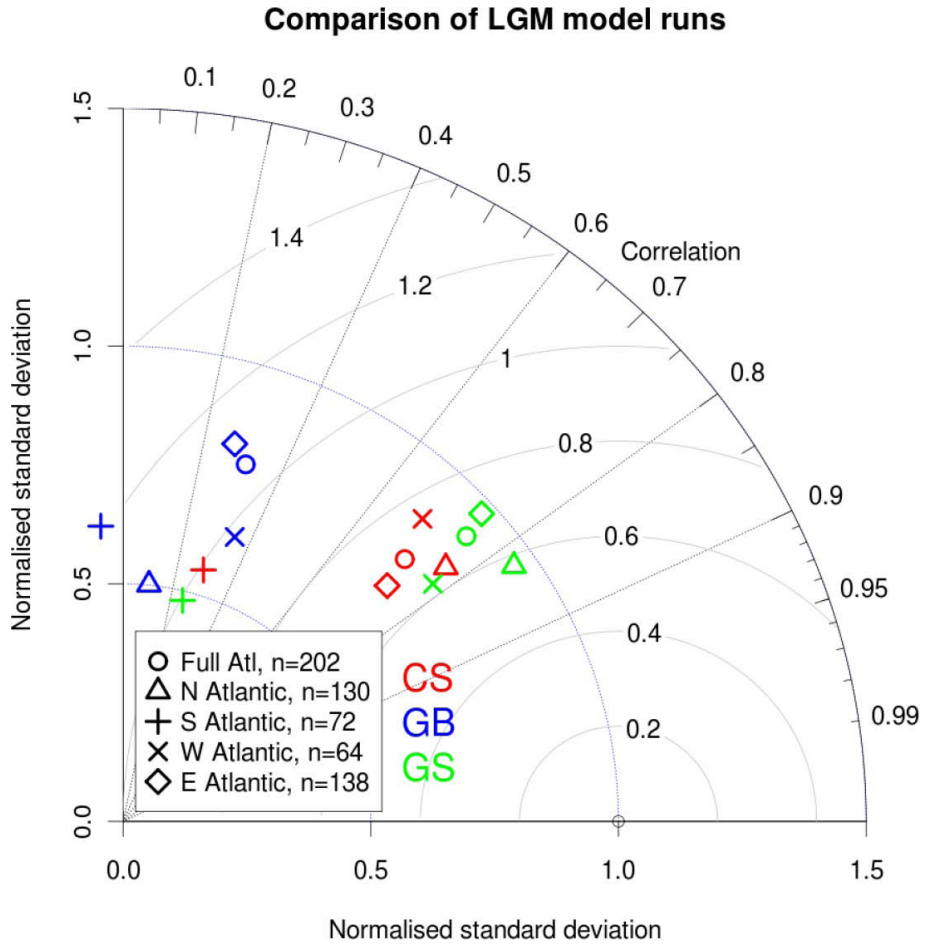

Figure 7.7: Taylor diagram [Taylor, 2001] showing the correlation coefficients (along the arc) and the centred RMS differences (gray solid arcs of circles) for the three LGM scenarios and different Atlantic regions when compared to the LGM $\delta^{13}C_{foram}$ data. The number of data points included in each sub-area is given by n. The normalised standard deviation is a measure for $\delta^{13}C$ variance in the model with respect to the observations.

In the North, West, and East Atlantic $\delta^{13}C_{GS}$ correlates strongest with the sediment data (r = 0.82, 0.78, and 0.73, respectively). In the South Atlantic r is lower than 0.30 for all model scenarios. The GB correlation coefficient is nowhere greater than 0.35.

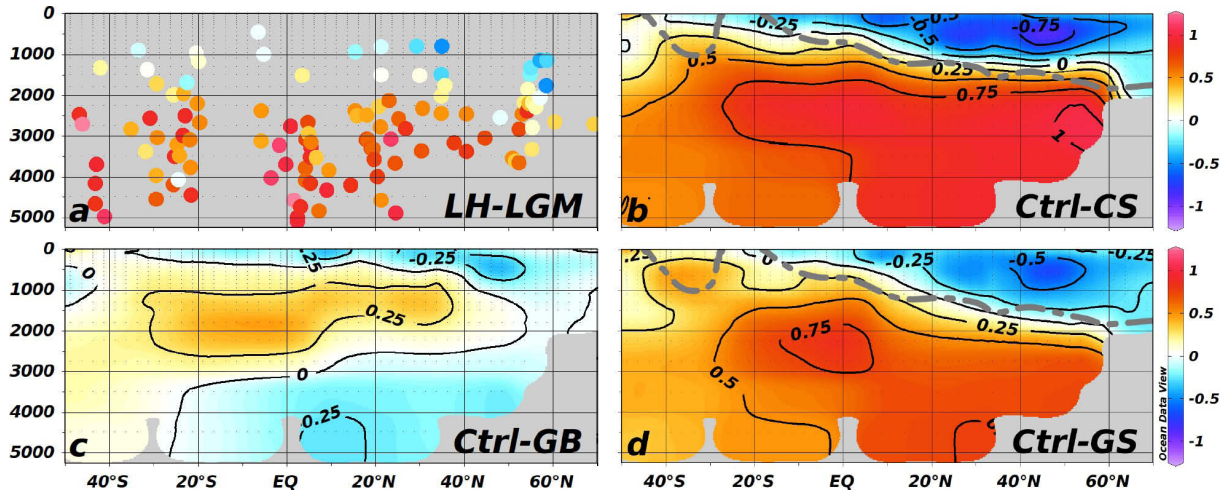

Figure 7.8: East Atlantic $\Delta\delta^{13}$C plots (anomalies): (a) difference between LH and LGM sediment data, (b to d) differences between control run and CS, GB, and GS, respectively. Sediment data indicate a strong $\Delta\delta^{13}$C gradient between the surface/intermediate ocean and the deep ocean. Gray dash-dotted lines in (b) and (d) are zero-lines which are based on observations (a).

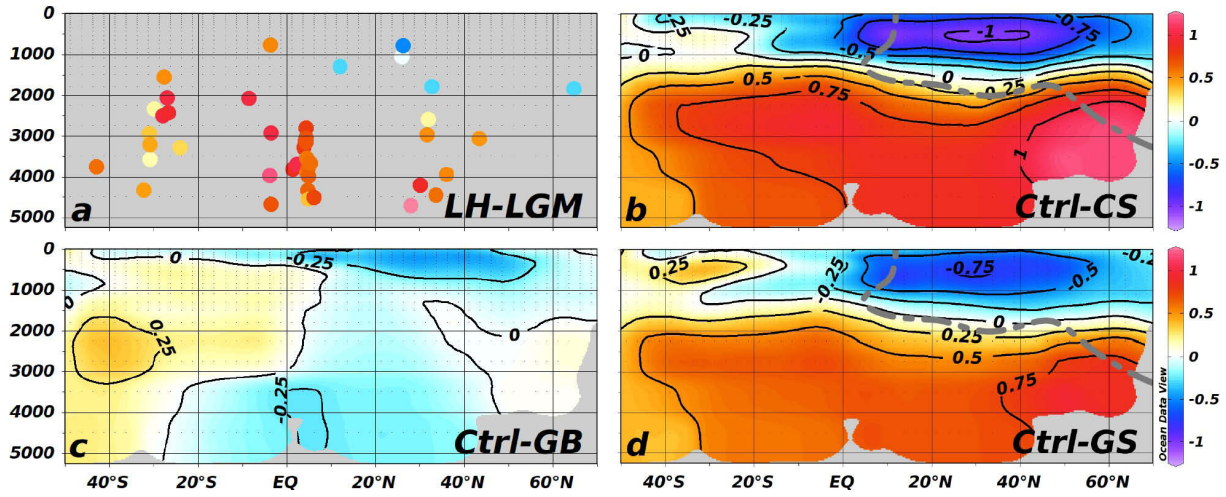

Figure 7.9: Like Figure 7.8, but along the West Atlantic section.

7.2.3 $\Delta\delta^{13}$C - differences between LH and LGM sediments, and differences between control run and LGM runs

The $\Delta\delta^{13}$C plot for the sediment data (Figure 7.8a) shows that the LH δ^{13}C data are more negative than the LGM data in the northern Atlantic at depths above 1.5 to 2 km, but are more positive in all areas below 2 km waterdepth. The δ^{13}C values in the top 2 km in the eastern South Atlantic are similar for the two time slices. The maximum positive anomaly for GB is in the central Atlantic Ocean between 40°N and 40°S and depths between 500 m and 2500 m (up to 0.5‰ VPDB). Negative anomalies (values of -0.3‰ VPDB) are present in the tropical and North Atlantic surface ocean as well as at depths below 3 km north of 20°S. CS anomalies are most negative in the upper 1250 m of the North Atlantic (-0.6‰ VPDB), but positive below 1500 m water depth. Positive anomalies are strongest in the deep North Atlantic (up to +1‰ VPDB), whereas they are weaker in the deep South Atlantic (+0.5‰ VPDB). Anomalies are zero south of 40°S at depths above 1.5 km. GS anomalies are similar in magnitude to CS anomalies, but less pronounced: negative anomalies in the North Atlantic above depths of 1500 m and in the tropical surface ocean, and positive anomalies in most of the remaining ocean basin. Maximum positive values are found in the deep North Atlantic and the mid-depth tropical Atlantic (+0.7‰ VPDB), lower ones in the deep South Atlantic (+0.4‰ VPDB).

7.3 Model-data comparison discussion

7.3.1 Control run

The control run captures the general δ^{13}C features observed in the water column of the present-day Atlantic and in LH sediment cores. Compared to GLODAP, control run δ^{13}C values are higher in the North Atlantic. This is most likely explained by the Suess effect, which has recently been shown to penetrate down to 2500 meters depth and southwards to 30°N in the North

Atlantic [Olsen and Ninnemann, 2010]. Two cores near the Bahamas by Slowey and Curry [1995], OCE205-33GGC and OCE205-100GGC, have higher δ^{13}C values than are seen in the control run. GLODAP $\delta^{13}C_{DIC}$ measurements, however, contradict such high $\delta^{13}C_{foram}$ values. The control run correlates very well with LH sediment data in the Northern Atlantic (see Figure 7.4), but underestimates the observations in some areas of the South Atlantic. Model δ^{13}C values in the upper 500-2000 meters in the South Atlantic are lower than foraminiferal δ^{13}C by more than 0.5‰ VPDB. This seems to be a general model problem, that is also present in the glacial model scenarios (see below).

An altered Redfield stoichiometry for Southern Ocean and Antarctic surface and intermediate depth waters (as suggested by Zahn and Keir [1994] or Lynch-Stieglitz et al. [1995]) could be the source for the lower-than-observed Antarctic Intermediate Water (AAIW) δ^{13}C in the model. Zahn and Keir [1994] argued that isotopically depleted $CO_{2(aq)}$ readily enters the atmosphere once the upwelled waters come into contact with the sea surface. At the same time nutrients are not taken up by photosynthesis to such a degree that would ensure a constant Redfield stoichiometry, which in turn would lead to higher-than-expected δ^{13}C values for AAIW.

Following Broecker and Maier-Reimer [1992] and Lynch-Stieglitz et al. [1995] we investigate the contribution of the air-sea exchange ($\delta^{13}C_{as}$) to the carbon isotopic composition of surface water by removing the biological component from the total modeled or observed δ^{13}C signal:

$$\delta^{13}C_{as} = \delta^{13}C - (2.7 - 1.1 \times PO_4),$$

where PO_4 is the phosphate concentration in μmol kg^{-1}. Our control run yields positive values of $\delta^{13}C_{as}$ in the AAIW formation area, which indicates that the isotopic signature of our modeled AAIW is substantially influenced by isotopic air-sea fluxes (Fig. B.4, Appendix B). However, our model values of $\delta^{13}C_{as}$ (about 0.2‰ VPDB) are significantly smaller than observations (of up to 1‰ VPDB according to Mackensen et al. [1996]) which suggests that our carbon cycle model

underestimates the isotopic air-sea exchange in the AAIW formation area. This is probably due to the air-sea exchange formulation in the model which does not explicitly depend on the wind speed, but employs a globally averaged gas transfer velocity value. This model deficit is also corroborated by the results from a numerical sensitivity study carried out by Broecker and Maier-Reimer [1992] who (employing an earlier version of our model) found that by doubling the air-sea exchange rate of CO_2 the $\delta^{13}C$ values in the formation region of AAIW would increase by 0.4‰ VPDB.

7.3.2 LGM runs

The model-data difference plots (Figure 7.5 and Figure 7.6) indicate that model results are systematically higher than observations in the deep South Atlantic and along the North American coast.

In the deep Southern Ocean south of 40°S GS simulates $\delta^{13}C$ values that are higher by 0.23 to 0.84‰ VPDB than a whole suite of sediment cores (PS1745-3 and PS2082-1 [Mackensen et al., 1994], TTN057-6 [Hodell et al., 2003], RC15-93, RC15-94, TN057-21 and V22-108 [Ninnemann and Charles, 2002], see Figure 7.5 and 7.6). The $\delta^{13}C$ values in the cores reported by Ninnemann and Charles [2002] are based on both *C. wuellerstorfi* and *C. mundulus*. Hodell et al. [2001] showed that *C. kullenbergi* (which is the same species as *C. mundulus* [Yu et al., 2008]) records systematically lower $\delta^{13}C$ values than *C. wuellerstorfi*. Extrapolating the $\delta^{13}C_{\text{kullenbergi}}$ data scatter to -0.80‰ VPDB suggests a $\delta^{13}C_{\text{wuellerstorfi}} \approx 0$‰ VPDB (see Hodell et al. [2001]'s figure 1). Some of the difference seen in the model-data comparison could therefore be taken up. Another possible influence is the phytodetritus effect [Mackensen et al., 1993], which causes foraminifera to record lower-than-expected $\delta^{13}C$ values, typically explaining 0.4‰. Cores that lie close to an oceanic front are potentially affected. The coarse model resolution does not permit to capture steep oceanographic gradients such as oceanic fronts, which may also partly explain the model-data offset in the Southern Ocean. LGM reconstructions of oceanic fronts

in the Southern Ocean by Gersonde et al. [2003, 2005] suggest that the Polar Front (PF), the Sub-Antarctic Front (SAF) and the Sub-tropical Front (STF) shifted northwards by 3-5°. Careful comparison of the frontal positions with the locations of the relevant cores shows that PS1745-3 and RC15-93 fall exactly on the reconstructed PF, whereas PS2082-1 and TTN57-6 coincide with the reconstructed SAF. Cores RC15-94 and V22-108 fall in between the reconstructed PF and SAF, TN057-21 lies between the reconstructed SAF and STF. Since oceanic fronts meander about their mean position, the latter cores may also be affected by the phytodetritus effect. Hence, both factors, measurements on epibenthic species other than *C. wuellerstorfi* and changes in frontal positions with the associated phytodetritus effect, may explain model-data differences in the deep Southern Ocean.

In the western North Atlantic below 4 km and between 20-30°N there are four cores which have δ^{13}C values that are lower than GS by 0.40 to 0.62‰ VPDB (KNR140-12JPC, KNR140-22JPC and KNR140-28GGC [Keigwin, 2004], EN120-1GGC [Boyle and Keigwin, 1987], see Figure 7.6). The horizontal flow fields of model runs CS and GS (not shown) reveal an AABW influx in the deep western North Atlantic. The model δ^{13}C signal, however, is still too high. Keigwin [2004] stresses that measurements of Holocene δ^{13}C values in this location below 3 km do not agree with present-day DIC measurements, which may point towards yet unknown problems with these cores.

There are also areas where model results indicate lower δ^{13}C values than observational δ^{13}C values. This is particularly true for the intermediate depth South East Atlantic, the Brazil margin cores, the central North Atlantic (see Figure B.2, Appendix B), and the central South Atlantic at 3 km water depth.

In the South East Atlantic all model scenarios (including the control run) yield lower δ^{13}C values by about -1‰ VPDB compared to the sediment data (175-1087A [Pierre et al., 2001], 175-1085A (given as ODP1085A in Bickert and Mackensen [2004]), IOW226920-3 [Mollenhauer et al., 2002], and KW-31 [Sarnthein et al., 1994]). Sediment $\delta^{13}C_{foram}$ data are consis-

tently higher than any model simulation δ^{13}C, and model results of temperature and salinity (not shown) do not point towards any anomalous water mass here. The low model δ^{13}C is likely to be an artefact which may partly be caused by underestimation of carbon isotope air-sea exchange in the formation region of AAIW (see control run discussion above). For the LGM scenarios this misrepresentation might be exacerbated due to generally stronger and seasonally more varying glacial winds, which may cause the anomalously low δ^{13}C signal in the South East Atlantic. One might also speculate about a Mediterranean influence: Zahn et al. [1987] find that Mediterranean Outflow Water (MOW) has a δ^{13}C signature that was higher during the LGM (greater than 1.6‰ VPDB) when compared to today (1.3‰ VPDB). Bickert and Mackensen [2004] show that MOW extends southwards after leaving the Strait of Gibraltar. It cannot be verified, however, that MOW extends further south than 10°N at depths above 2500 meters, as there are no sediment cores at these depths away from the continental slope. Moreover, the difference in MOW δ^{13}C between today and the LGM is small (0.3‰ VPDB) compared to the difference seen in the model-data comparison in the mid-depth South East Atlantic (1‰ VPDB). There is no Mediterranean in our LGM set-up.

Most of the Brazil margin cores of Curry and Oppo [2005] between 25-35°S contain δ^{13}C values that are higher by up to 0.60‰ than model values in GS (e.g. CHN115-70PC, CHN115-89PC, or CHN115-91PC, see Figure 7.6f). The same data-model difference holds for the LH data and our control simulation (Figure 7.3c). The most likely culprit is again poor carbon isotope air-sea exchange in the model (see control run discussion above), which is likely to be more pronounced in our LGM runs. Additionally, upwelling of NADW-derived waters south of Cape Frio would introduce much higher δ^{13}C values [Acha et al., 2004], but the model cannot resolve such local upwelling features.

Several cores in the central North Atlantic between 25-40°W and at 2-3.5 km water depth are enriched in ^{13}C with respect to either GS or CS (e.g. CHN824115 [Boyle and Keigwin, 1987], or T86-15P [Sarnthein et al., 1994]) with δ^{13}C values relative to GS that are higher by 0.42 to

0.66‰ VPDB (see Figure B.2 in Appendix B). This points towards a model NADW flowpath that is too shallow in the central North Atlantic.

Analogously, there are four cores in the central South Atlantic by Bickert and Mackensen [2004] for which scenario GS simulates δ^{13}C values that are lower than observations by 0.58 to 0.88‰ VPDB (GeoB3808-6, GeoB5115-2, GeoB5121-2, and GeoB2016-1). Again, one may speculate about a NADW signal in the sediments that neither model scenario captures as model-NADW is shoaling too much. Additionally, the model problems seen in the South East Atlantic may contribute by extending into the central South Atlantic.

7.3.3 $\Delta\delta^{13}$C - differences between LH and LGM sediments, and differences between control run and LGM runs

The $\Delta\delta^{13}$C plots in Figure 7.8 and 7.9 have the advantage that systematic errors such as constant offsets in δ^{13}C values in the sediments due to, e.g. upwelling, or model artefacts such as the one seen in the South East Atlantic, are reduced. Scenario GB performs poorly when compared to the sediment data (Figure 7.8a, c and 7.9a, c). $\Delta\delta^{13}$C is similar in both CS and GS. For the sediments the $\Delta\delta^{13}$C = 0 line lies close to 2 km water depth. The same holds for GS, but not for CS, where the zero-line is above 1.4 km water depth (Figure 7.8b and 7.9b). In addition, the average sediment $\Delta\delta^{13}$C signal below 2 km water depth is less than 0.75‰ VPDB, which is similar to GS. In CS this value is mostly above 0.75‰ VPDB. This further strengthens the good agreement of scenario GS with the observations. The sediment cores south of 40°S are only affected by frontal upwelling during the LGM and not during the LH (see above). Therefore, the effect is not systematic, and the high $\Delta\delta^{13}$C in the sediments comes as no surprise.

The differences between our three model scenarios are summarised in Figure 7.7. Scenarios GS and CS both correlate very well with the sediment data. GS, however, correlates better in the North, West and East Atlantic. Additionally, the variance in GS is closer to that of the

reconstructions. Scenario GB performs poorly in the model-data comparison.

The altered fresh water balance in the Southern Ocean which is employed in both, GS and CS, seems to be a crucial feature in our LGM simulations. It is caused by (1) enhanced northward sea ice export and melting away from the sea ice production zone, which in turn causes (2) a relative increase in brine rejection when new sea ice is forming. The overturning cell in the North Atlantic is shoaling and weakening for both scenarios, indicating another important LGM feature (Figure 7.3). The strength of the positive overturning cell, however, is less well constrained: 12 Sv for GS contrast with only 8 Sv for CS, although both scenarios show a good fit for the North Atlantic. This significant difference in the response of the model to the two different SST reconstructions deserves further explanation. It is important to note that the SST reconstructions have an impact on atmospheric wind patterns and evaporation/precipitation patterns that the atmospheric model generates, which in turn have an impact on freshwater and heat fluxes into the ocean, ocean circulation, and air-sea gas exchange (see also Romanova et al. [2004]). Scenario GS, for instance, has surface waters south of Iceland that are saltier by more than 2 PSU when compared to CS (not shown). This causes stronger downwelling and is very likely the reason for the more rigorous AMOC in scenario GS compared to CS. Since δ^{13}C is not a purely kinematical tracer, it can only be used to reconstruct the geometries of water masses. The strength of the overturning cell cannot be assessed.

7.3.4 Relation to previous studies

Previous model-data comparisons have either used a much reduced number of observations, or not employed a three-dimensional OGCM. Winguth et al. [1999] used ad-hoc circulation fields and a limited amount of mostly East Atlantic observations. Their glacial first guess scenario yields a reduced North Atlantic overturning circulation, which is compensated for by an increased influx of Southern Ocean deep waters. This result is similar to what we find for scenario GS, but there are conceptual differences. Winguth et al. [1999] prescribed estimated salinity

fields which were additionally modified in high latitudes to reduce the model-data misfit. In our model setup, salinity is a fully prognostic variable, which is physically more consistent.

Tagliabue et al. [2009] employ an OGCM and a biogeochemistry model forced by different LGM boundary conditions. Their model scenario that agrees best with observations (CircA) has a reduced ventilation in the North Atlantic and reduced AABW export. Their increased AABW export scenario (CircB) does not agree well with observations. This is the opposite of what our δ^{13}C model results show: our two best fitting scenarios arrive at increased AABW export from the Southern Ocean. Since increased AABW inflow into the North Atlantic is also supported by radiocarbon, grain size, and ^{231}Pa/^{230}Th studies [Robinson et al., 2005; Hall et al., 2011; Negre et al., 2010] we believe that our GS and CS model scenarios are well suited to describe the LGM Atlantic Ocean state.

So far most modeling studies have focused on changing the freshwater balance in the North Atlantic [Roche et al., 2007; Kageyama et al., 2009; Otto-Bliesner and Brady, 2010], with mixed successes regarding the integrity with observational data. Changes in freshwater production in the Southern Ocean [Adkins et al., 2002] have attracted comparatively less attention, but seem to be important [Stocker et al., 1992; Fichefet et al., 1994; Winguth et al., 1999; Seidov et al., 2001; Shin et al., 2003b; Schmittner, 2003; Butzin et al., 2005]. Schmittner [2003] increased rates of sea ice formation and northward export while keeping the AMOC strength at present-day levels. This resulted in saltier and denser AABW, increased its formation rate, and led to a higher consistency with reconstructions of glacial bottom water properties. Shin et al. [2003a] modeled enhanced northward sea ice export in the Southern Ocean in a fully coupled ocean-atmosphere circulation model and arrived at a shoaled and weakened AMOC. Butzin et al. [2005] found that modeling radiocarbon in the glacial ocean with a changed freshwater balance in the Southern Ocean agrees best with observations. Our study with its widespread collection of δ^{13}C values puts these modeling efforts on a more comprehensive observational base and further highlights the Southern Ocean's role in influencing global glacial climate.

7.4 Model-data comparison conclusions

The objective of this study is to test in numerical sensitivity experiments which AMOC scenario could be reconciled with observed modern and past δ^{13}C distributions in the Atlantic Ocean, and to infer the climatic conditions and processes acting in the Atlantic Ocean during the LGM. We have assembled a δ^{13}C dataset of 220 sediment cores that we compare to three different LGM model scenarios.

The model scenario that best correlates with observations (r = 0.76) has a shoaled positive overturning circulation in the North Atlantic that is reduced by 40% compared to the present-day. Northward AABW flux is intensified. This scenario (GS) is based on GLAMAP SSTs and employs an altered freshwater balance in the Southern Ocean that mimics increased sea ice export and melting at latitudes between 50-55°S, north of the sea ice production zone.

GS correlates best in the northern (r = 0.82), western (0.78) and eastern Atlantic (0.73), with a δ^{13}C variance that is close to the observed $\delta^{13}C_{foram}$ variance. Scenario CS, which is forced by CLIMAP SSTs, also uses an altered freshwater balance in the Southern Ocean, and has a weak AMOC. It performs slightly worse than GS in all Atlantic sub-areas, and also with regard to the variance. Our glacial base scenario GB with its strong AMOC similar to the present-day does not agree with observations.

Some differences between model and sediment data δ^{13}C values can be explained by local effects (e.g. upwelling) and known model deficiencies. In particular, the poor representation of carbon isotope air-sea exchange in the AAIW formation region due to globally averaged wind fields in the carbon cycle model causes lower-than-observed δ^{13}C model values. An implementation of seasonally varying wind patterns in the carbon cycle model as well as higher model resolution in critical areas such as near oceanic fronts is therefore desirable.

Our results further corroborate that the AMOC cell shoaled to less than 2000 meters water depth during glacial times. By how much the positive AMOC strength weakened cannot be es-

tablished, because different boundary conditions and overturning strengths, as found in GS and CS, yield similar results for δ^{13}C. GS with its more recent GLAMAP reconstruction shows an AMOC weakening to 12 Sv, which is a reduction by 40% compared to its present-day strength. The increased negative AMOC at depth in scenarios GS and CS is in line with and further supports recent ^{231}Pa/^{230}Th and grain size studies [Negre et al., 2010; Hall et al., 2011]. Our findings further underline that the Southern Ocean's fresh water balance might play a key role in explaining the glacial ocean.

Chapter 8

Modelling δ^{13}C in benthic foraminifera: insights from model sensitivity experiments

This chapter presents a study that assesses the impact of different physical, biological and carbonate chemistry processes on benthic $\delta^{13}C_{foram}$ values by performing model sensitivity experiments. We highlight some of the uncertainties in $\delta^{13}C_{foram}$ values and put some upper limits on their extent. For that we employ an adapted version of the foraminifera calcification model developed by Wolf-Gladrow et al. [1999] and Zeebe et al. [1999]. The model and its adaptation to benthic foraminifera is described in detail in Chapter 5.

8.1 Methodological approach

8.1.1 Model input parameters

First, we performed sensitivity simulations for different external bulk parameters. These parameters are $\delta^{13}C_{DIC}$, temperature, salinity, pressure, $\delta^{13}C_{POC}$, pH, and TA. Second, we varied parameters related to the foraminifer, i.e. respiration rate and calcification rate. When varying one

parameter all other parameters where kept constant at generic deep-sea values (see Table 8.1).

There are only few measurements of vital rates in benthic foraminifera. We chose our standard respiration rate of 0.41 nmol CO_2 h^{-1} based on laboratory measurements by Nomaki et al. [2007] on *C. wuellerstorfi*, taken from a depth of 1430 m. This respiration rate lies at the upper end of rates measured for benthic foraminiferal species [Hannah et al., 1994; Nomaki et al., 2007; Geslin et al., 2011], but is one of the few measurements on deep-sea species. Our standard calcification rate of 0.28 nmol C h^{-1} is based on in-culture measurements by Glas et al. [2012] on *Ammonia sp.* (Brünnich 1772), a shallow-water symbiont-barren benthic species. To our knowledge this represents the only calcification rate measurement on benthic foraminifera.

Parameter	**Units**	**Value**
Temperature	°C	1.3
Salinity		34.7
Pressure	bar	300
pH		7.9
$\delta^{13}C_{DIC}$	‰	0.5
$\delta^{13}C_{POC}$	‰	-21.9
Total Alkalinity (TA)	μmol kg^{-1}	2400
Radius	μm	200
Surface area	μm^2	5.03×10^5
Volume	μm^3	3.35×10^7
Biovolume$^{\alpha}$	μm^3	2.51×10^7
Biomass$^{\beta}$	μg C	2.51
Respiration Rate (RR)	nmol CO_2 h^{-1}	0.41
RR per biovolume	nmol CO_2 h^{-1} μm^{-3}	1.63×10^{-8}
RR per biomass	nmol CO_2 h^{-1} (μg C)$^{-1}$	0.16
Calcification Rate (CR)$^{\gamma}$	nmol CO_3^{2-} h^{-1}	0.28
CR per surface area	nmol CO_3^{2-} h^{-1} μm^{-2}	5.57×10^{-7}

$^{\alpha}$ Volume-to-biovolume conversion factor of 0.75 based on Hannah et al. [1994] and Geslin et al. [2011].
$^{\beta}$ Biovolume-to-biomass conversion factor of 10^{-7} (μg C) μm^{-3}, based on average of Turley et al. [1986] and Michaels et al. [1995].
$^{\gamma}$ Also applies to uptake of HCO_3^-.

Table 8.1: Standard model parameters used in this study.

8.1.2 Combined scenarios: the glacial, phytodetritus layer

The scenarios considered in this study are a control scenario for a generic deep ocean setting, a glacial scenario and a phytodetritus layer environment scenario. The changes in the different model parameters associated with the scenarios are shown in Table 8.2. Changes in $\delta^{13}C_{DIC}$ are not considered, since the model faithfully records those changes in the shell's final $\delta^{13}C_{foram}$ (see Section 8.2.1). Here we focus on the remaining parameters, which are less well studied.

For our glacial scenario we changed three parameters: temperature from 1.3°C to -1.95°C [Clark et al., 2009], pH from 7.9 to 8.0 [Hönisch et al., 2008], and $\delta^{13}C_{POC}$ from $-21.9‰$ to $-26.9‰$. The lowering of $\delta^{13}C_{POC}$ by 5‰ is based on changes in SSTs for the LGM from the MARGO dataset [Waelbroeck et al., 2009] combined with our own estimates of the associated changes in $\delta^{13}C_{POC}$ [Rau et al., 1989; Goericke and Fry, 1994].

Unfortunately, not much is known about phytodetritus layers on the sea floor. The most extensive review by Beaulieu [2002] has only limited information on chemical composition of these layers. Beaulieu [2002] cites a few measurements of $\delta^{13}C_{POC}$ ranging from $-24‰$ in the Atlantic sector of the Southern Ocean to $-31‰$ in the Mediterranean Sea. Furthermore, she reviews the availability of measurements on organic material, C:N ratios and inorganic content. But none is available in as much detail as would be needed for our model input. Therefore our phytodetritus scenario is based on best guesses for pH: as remineralisation and biodegradation happen, more CO_2 is released in and around the phytodetritus layer, lowering pH (here we reduce pH by 0.1 to 7.8). For the chosen respiration rate there is, again, not much quantitative information available, rather it has been observed that benthic foraminifera feed on phytodetrital layers and then start new chamber formation or reproduction [Gooday et al., 1990], all of which increase respiration. We therefore increase the respiration rate by 1 nmol CO_2 h^{-1} to 1.41 nmol CO_2 h^{-1}.

Parameter	Units	Standard	Glacial	Phytodet.
Temperature	°C	1.3	−1.95	1.3
pH		7.9	8.0	7.8
$\delta^{13}C_{POC}$	‰	−21.9	−26.9	−21.9
Resp. rate	nmol CO_2 h^{-1}	0.41	0.41	1.41

Table 8.2: Model parameters used in the different scenarios.

8.2 Sensitivity experiment results

Our results are presented in three subsections - one for environmental parameters, one for vital parameters and one for the combined scenarios. If not stated otherwise, the standard model parameters shown in Table 8.1 apply. Figures in this section show both CO_3^{2-} and HCO_3^- uptake. The final $\delta^{13}C_{foram}$ for CO_3^{2-} uptake is generally higher by 0.07 to 0.08‰ compared to HCO_3^- uptake, except for the vital effect sensitivities (see Section 8.3.3 below). If not mentioned otherwise, the description of the results refers to CO_3^{2-} uptake. Table 8.3 gives an overview of the different sensitivities found in this study.

8.2.1 Environmental parameters

Changes in $\delta^{13}C_{DIC}$ result in changes of exactly the same magnitude in $\delta^{13}C_{foram}$. There is, however, an offset of around 0.24‰ below the 1:1 line at standard model parameters (see Figure 8.1). Increases in temperature by 1°C cause an increase in $\delta^{13}C_{foram}$ of 0.05‰. The effect of salinity on $\delta^{13}C_{foram}$ is 0.01‰ for $\Delta S = 5$. Increasing pressure leads to a drop of $\delta^{13}C_{foram}$ by 0.02 to 0.03‰ per 100 bar (equivalent to 1 km water depth).

Increasing $\delta^{13}C_{POC}$ by 10‰ leads to an enrichment of $\delta^{13}C_{foram}$ by 0.06‰ (Figure 8.2). Generally there is a drop in $\delta^{13}C_{foram}$ when pH increases. At low pH values this drop is strongest at −0.08‰ per 0.1 pH increase before dropping to an average of −0.02‰ per 0.1 pH increase at pH values greater than 8.2. Changes in TA have a small impact of +0.01‰ on $\delta^{13}C_{foram}$ for an increase by 100 μmol kg^{-1}.

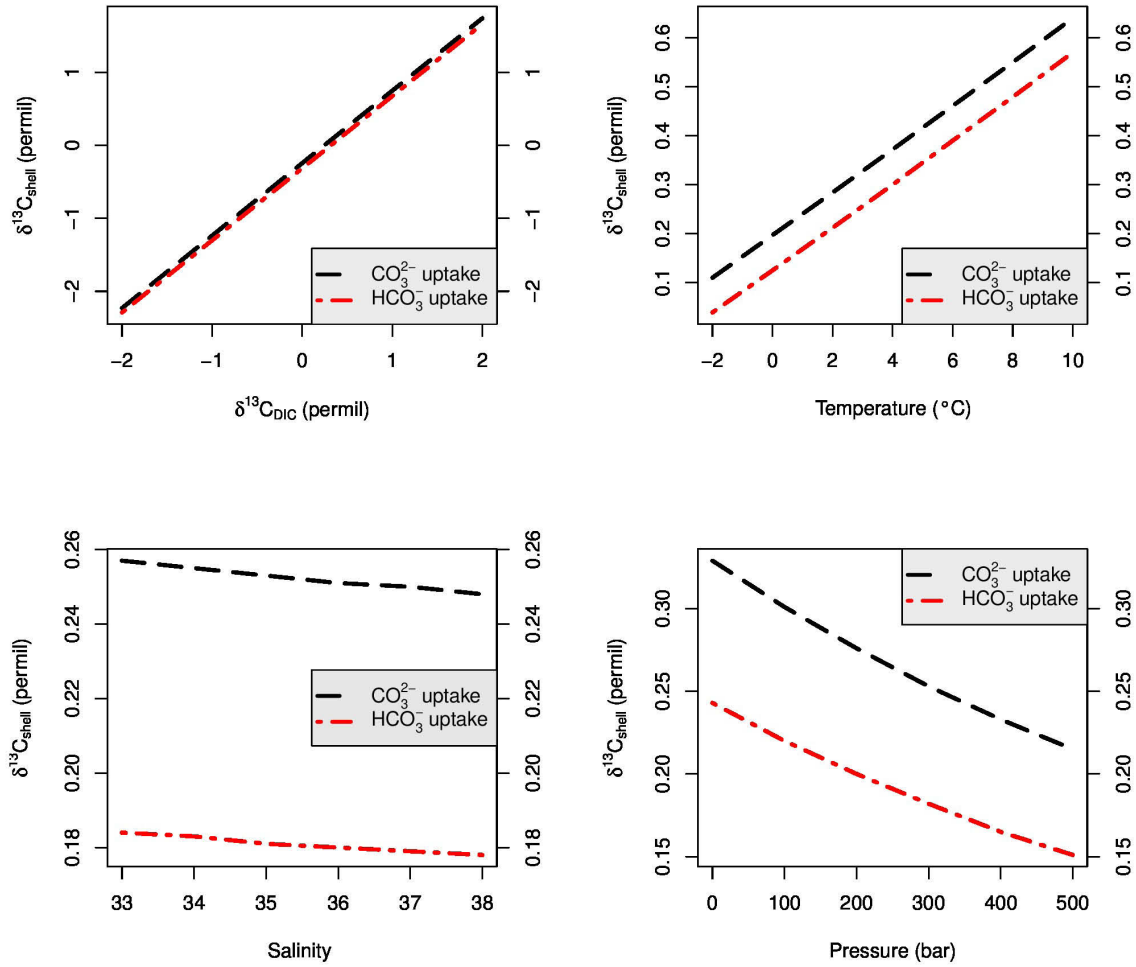

Figure 8.1: Foraminiferal $\delta^{13}C_{shell}$ shown for different external model parameters: $\delta^{13}C_{DIC}$, temperature, salinity and pressure.

8.2.2 Vital parameters

Increasing respiration rates result in more depleted $\delta^{13}C_{foram}$. The effect is strongest at low respiration rates where an increase by 1 nmol CO_2 h^{-1} causes a decrease of 0.36‰ compared to only 0.28‰ at higher rates (Figure 8.3). The fact that respiration rates higher than 2.5 nmol CO_2 h^{-1} are not possible for uptake of CO_3^{2-} will be discussed in Section 8.3.3 below.

For increasing calcification rates $\delta^{13}C_{foram}$ becomes more enriched. In the case of CO_3^{2-}

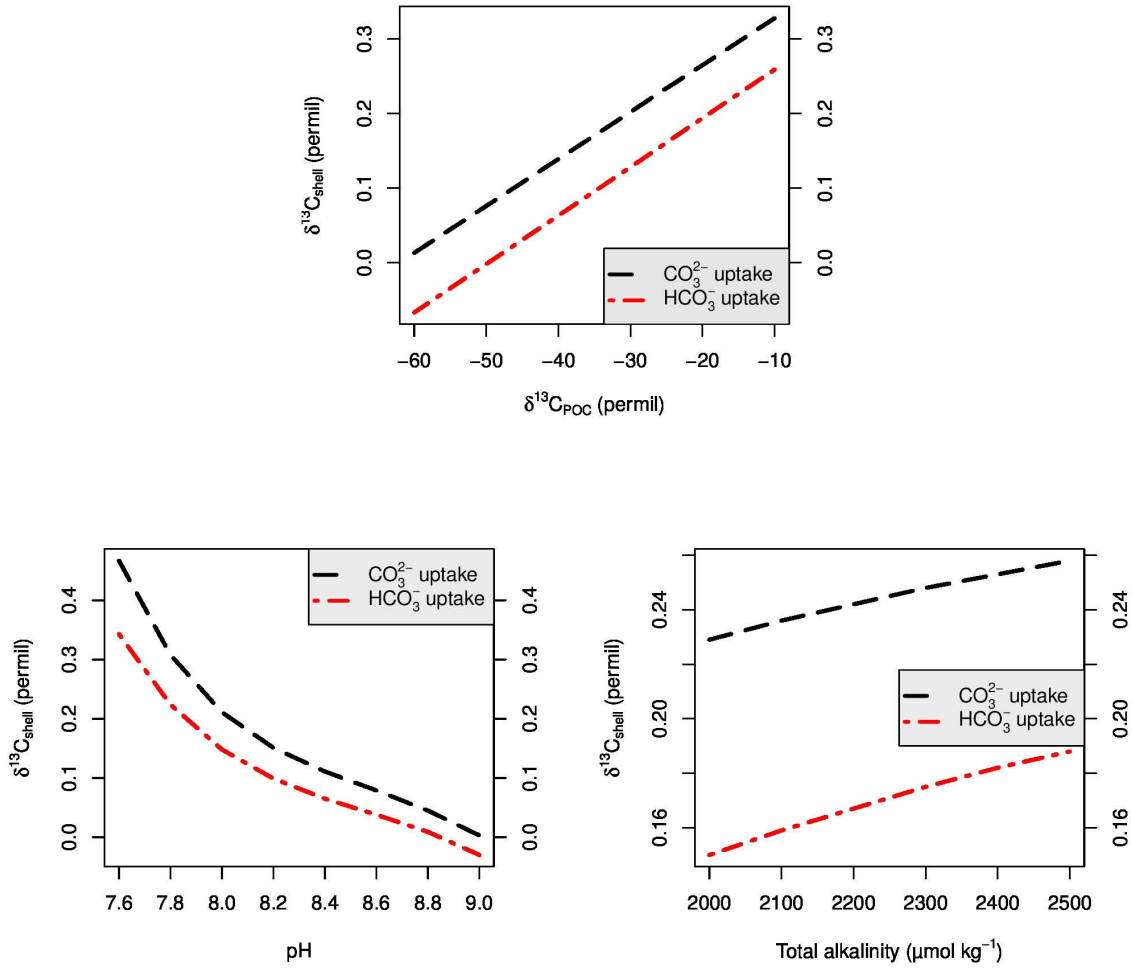

Figure 8.2: Same as in Figure 8.1 but for $\delta^{13}C_{POC}$, pH and TA.

uptake the enrichment is +0.08‰ per nmol CO_3^{2-} h^{-1} at low calcification rates and +0.27‰ per nmol CO_3^{2-} h^{-1} at rates of 0.5 to 0.6 nmol CO_3^{2-} h^{-1}. For HCO_3^- uptake the enrichment is linear at 0.01‰ per nmol HCO_3^- h^{-1}. Again, CO_3^{2-} uptake is limited: calcification rates higher than 0.6 nmol CO_3^{2-} h^{-1} are not possible in the model. This will be further discussed in Section 8.3 below.

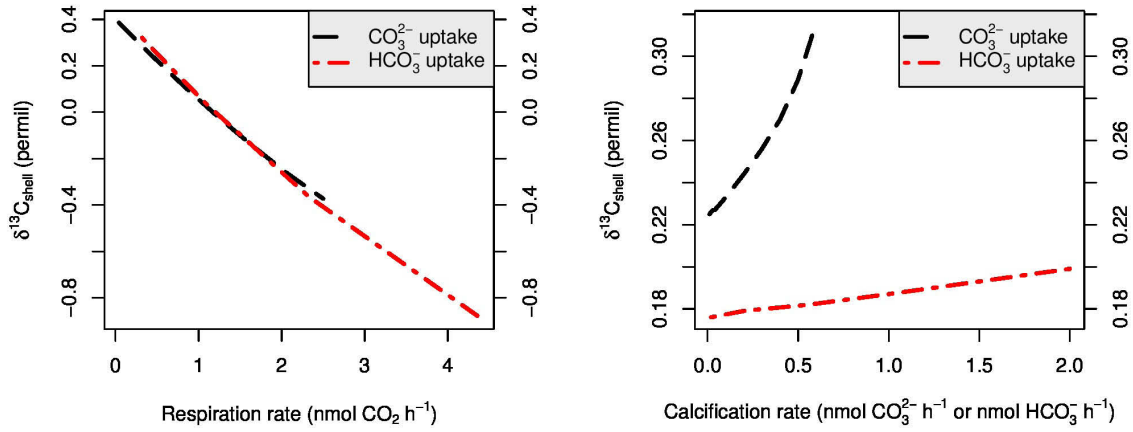

Figure 8.3: Foraminiferal $\delta^{13}C_{shell}$ shown for changes of vital parameters: respiration rate (left) and calcification rate (right).

Effect of ...	**given change of ...**	**on $\delta^{13}C_{foram}$**	**Figure**
$\delta^{13}C_{DIC}$	+1‰	+1.0‰	8.1
Temperature	+1°C	+0.05‰	8.1
Salinity	+5	< -0.01‰	8.1
Pressure	+100 bar	$\left\{ \begin{array}{c} -0.03‰ \text{ at lower pressure} \\ -0.02‰ \text{ at higher pressure} \end{array} \right\}$	8.1
$\delta^{13}C_{POC}$	+10‰	+0.06‰	8.2
pH	+0.1	$\left\{ \begin{array}{c} -0.08‰ \text{ at lower pH} \\ -0.02‰ \text{ at higher pH} \end{array} \right\}$	8.2
TA	+100 μmol kg^{-1}	+0.01‰	8.2
Resp. rate	+1 nmol CO_2 h^{-1}	$\left\{ \begin{array}{c} -0.36‰ \text{ at lower rates} \\ -0.28‰ \text{ at higher rates} \end{array} \right\}$	8.3
Calc. rate	+1 nmol CO_3^{2-} h^{-1}	$\left\{ \begin{array}{c} +0.08‰ \text{ at lower rates} \\ +0.27‰ \text{ at higher rates} \end{array} \right\}$	8.3
Calc. rate	+1 nmol HCO_3^- h^{-1}	+0.01‰	8.3

Table 8.3: Overview of $\delta^{13}C_{foram}$ sensitivity to different model parameters.

8.2.3 Combined scenarios

The combined effects of the two scenarios (glacial and phytodetritus layer) on the $\delta^{13}C_{foram}$ values are summarised in Table 8.4. The combined effects of the individual parameters are -0.22‰ and -0.23‰ for the glacial and the phytodetritus scenario, respectively.

Effect of ...	**given change of ...**	**on $\delta^{13}C_{foram}$**
Glacial combined		**-0.22‰**
Temperature	-3.25°C	-0.16‰
pH	+0.1	-0.04‰
$\delta^{13}C_{POC}$	-5‰	-0.03‰
Phytodetritus combined		**-0.23‰**
pH	-0.1	+0.05‰
Respiration rate	+1 nmol CO_2 h^{-1}	-0.30‰

Table 8.4: Overview of $\delta^{13}C_{foram}$ sensitivity for the two scenarios: glacial and phytodetritus. The combined impact on $\delta^{13}C_{foram}$ may differ from the sum of individual parameter impacts.

8.3 Sensitivity experiment discussion

8.3.1 General remarks

Many of the laboratory studies, that we are using to compare our model results with, have been conducted on planktonic foraminifera, which are easier to keep in culture and therefore more attractive experimentation objects. Of course, there are differences between planktonic and benthic foraminiferal species. Erez [2003] predicts that respiration and calcification rates of deep-sea benthics are one to two orders of magnitude lower than in planktonics. Benthics have much longer life cycles, being able to survive for several years [Hemleben and Kitazato, 1995]. In contrast, the lifetime of planktonics is typically of the order of weeks to months, with many life cycles tuned to the lunar cycle (e.g. Bijma et al. [1990, 1994]). Deep-sea benthics, especially those palaeoceanographers are interested in, are much smaller than planktonics. Their feeding habits and reproduction cycles are different. Wherever possible, we are using experimental studies on benthics for comparison. Where this is not possible we are taking planktonics bearing in mind the issues mentioned.

One drawback of the model is that it does not include any cell-internal biological features (e.g. internal vacuoles). Neither does it include processes such as vesicular transport inside the cell. Accordingly, changes in internal parameters such as the increase in pH of internal vesicles

as they are transported to the site of active calcification (e.g. de Nooijer et al. [2009]) cannot be accounted for. These deficiencies obviously limit the model's predictive power, but we leave the inclusion of internal cell processes to future studies. Nonetheless, our approach yields some very useful insights into shell-external parameters and the more straightforward vital effects.

8.3.2 Environmental parameters

In the following subsections we are discussing the various sensitivities in more detail. Salinity and TA are left out, since neither shows a marked effect on $\delta^{13}C_{foram}$.

$\delta^{13}C_{DIC}$

As expected, $\delta^{13}C_{DIC}$ affects $\delta^{13}C_{foram}$ in a 1:1 relationship (Figure 8.1). For our standard parameters, however, there is an offset for $\delta^{13}C_{foram}$ of around -0.2 to $-0.3‰$ with respect to $\delta^{13}C_{DIC}$. Field studies have shown that benthic foraminifera record $\delta^{13}C_{DIC}$ of bottom water or porewater with negative offsets. Only a few epibenthic species such as *C. wuellerstorfi*, in the absence of other effects, and possibly by chance, capture $\delta^{13}C_{DIC}$ more or less exactly in their $\delta^{13}C_{foram}$ (e.g. Woodruff et al. [1980]; Duplessy et al. [1988]). The implicit assumption that benthic foraminifera record $\delta^{13}C_{DIC}$ of bottom waters has also been challenged by Zeebe [2007]. He showed in a modelling study that porewater $\delta^{13}C_{DIC}$ influences bottom water $\delta^{13}C_{DIC}$ above the sediment-water interface. Even species like *C. wuellerstorfi* that tend to live on, or attach themselves to elevated structures on the seafloor [Linke and Lutze, 1993] may therefore be affected by porewater. For the purpose of this paper it is sufficient to note that $\delta^{13}C_{DIC}$ is taken up into the foraminiferal shell as expected in a 1:1 relationship, even if there is a constant offset. Here we focus on the other parameters that have had less attention in the past.

Temperature

The temperature sensitivity of $\delta^{13}C_{foram}$ is surprisingly high with +0.05‰ per °C. In the model this is achieved by changes in δ^{13}C of the carbonate species: as temperature increases $\delta^{13}C_{CO_2}$ and $\delta^{13}C_{CO_3^{2-}}$ become more enriched, whereas $\delta^{13}C_{HCO_3^-}$ more depleted. In combination with the related changes of the fractionation factors for calcite formation [Mook, 1986; Zeebe et al., 1999], $\delta^{13}C_{foram}$ is enriched with increasing temperature. This has important consequences for the interpretation of $\delta^{13}C_{foram}$ values of warmer or colder climate states (e.g. Section 8.3.4 below).

Laboratory measurements on the symbiont-barren planktonic foraminifer *Globigerina bulloides* show a decrease of $\delta^{13}C_{foram}$ by 0.11‰ per temperature increase of 1°C [Bemis et al., 2000], which differs both in quality and quantity from our model's increase. Bemis et al. [2000] hypothesise though that increasing temperatures induce higher respiration rates, which, in turn, introduce more depleted $\delta^{13}C_{CO_2}$ near the shell. After conversion from CO_2 to HCO_3^- and CO_3^{2-}, this carbon is subsequently taken up during calcification, thus lowering $\delta^{13}C_{foram}$. We also find a lowering of $\delta^{13}C_{foram}$ with increasing respiration rates (see Figure 8.3), which, depending on the increase in respiration rate, can easily overprint the signal caused by a temperature increase. In fact, our model requires an increase of the standard respiration rate by 0.5 nmol CO_2 h^{-1} from 0.41 to 0.91 nmol CO_2 h^{-1} in order to explain Bemis et al. [2000]'s hypothesis. Combined measurements of temperature and respiration would be highly desirable in order to test these results.

Pressure

The pressure effect on $\delta^{13}C_{foram}$ in the model is relatively small with a decrease of only 0.02 to 0.03‰ per increase of 100 bar. The difference in $\delta^{13}C_{foram}$ between a foraminifer living at a depth of 3000 m and 5000 m is therefore only about 0.05 to 0.06‰. Higher pressure causes

a change in the equilibrium constants of the chemical reactions between the different carbonate species in seawater: $[CO_3^{2-}]$ is reduced at higher pressures and its $\delta^{13}C$ value is more depleted. Upon uptake and calcification this lower $\delta^{13}C_{CO_3^{2-}}$ results in an equally depleted $\delta^{13}C_{foram}$.

$\delta^{13}C_{POC}$

It is well established that $\delta^{13}C_{POC}$ varies with latitude [Rau et al., 1989; Goericke and Fry, 1994]: at the equator $\delta^{13}C_{POC}$ is typically around $-20‰$, becoming more negative towards the poles with down to $-26‰$ in the Northern Hemisphere and $-35‰$ in the Southern Hemisphere. Differences in the two hemispheres can be explained by differences in temperature, $[CO_{2(aq)}]$ and growth rates (see e.g. Hofmann et al. [2000]). Another environment where $\delta^{13}C_{POC}$ values can be extremely low is near methane-venting structures on the seafloor (e.g. Mackensen et al. [2006]). Values of $-60‰$ have been reported by Hinrichs [2001]. Hill et al. [2004] found that foraminifera feed on this extremely depleted $\delta^{13}C_{POC}$, often in the form of bacteria.

The decrease of $\delta^{13}C_{foram}$ in our model with decreasing values of $\delta^{13}C_{POC}$ is expected. Respired CO_2 in the model is added to the external environment at the foraminiferal shell boundary. This is also the area where HCO_3^- or CO_3^{2-} are taken up by calcification. Conversion between the different carbonate species causes some of the low $\delta^{13}C_{CO_2}$ to become $\delta^{13}C_{HCO_3^-}$ and $\delta^{13}C_{CO_3^{2-}}$, which is subsequently taken up into the foraminiferal shell lowering $\delta^{13}C_{foram}$. Figure 8.4 demonstrates the effect of lower $\delta^{13}C_{POC}$ on the $\delta^{13}C$ values of the different carbon species as well as ΣCO_2. For standard model parameters the change in $\delta^{13}C_{foram}$ per change of $\delta^{13}C_{POC}$ is around 0.6%. In laboratory experiments Spero and Lea [1996] fed planktonic *G. bulloides* algal diets of differing $\delta^{13}C_{POC}$ values. This caused a marked effect in the $\delta^{13}C_{foram}$ values. Their observed change in $\delta^{13}C_{foram}$ per change of $\delta^{13}C_{POC}$ is around 3.5%, which is more than five times higher than our model results suggest. In the model the carbon has to take a detour via release of low $\delta^{13}C_{CO_2}$, subsequent conversion to HCO_3^- and CO_3^{2-}, and finally uptake and inclusion into the shell during calcification. The actual pathway of low $\delta^{13}C_{POC}$ inside benthic foraminifera via the

so called "carbon pool" (e.g. Bijma et al. [1999]), if it exists at all, is likely to be shorter and may therefore be more efficient at transmitting the $\delta^{13}C_{POC}$ signal into the shell's $\delta^{13}C_{foram}$.

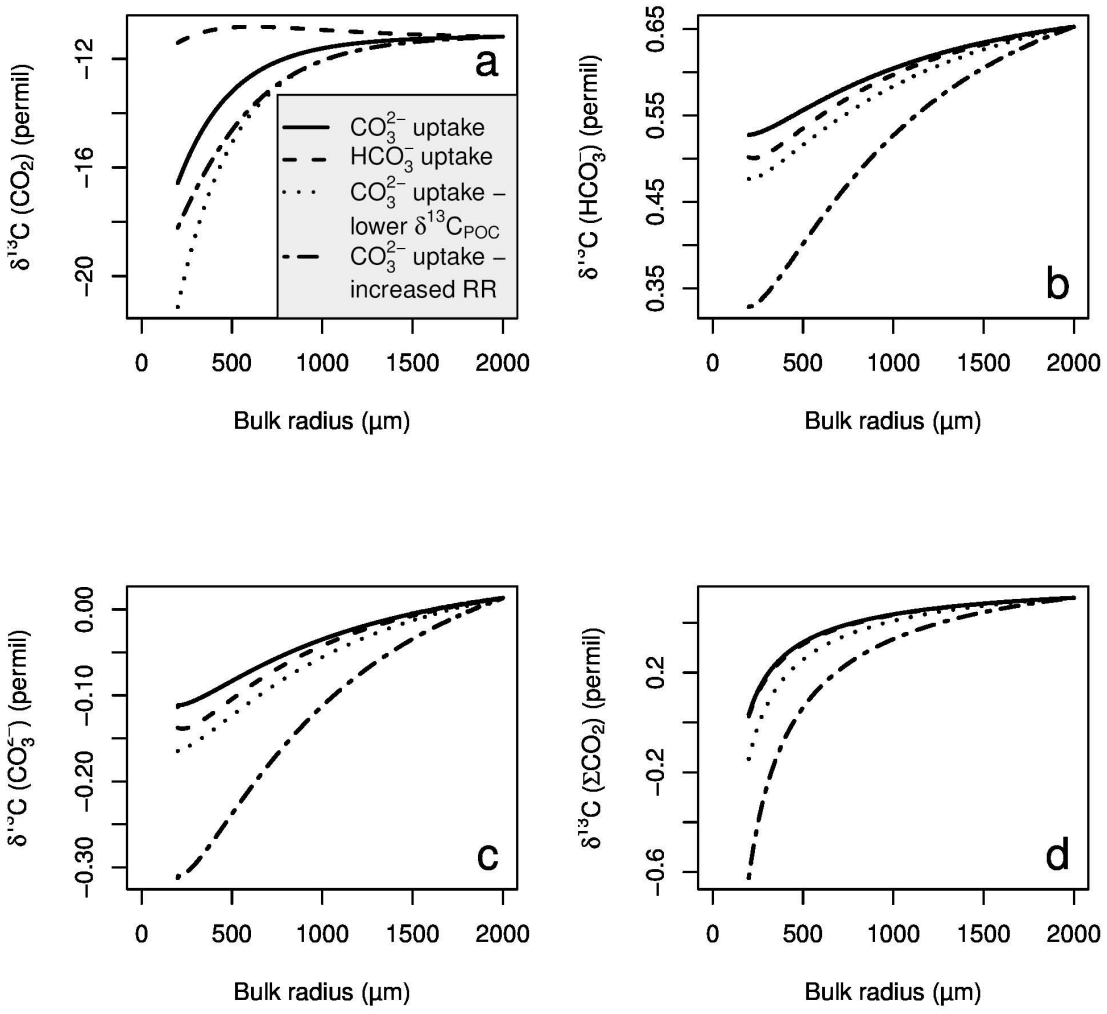

Figure 8.4: Model results for the δ^{13}C of CO_2 (a), HCO_3^- (b), CO_3^{2-} (c), and ΣCO_2 (d). The solid line represents CO_3^{2-} uptake at 0.28 nmol CO_3^{2-} h^{-1}, the dashed line is HCO_3^- uptake at 0.56 nmol HCO_3^- h^{-1} (same net calcification rate as for CO_3^{2-} uptake), the dotted line is CO_3^{2-} uptake with $\delta^{13}C_{POC}$ reduced from -21.9 to -30.0‰, and the dash-dotted line is CO_3^{2-} uptake at an increased respiration rate of 1.0 nmol CO_3^{2-} h^{-1}.

pH

The effect of pH on $\delta^{13}C_{foram}$ is more pronounced at pH values below 8, but is generally less than +0.1‰ per 0.1 pH decrease. The effect is a lot smaller than what was found by Spero et al. [1997] in planktonic foraminifera, which suggests that the model may not fully capture the pH/carbonate ion effect and its likely associated biological mechanism. The pH at the actual calcification site may be different, notably higher (e.g. de Nooijer et al. [2009]). Since cell-internal processes are not included in the model - we only consider the pH-driven fractionation between the carbonate species at the shell - we think that those are mostly responsible for the weak pH effect.

8.3.3 Vital parameters

Respiration rate

The respiration rate is the second most sensitive model parameter affecting $\delta^{13}C_{foram}$ after $\delta^{13}C_{DIC}$ (see Figure 8.3). An averaged decrease of 0.3‰ per increase of 1 nmol CO_2 h^{-1} adds a further challenge for interpreting $\delta^{13}C_{foram}$. In the model this is caused by more depleted $\delta^{13}C_{CO_2}$ which is diffusing out of the foraminifer. In turn, this is lowering the $\delta^{13}C$ values of HCO_3^- and CO_3^{2-}, either of which are taken up during calcification, and resulting in depleted $\delta^{13}C_{foram}$ values. Figure 8.4 illustrates the changes in $\delta^{13}C$ of the different carbon species for increased respiration rates. For calcification with CO_3^{2-}, respiration rates higher than 2.5 nmol CO_2 h^{-1} are not possible since the increased concentration of CO_2 causes an overall drop of pH near the shell, thus lowering and eventually depleting all remaining CO_3^{2-}.

How important is this effect? In this context it would be beneficial to know when foraminifera increase their metabolism and respire more. Several studies on benthic foraminifera have shown that they are dormant for most of the year, but increase their activity as soon as food is available (e.g. Moodley et al. [2002]). This is also the time when they build their new chambers and/or reproduce. To our knowledge, in-situ measurements of respiration rates on deep-sea benthic

foraminifera do not exist. Measurements on cultured benthic species vary across two orders of magnitude [Geslin et al., 2011]. Given the strong impact respiration rates have on $\delta^{13}C_{foram}$ in our model, measurements of respiration rates before, during and after chamber formation would be highly desirable to improve our understanding of $\delta^{13}C_{foram}$ signal formation.

Calcification rate and CO_3^{2-} vs. HCO_3^- uptake

The sensitivity of $\delta^{13}C_{foram}$ in response to changing calcification rates is less than 0.1‰, which is significantly lower than for changing respiration rates. At standard model parameters CO_3^{2-} uptake rates can only be as high as 0.6 nmol h^{-1} since at higher rates the CO_3^{2-} pool near the modelled shell boundary is depleted (see Figure 8.5). When bulk pH is increased, $[CO_3^{2-}]$ also increases allowing for higher calcification rates. In contrast, uptake of HCO_3^- is not limited since plenty of HCO_3^- is available. The associated changes in $\delta^{13}C_{foram}$ for HCO_3^- uptake are small compared to many of the other parameters tested in this study.

Our model results generally suggest that HCO_3^- uptake results in $\delta^{13}C_{foram}$ values that are lower by 0.07 to 0.08‰ compared to CO_3^{2-} uptake. This seems counter-intuitive as $\delta^{13}C_{HCO_3^-}$ is more than 0.6‰ higher than $\delta^{13}C_{CO_3^{2-}}$ (Figure 8.4). The simple explanation is that at 1.3°C the fractionation factor between HCO_3^- and $CaCO_3$ is -0.32‰, whereas for CO_3^{2-} and $CaCO_3$ it is +0.37, thus offsetting the differences in $\delta^{13}C$ of the two carbon species near the shell.

Which of the two carbon species is actually taken up during calcification of foraminifera has still not been established. The obvious choice seems to be CO_3^{2-} following the simple calcification equation

$$Ca^{2+} + CO_3^{2-} \rightleftharpoons CaCO_3. \tag{8.1}$$

Modelling results for the planktonic species *Globigerinoides sacculifer*, however, have shown that carbonate ion supply can be insufficient to account for measured calcification rates [Wolf-

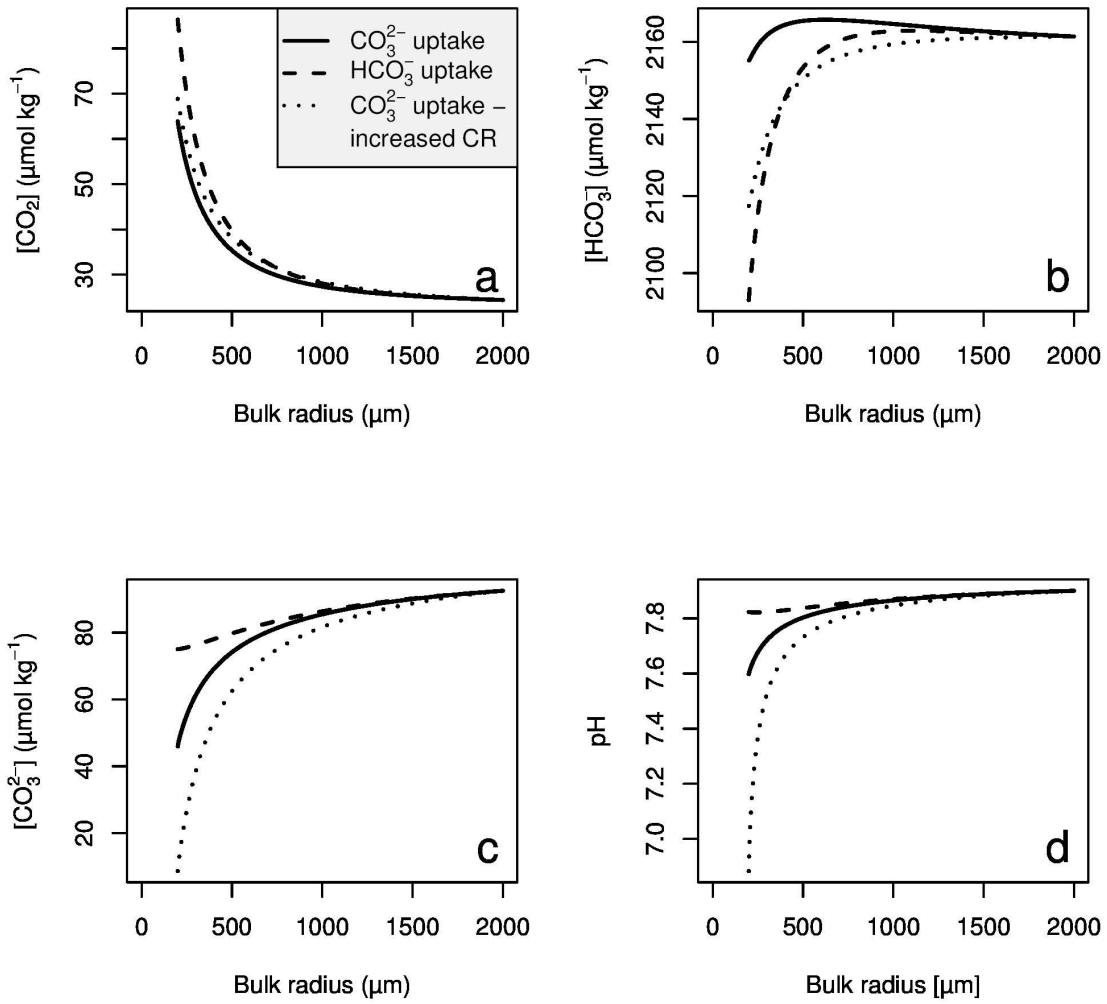

Figure 8.5: Model results for the bulk concentrations of CO_2 (a), HCO_3^- (b), CO_3^{2-} (c), and pH (d). The solid line represents CO_3^{2-} uptake at 0.28 nmol CO_3^{2-} h^{-1}, the dashed line is HCO_3^- uptake at 0.56 nmol HCO_3^- h^{-1} (same net calcification rate as for CO_3^{2-} uptake), and the dotted line is CO_3^{2-} uptake at an increased rate of 0.60 nmol CO_3^{2-} h^{-1}. At this elevated calcification rate the CO_3^{2-} concentration at the shell boundary is approaching zero (c) - higher rates are physically not possible.

Gladrow et al., 1999], just as for our results at rates higher than 0.6 nmol CO_3^{2-} h^{-1}. Therefore some foraminifera may require an internal carbon pool (e.g. Erez [2003]) from which carbon is

taken during calcification, or partly (maybe fully) employ bicarbonate ion:

$$Ca^{2+} + 2\,HCO_3^- \rightleftharpoons CaCO_3 + H_2O + CO_2. \tag{8.2}$$

Another process to overcome the depletion of the carbonate ion pool near the shell is the elevation of internal pH as has been described by, for instance, de Nooijer et al. [2009]. This could create a sufficiently high concentration of carbonate ion inside the foraminifer which is supplied by uptake and subsequent conversion of HCO_3^- and/or CO_2 to CO_3^{2-}. Yet another mechanism could be the foraminifer's pseudopodial network that can reach out into the ambient seawater and harvest more CO_3^{2-} from a bigger volume than would be possible by simple cross-membrane transport at the shell boundary. Here we cannot answer which of these mechanisms is at work, but from the model results it is obvious that one or more of them are required in order to allow the foraminifer to calcify at rates greater then 0.6 nmol h^{-1} when using CO_3^{2-}.

8.3.4 Combined scenarios

The Glacial

Our glacial results (Table 8.4) suggest that we may explain about two-thirds of the observed interglacial to glacial drop in $\delta^{13}C_{foram}$ (global ocean average of $-0.32‰$ [Duplessy et al., 1988]) by changes in temperature, pH and $\delta^{13}C_{POC}$. Interestingly, temperature is the main driver in our model, whereas the carbonate ion effect (or pH effect) has a relatively minor impact. Spero et al. [1997] found that increasing carbonate ion concentrations result in a decrease of planktonic $\delta^{13}C_{foram}$, which they put forward as another possible explanation for the lowered $\delta^{13}C_{foram}$ found in the Last Glacial Maximum (see also Lea et al. [1999]). To our knowledge the temperature-$\delta^{13}C_{foram}$ relationship has not been assessed before for benthic foraminifera in the context of glacial-interglacial changes.

Admittedly, our 'one-size-fits-all' approach is a bit rough: Different core sites have of course

experienced different parameter changes during the glacial and each core needs to be looked at in detail. Deep ocean temperatures have not decreased everywhere by the average 3.25 ± 0.55°C reported by Clark et al. [2009]. The same is true for pH: Hönisch et al. [2008] found that pH in the southeast Atlantic Ocean during the LGM was increased above 3500 m water depth by up to 0.1 pH units, but decreased below that depth (-0.07 pH units). The Pacific may have experienced increases of up to 0.5 pH units [Sanyal et al., 1997]. Our estimate of a decreased $\delta^{13}C_{POC}$ in the glacial is probably an upper limit. The $\delta^{13}C_{POC}$ value formed by algae is not only depending on SSTs, but also on the concentration of $CO_{2(aq)}$ and growth rates, which introduce a seasonal signal [Goericke and Fry, 1994; Hofmann et al., 2000]. Therefore, depending on where $\delta^{13}C_{POC}$ is formed, the final $\delta^{13}C_{foram}$ values may change, but probably by no more than 0.05‰. A logical next step would be to apply our model to a combined carbon cycle/general ocean circulation model in order to obtain spatial patterns for $\delta^{13}C_{foram}$. These could then be compared to observational data from sediment cores à la Hesse et al. [2011].

Phytodetritus layer

So far most of the effect of a phytodetritus layer was attributed to lowering of $\delta^{13}C_{DIC}$ in the layer's interstitial waters. Our results of -0.23‰ (Table 8.4) allow us to explain more than half of the typical reduction of -0.4‰ found in some phytodetritus layer locations (see e.g. Bickert and Mackensen [2004]; Zarriess and Mackensen [2011]) without invoking changes in $\delta^{13}C_{DIC}$. The increased respiration rate is the main driver in our model. Whether or not a respiration rate increase of 1 nmol CO_2 h^{-1} is realistic cannot be said for certain, since the available respiration rate measurements have all been taken during times of food unavailability [Hannah et al., 1994; Nomaki et al., 2007; Geslin et al., 2011].

8.4 Sensitivity experiment conclusions

The objective of this study is to test the sensitivity of δ^{13}C in benthic foraminiferal shells to different physical, chemical and biological parameters using a reaction-diffusion model for calcification of foraminifera. Changes in $\delta^{13}C_{DIC}$ cause equal changes in $\delta^{13}C_{foram}$ in the model. Offsets between $\delta^{13}C_{DIC}$ and $\delta^{13}C_{foram}$ depend on a variety of physical, chemical and biological parameters. Temperature, respiration rate and pH have a marked effect on $\delta^{13}C_{foram}$, whereas salinity, pressure, $\delta^{13}C_{POC}$, total alkalinity and calcification rate are less important.

The model can account for two-thirds of the drop in glacial $\delta^{13}C_{foram}$ with respect to Holocene values by a combination of lower temperature, higher pH and a shift in $\delta^{13}C_{POC}$, with temperature causing most of the signal. We can explain more than half of the decrease in $\delta^{13}C_{foram}$ of foraminifera living in and feeding on phytodetrital layers without invoking changes in $\delta^{13}C_{DIC}$. Critically, this decrease is depending on the respiration rate.

Possible future uses of the model include the application to coupled carbon cycle/general ocean circulation models in order to assess spatial patterns, or a closer look at ontogenetic processes and the associated $\delta^{13}C_{foram}$ changes.

Chapter 9

Towards a mechanistic interpretation of δ^{13}C: modelling calcification in benthic foraminifera and its application to palaeoceanographic model scenarios

9.1 Methods

The basic methodological approach described in this chapter is the combination of previously unconnected models in order to come closer to the long-standing goal of modelling directly what is found in sediment cores, in our case $\delta^{13}C_{foram}$. For this we are using output from the coupled HAMOCC2s (see Heinze and Maier-Reimer [1999]; Heinze et al. [1999] and Chapter 5) and LSG models [Maier-Reimer et al., 1993] in order to drive the diffusion-reaction foraminifera calcification model (FCM) developed by Wolf-Gladrow et al. [1999] and Zeebe et al. [1999] and adapted for benthic foraminifera by Hesse et al. [in review] (see also Chapter 5). We assess the

uncertainties in the $\delta^{13}C_{foram}$ signal on an ocean-wide scale, and in association with different model scenarios. As described in Chapter 5, these scenarios include a pre-industrial control run as well as two different LGM scenarios based on GLAMAP SSTs (see Chapter 4), building on previous studies by Butzin et al. [2005] and Hesse et al. [2011].

The three considered model scenarios each have their own distinct set of values for temperature, salinity, $\delta^{13}C_{DIC}$, transport rates etc. The only FCM parameter that we used for additional sensitivity experiments is respiration rate, which is the vital parameter with the strongest impact on $\delta^{13}C_{foram}$ [Hesse et al., in review]. Our standard respiration rate is set at 0.41 nmol CO_2 h^{-1} based on Nomaki et al. [2007]. Additionally, we did sensitivity experiments for a ten times reduced respiration rate of 0.041 nmol CO_2 h^{-1}, as well as a doubled respiration rate of 0.82 nmol CO_2 h^{-1}.

9.2 Combined modelling results

9.2.1 $\delta^{13}C_{foram}$ vs $\delta^{13}C_{DIC}$

Figures 9.1 and 9.2 show the model results for the control run and the two glacial scenarios GB and GS for $\delta^{13}C_{DIC}$, for $\delta^{13}C_{foram}$ as modelled with the FCM, and also the anomaly between $\delta^{13}C_{foram}$ and $\delta^{13}C_{DIC}$. For each model scenario $\delta^{13}C_{foram}$ in the deep ocean is lower than $\delta^{13}C_{DIC}$ by more than 0.2‰, whereas in the surface ocean between 40°S and 40°N $\delta^{13}C_{foram}$ is enriched by $\geq$0.2‰ compared to $\delta^{13}C_{DIC}$. In the two glacial scenarios the northern North Atlantic above 2 km water depth shows the strongest depletion of $\delta^{13}C_{foram}$ with respect to $\delta^{13}C_{DIC}$.

9.2.2 LGM-to-present-day anomalies

The δ^{13}C anomalies between the glacial model runs and the control run are shown in Figure 9.3 for the western Atlantic Ocean and in Figure 9.4 for the eastern Atlantic Ocean. Anomalies

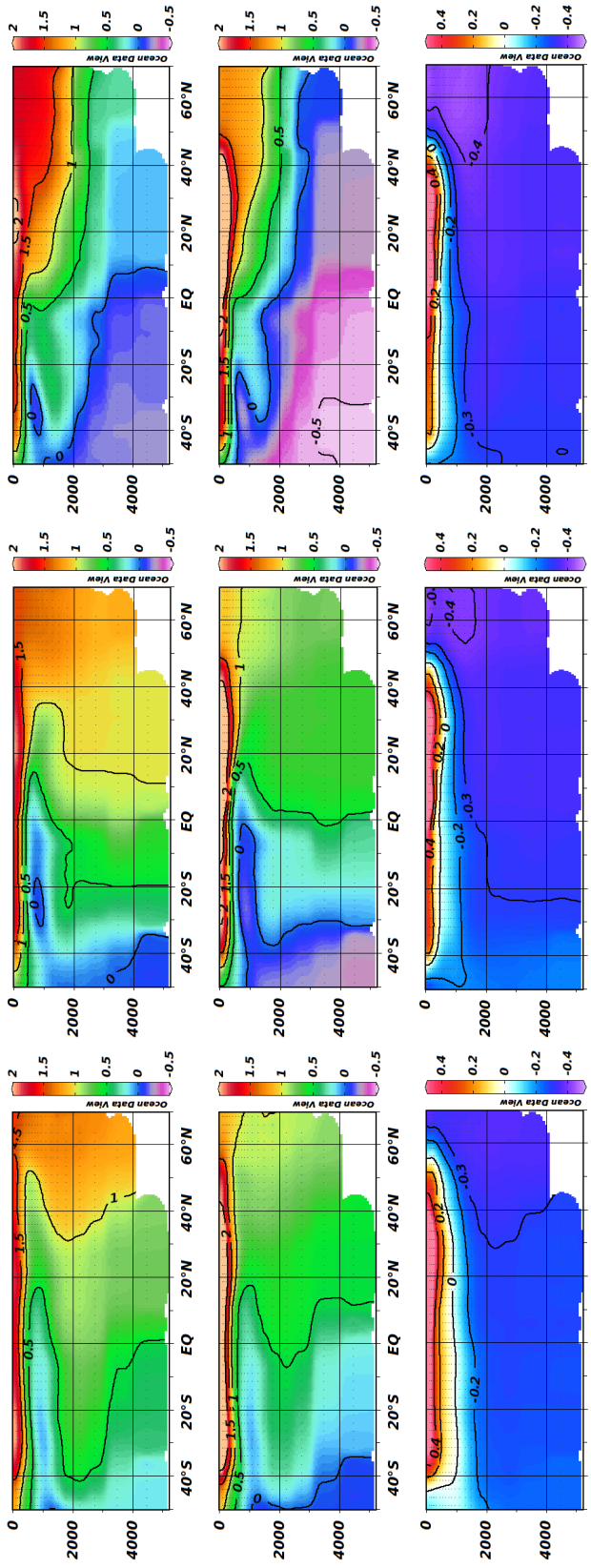

Figure 9.1: Control run (left column), glacial scenario GB (middle column) and glacial scenario GS (right column) $\delta^{13}C_{DIC}$ data (top row), $\delta^{13}C_{foram}$ data (middle row), and the difference between $\delta^{13}C_{foram}$ and $\delta^{13}C_{DIC}$ (bottom row) in the western Atlantic (all in ‰). Including the FCM leads to a depletion of $\delta^{13}C$ of more than 0.2‰ in the deep ocean and a marked enrichment of $\delta^{13}C$ in the surface ocean between 40°S and 40°N.

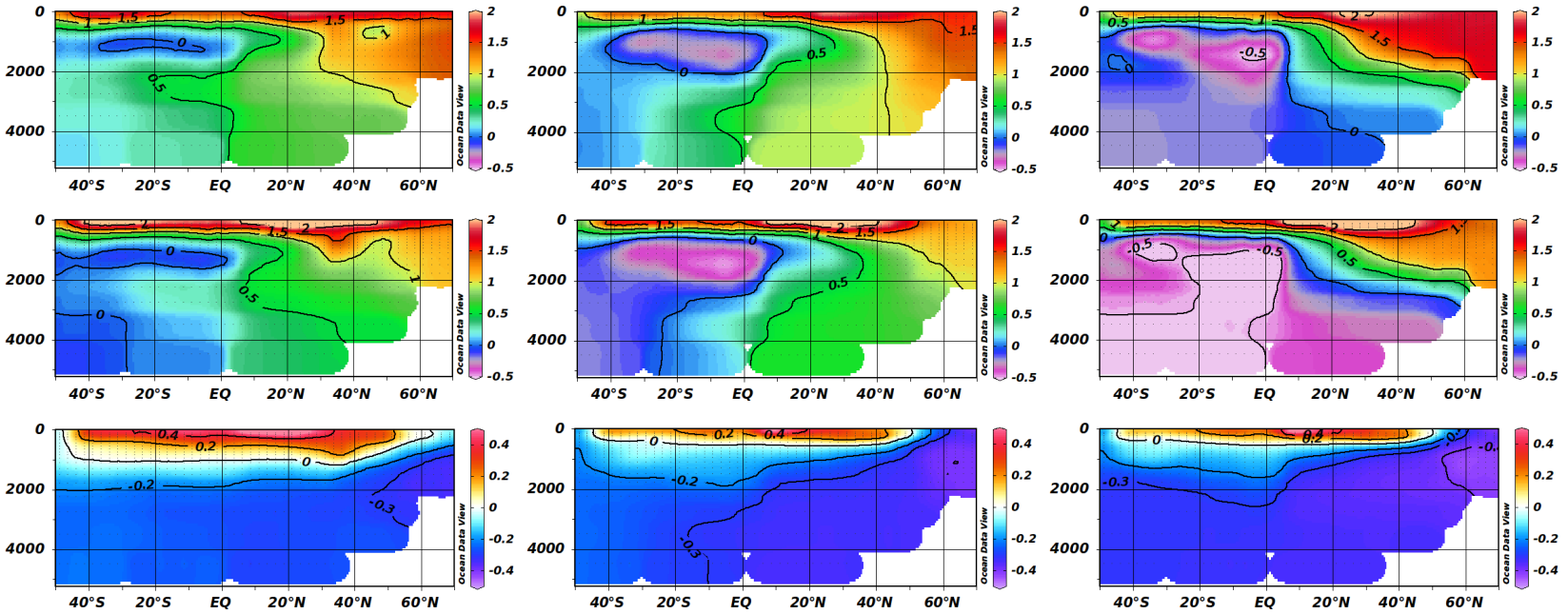

Figure 9.2: Same as in Figure 9.1, but for the eastern Atlantic. The depletion and enrichment of δ^{13}C in the deep ocean and the surface ocean, respectively, is similar to that seen in Figure 9.1.

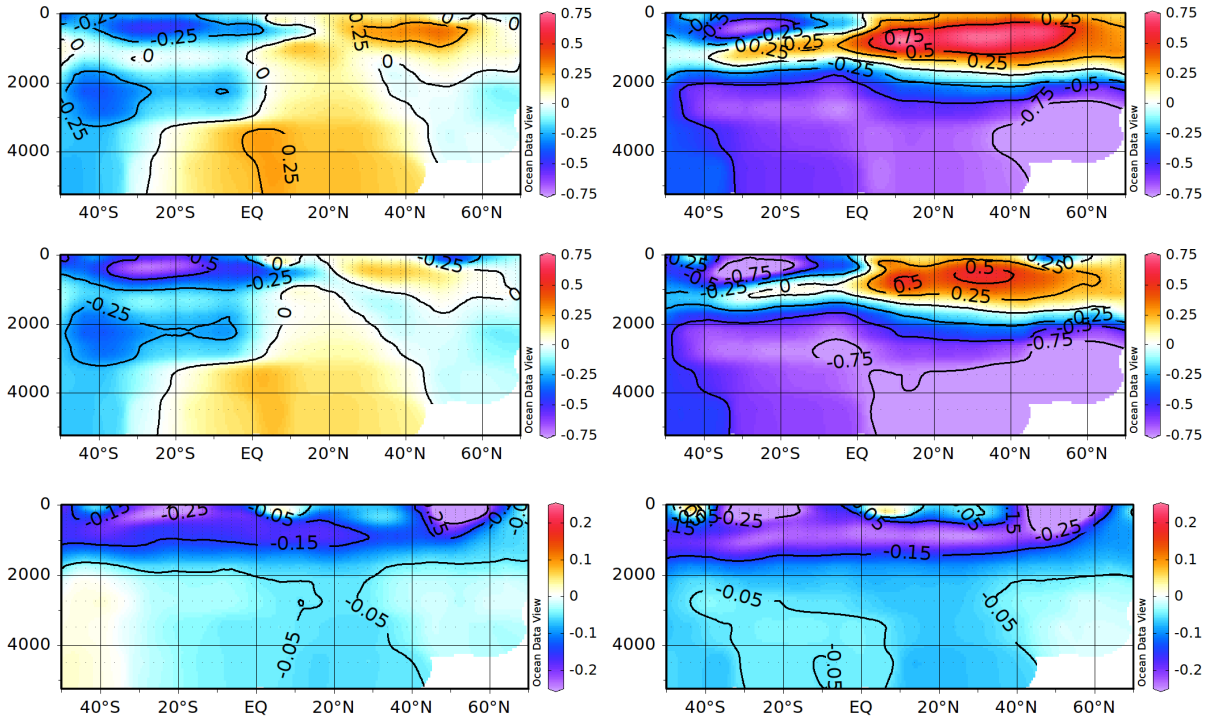

Figure 9.3: LGM-to-present-day anomaly plots for the western Atlantic Ocean for scenarios GB (left column) and GS (right column). Top row: anomaly of modelled glacial $\delta^{13}C_{DIC}$ with respect to control $\delta^{13}C_{DIC}$. Middle row: anomaly of modelled glacial $\delta^{13}C_{foram}$ with respect to control $\delta^{13}C_{foram}$. Bottom row: the difference between the $\delta^{13}C_{foram}$ anomaly and the $\delta^{13}C_{DIC}$ anomaly. All anomalies are in ‰. Note the different scale bar for the bottom row plots.

in $\delta^{13}C_{DIC}$ and $\delta^{13}C_{foram}$ (top row and middle row in Figures 9.3 and 9.4, respectively) show a similar pattern for each glacial scenario, but there are distinct differences between GB and GS. GB shows a more ^{13}C-enriched deep ocean compared to control run, whereas GS' deep ocean is strongly depleted in $\delta^{13}C$. This is true for both $\delta^{13}C_{DIC}$ and $\delta^{13}C_{foram}$. The anomalies for GB and GS both share a common feature in the upper 1500 to 2000 meters: the North Atlantic is more enriched in $\delta^{13}C$, and the South Atlantic is split between a depleted uppermost cell in the top 1000 meters and a tongue of less depleted $\delta^{13}C$ between 1000 and 2000 meters water depth. Again, this is true for both $\delta^{13}C_{DIC}$ and $\delta^{13}C_{foram}$ with $\delta^{13}C_{foram}$ being more depleted than $\delta^{13}C_{DIC}$. The amount of the depletion can be seen in the bottom rows of Figures 9.3 and 9.4: here the differences between the $\delta^{13}C_{foram}$ anomaly and the $\delta^{13}C_{DIC}$ anomaly are displayed. On

average, the deep ocean anomaly in $\delta^{13}C_{foram}$ is lower by 0.05 to 0.10‰ compared to the anomaly in $\delta^{13}C_{DIC}$.

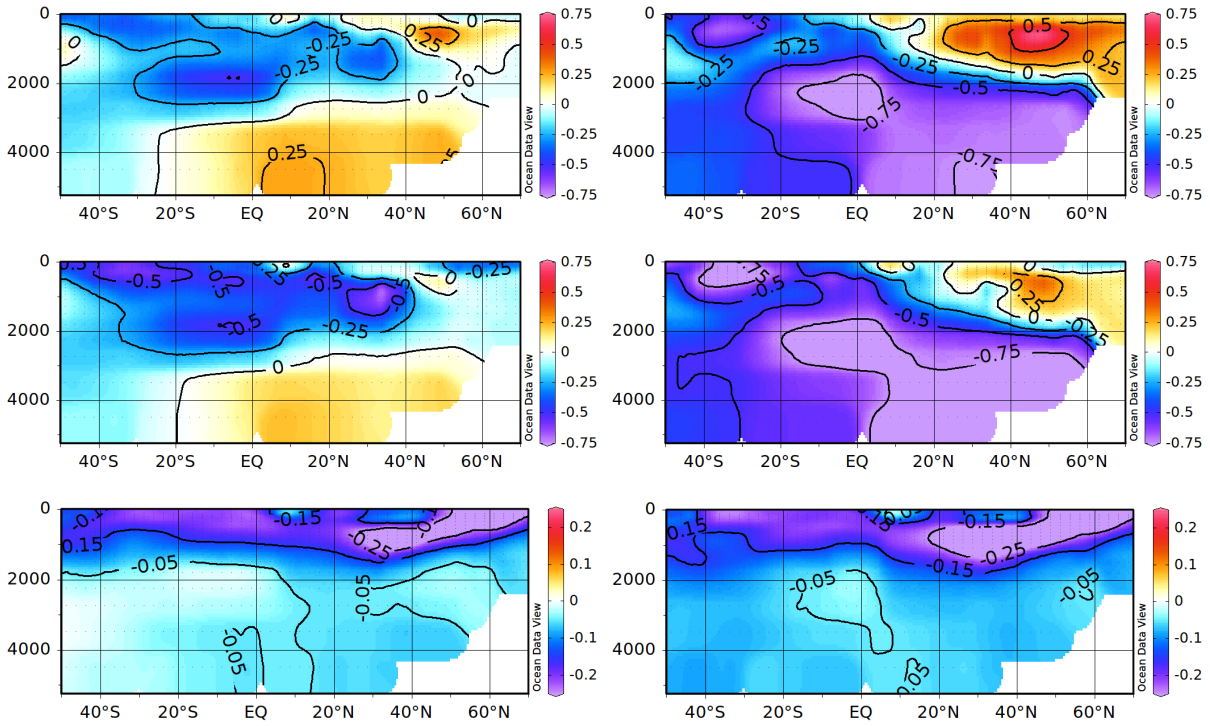

Figure 9.4: Same as Figure 9.3, but in the eastern Atlantic Ocean.

9.2.3 Respiration rate

The effect of changing the respiration rate in the FCM is shown in Figure 9.5 for the control run. When the respiration rate is reduced ten times, the final $\delta^{13}C_{foram}$ is less negative than for the standard respiration rate. In contrast, a doubled respiration rate causes $\delta^{13}C_{foram}$ to be even more depleted with respect to $\delta^{13}C_{DIC}$ than the standard respiration rate. In both cases the effect of a lowered/increased respiration rate is most pronounced in the surface ocean (up to $\pm$0.2‰), and seems to be reduced to $\pm$0.1‰ as the water mass ages. For the glacial scenarios (not shown) the pattern is similar.

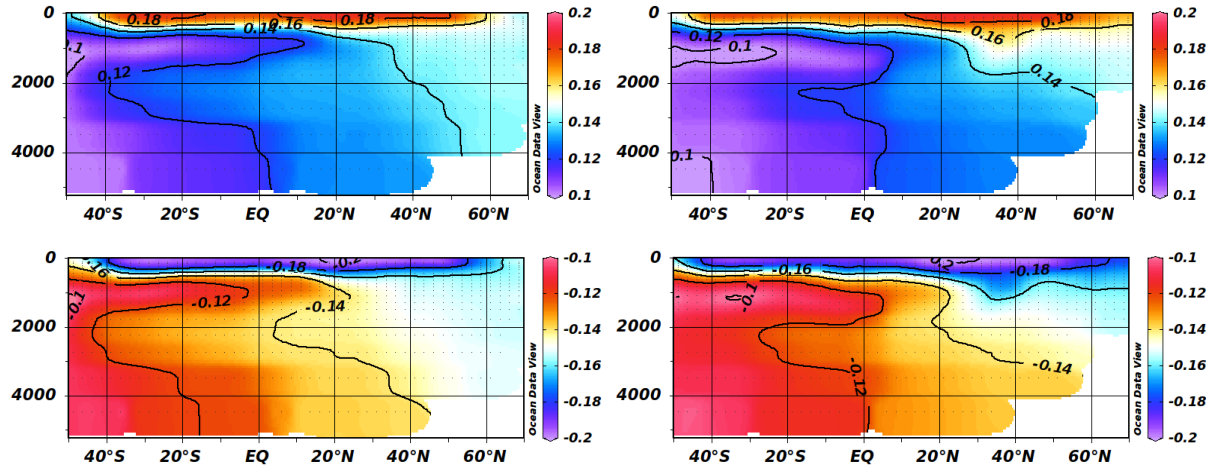

Figure 9.5: Respiration sensitivity experiments for the control run: Anomalies (in ‰) with respect to the standard respiration rate for a ten times lowered respiration rate (top row) and a doubled respiration rate (bottom row) for the western and eastern Atlantic (left and right column, respectively). A lowered respiration rate reduces the difference between $\delta^{13}C_{foram}$ and $\delta^{13}C_{DIC}$, whereas an increased respiration rate causes a further drop in $\delta^{13}C_{foram}$ with respect to $\delta^{13}C_{DIC}$. Note the scale bar differences between top and bottom row.

9.2.4 Model-data comparison

The results of a quantitative comparison between reconstructions (see Chapter 6 on sediment core $\delta^{13}C$ data) and the different model scenarios are summarised in the Taylor diagrams [Taylor, 2001] in Figure 9.6 and shown in Table 9.1. For the control run simulated without the FCM, both the correlation coefficient r and the RMS difference are highest and lowest, respectively. For glacial scenarios GB and GS, including the FCM improves both r and the RMS difference, but only slightly (see Table 9.1). Different respiration rates do not cause changes in r in any of the scenarios, and the RMS difference hardly varies between different respiration rates.

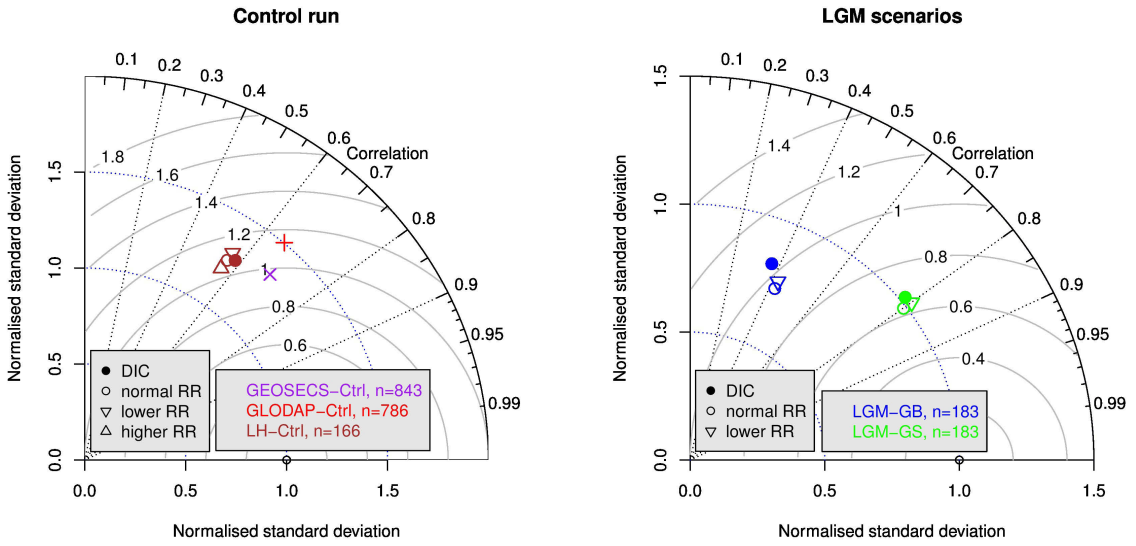

Figure 9.6: Taylor diagram [Taylor, 2001] showing the correlations and standard deviations of the various model scenarios: Present-day $\delta^{13}C_{DIC}$ measurements (GEOSECS and GLODAP) and Late Holocene (LH) $\delta^{13}C_{foram}$ compared to control run $\delta^{13}C_{DIC}$ and $\delta^{13}C_{foram}$, respectively (left); LGM $\delta^{13}C_{foram}$ compared to $\delta^{13}C_{DIC}$ and $\delta^{13}C_{foram}$ of glacial scenarios GB and GS (right).

	Control run				**GB**			**GS**		
	DIC	Foram RR			DIC	Foram RR		DIC	Foram RR	
		low	*std*	*high*		*low*	*std*		*low*	*std*
correlation coeff. *r*	0.58	0.56	0.56	0.56	0.37	0.42	0.42	0.78	0.80	0.80
RMS difference	0.32	0.33	0.33	0.32	0.57	0.52	0.53	0.37	0.35	0.35

Table 9.1: Correlation coefficients and averaged RMS differences for the control run and the two glacial scenarios when compared to present-day/Late Holocene data and LGM data, respectively [RR = respiration rate; std = standard].

9.3 Combined modelling discussion

9.3.1 $\delta^{13}C_{foram}$ vs $\delta^{13}C_{DIC}$

Figures 9.1 and 9.2 demonstrate that the FCM has a strong impact on $\delta^{13}C_{DIC}$, making the final $\delta^{13}C_{foram}$ lower in the deep ocean below 2 km water depth and higher in most of the surface ocean. Building on the paper by Hesse et al. [in review] (see also Chapter 8), where they did

parameter sensitivity studies with the stand-alone FCM, it is obvious that temperature, pH and respiration rate must play a role in the modelled differences between $\delta^{13}C_{DIC}$ and $\delta^{13}C_{foram}$. In the following paragraphs we are going to look at each of these parameters in turn.

Temperature

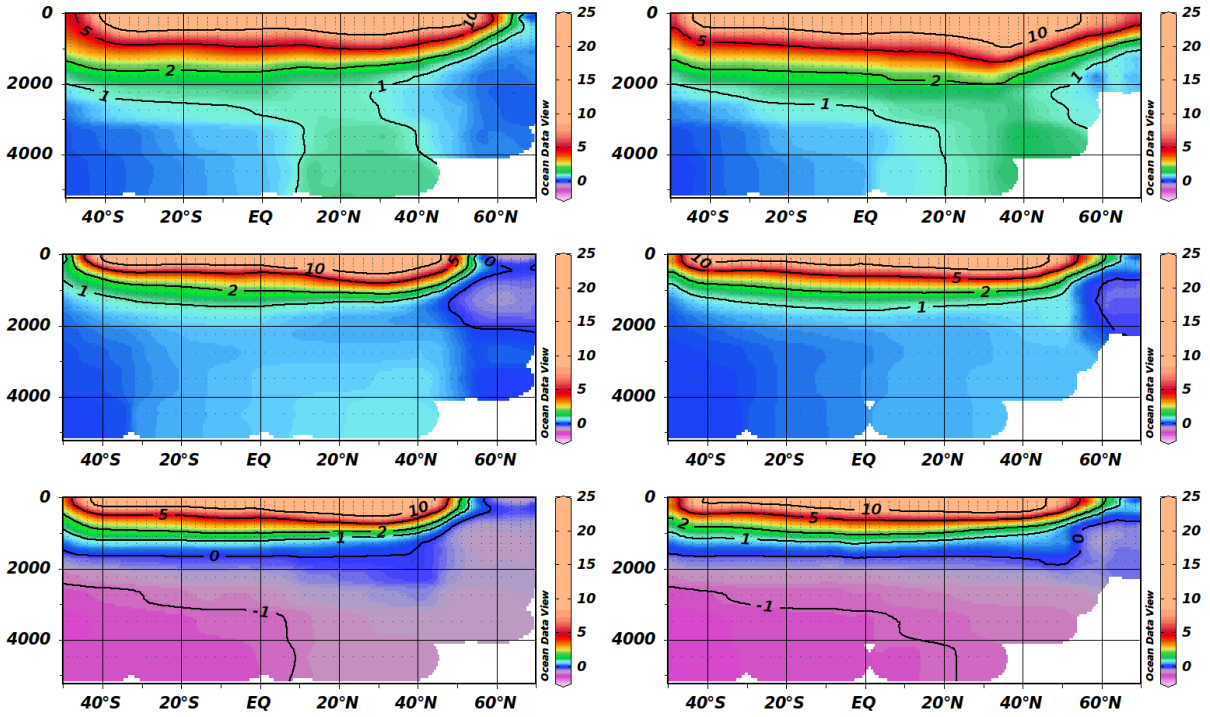

Figure 9.7: Temperature data in °C for the control run (top row), scenario GB (middle row), and scenario GS (bottom row) in the western Atlantic (left column) and the eastern Atlantic (right column). GB is only marginally colder in the deep ocean when compared to the control run. GS, however, has a relatively steep thermocline and is substantially colder in the deep ocean than the control run.

Looking at Figure 9.7 and comparing it to the $\delta^{13}C_{foram} - \delta^{13}C_{DIC}$ difference plots in Figures 9.1 and 9.2 there is a clear similarity in the displayed pattern: warm temperatures lead to higher $\delta^{13}C_{foram}$ values, whereas cold temperatures lead to lower $\delta^{13}C_{foram}$ values. Hesse et al. [in review] found that an increase in temperature by 1°C causes an increase in $\delta^{13}C_{foram}$ of 0.05‰, so the results are expected. But temperature is not the only parameter influencing the differences be-

tween $\delta^{13}C_{foram}$ and $\delta^{13}C_{DIC}$. For each model scenario the δ^{13}C differences are most pronounced in the northern North Atlantic, where temperatures are very low in each model scenario. Temperatures are, however, also very low in the deeper Southern Ocean, which is not reflected in the δ^{13}C anomaly (Figures 9.1 and 9.2). Therefore, we have to look further and consider differences in pH.

pH

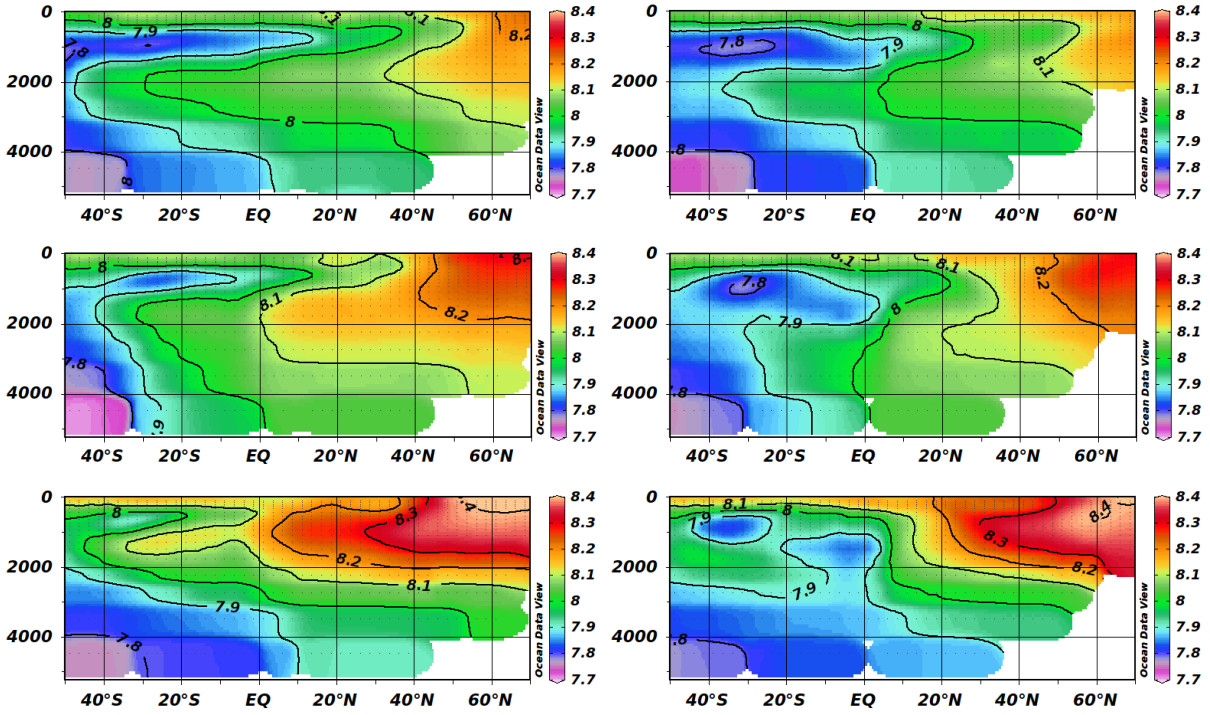

Figure 9.8: Same as Figure 9.7, but for pH data. Intermediate, deep and bottom waters can clearly be distinguished for the control run and the two glacial scenarios. Broadly speaking, the pH gradient between the NADW and AABW source regions steepens from the control run via GB to GS, which seems to be dominantly caused by a strong pH increase in the NADW source region, especially for GS.

The pH distribution (Figure 9.8) shows a strong gradient between the upper 2000 m in the northern North Atlantic and the deep Southern Ocean, which is steepening from the control run via GB to GS. For the stand-alone FCM, Hesse et al. [in review] found that the response of

$\delta^{13}C_{foram}$ to changes in pH of $+0.1$ is about $-0.08‰$ for pH < 7.6, decreasing to about $-0.02‰$ for pH > 8.2 (see Chapter 2). Hence the effect of pH on $\delta^{13}C_{foram}$ should be most pronounced in the deep Southern Ocean. This also seems to be what we are observing: low temperatures in the deep Southern Ocean should lower $\delta^{13}C_{foram}$, but the low pH counter-acts the temperature signal to make the $\delta^{13}C_{foram} - \delta^{13}C_{DIC}$ difference plots more homogenous in the deep ocean as a whole.

9.3.2 LGM-to-present-day anomalies

The $\delta^{13}C_{DIC}$ anomaly plots in the top row of Figures 9.3 and 9.4 show strong differences between the two glacial scenarios GB and GS. For GB the anomaly pattern is heterogeneous and the amplitudes rarely exceed $\pm 0.25‰$. The positive anomalies in the central deep Atlantic Ocean can be explained by GB's reduced negative overturning cell at depth compared to the control run (Figure 9.9). The strong gradient seen in the anomalies for GS with positive values in the surface ocean and negative values at depth are also caused by changes in the circulation regime. GS is characterised by a shallower positive overturning cell in the North Atlantic, and an extended negative cell in the deep ocean (Figure 9.9). Anomaly amplitudes are higher in GS, spanning a range of $+0.75‰$ in the upper North Atlantic to $-0.75‰$ in the deep North Atlantic.

For the anomalies in $\delta^{13}C_{foram}$ the overall anomaly pattern is similar to the $\delta^{13}C_{DIC}$ anomalies, but there is a shift to more negative anomalies (see bottom rows of Figures 9.3 and 9.4). The difference between $\delta^{13}C_{foram}$ and $\delta^{13}C_{DIC}$ anomalies in the deep ocean below 2 km water depth is between -0.05 to $-0.10‰$ for both GB and GS. In the upper ocean there is a pronounced band centred at approximately 1000 m water depth which shows the strongest difference between $\delta^{13}C_{foram}$ and $\delta^{13}C_{DIC}$ anomalies of up to $-0.25‰$. The band is the result of small negative shifts from $\delta^{13}C_{DIC}$ to $\delta^{13}C_{foram}$ in the oceanic regions where the strongest $\delta^{13}C$ gradients exist. For instance, a small shift and widening of the relatively low $\delta^{13}C$ AAIW region caused by the FCM causes a more pronounced negative LGM-to-present-day anomaly, which is then also visible in the differences between the $\delta^{13}C_{foram}$ and $\delta^{13}C_{DIC}$ anomalies.

The anomaly plots show that even though the absolut changes in δ^{13}C introduced by the inclusion of the FCM are greater than $-0.2‰$ in the deep ocean, the differences in the LGM-to-present-day anomalies are only between -0.05 to $-0.10‰$.

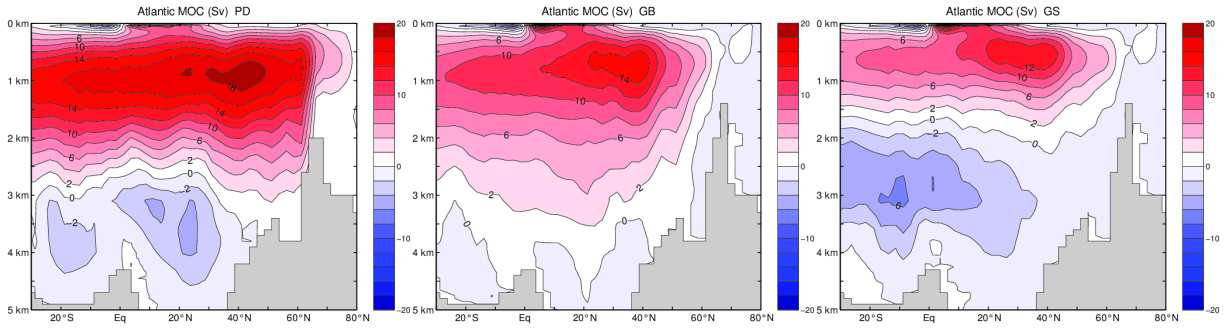

Figure 9.9: The AMOC in Sv for the control run (left), glacial scenario GB (middle), and glacial scenario GS (right). Scenario GB has a deepened and slightly reduced positive AMOC compared to the control run, whereas in GS the positive AMOC is shoaled and reduced by around 40% with respect to the control run. GS also has an increased negative AMOC at depth.

9.3.3 Respiration rate uncertainties

Our results suggest that the respiration rate plays an important role in determining $\delta^{13}C_{foram}$. From Figure 9.5 we can see that $\delta^{13}C_{foram}$ can change by up to $\pm 0.2‰$ depending on the actual respiration rate. And the actual respiration rate is - to the best of our knowledge - not very well constrained. Our standard respiration rate of 0.41 nmol CO_2 h^{-1} is based on a measurement on *C. wuellerstorfi* by Nomaki et al. [2007]. This value is at the higher end of measured benthic foraminiferal respiration rates, that can overall span two orders of magnitude or more [Geslin et al., 2011]. Respiration rate measurements have normally been taken at times when the foraminifera were not feeding, which may suggest that the so measured respiration rates are low compared to those the foraminifera exhibit when building new chambers, which is the process we are interested in. One could also argue, however, that the measurement process stresses the foraminifera, which could potentially also result in higher respiration rates. Basically, we don't know. Measuring respiration rates is a very delicate procedure, and doing it in-situ, which may

reduce/eliminate stress on the foraminifera, would be even more so. Therefore, for the moment we have to accept the uncertainty introduced by not knowing the respiration rate exactly.

9.3.4 Model-data comparison

The results of the model-data comparison (see Figure 9.6 and Table 9.1) show that the inclusion of the FCM improves the model-data fit for both glacial scenarios. For the previously favoured scenario GS (see Butzin et al. [2005], Hesse et al. [2011] and Chapter 7) the correlation coefficient increased from 0.78 to 0.80. Scenario GB experiences a stronger increase in r from 0.37 to 0.42, but on a much lower level. Clearly scenario GS with its altered freshwater balance in the Southern Ocean is still fitting reconstructions best, also with respect to its RMS difference and its variance, which is almost identical to the variance of the reconstructed sediment $\delta^{13}C_{foram}$ values (see the normalised standard deviation arc at 1.0 in Figure 9.6, right hand side). Interestingly, the different respiration rate scenarios do not influence the model-data comparison results. Overall the model-data comparison results are encouraging and show that the inclusion of the processes in the micro-environment around foraminifera do not change the main interpretation of $\delta^{13}C_{foram}$.

9.3.5 Limitations

The FCM does not include any processes that may happen within the foraminifera. Recent work by de Nooijer et al. [2009] has shown that internal processes may be very important in benthic foraminifera, especially when it comes to the calcification process. For instance, we do not know whether respired carbon is directly transported to the calcification site without taking the detour via release into the bulk, subsequent conversion of CO_2 to HCO_3^- and CO_3^{2-}, and finally re-uptake, as it is described in our model. We believe, however, that our model is an important first step to assess the processes acting during calcification, even if internal processes are neglected for the moment.

Possible drawbacks of the LSG and HAMOCC2s have already been discussed in Chapter 7. The globally averaged wind fields that are used for driving HAMOCC2s reproduce air-sea exchange in the Southern Ocean unrealistically and therefore underestimate $\delta^{13}C_{DIC}$ for AAIW [Hesse et al., 2011]. This has no consequences, however, for the deep ocean below 2000 meters water depth.

9.4 Implications

Combining all the evidence presented above, we can say that the addition of the FCM causes some substantial differences in absolut $\delta^{13}C_{foram}$ values, which can be explained by the effects of temperature, pH, and the circulation regime. LGM-to-present-day anomalies, however, are only slightly different when comparing model runs with and without the FCM. Uncertainties due to our limited knowledge about respiration rates amount to $\pm$(0.10 to 0.15)‰ in $\delta^{13}C_{foram}$, where the higher uncertainty is found in the northern North Atlantic (see Figure 9.5). The model-data comparison shows that both LGM scenarios fit slightly better to the data upon the inclusion of the FCM. GS is still the best fitting model scenario with an increased correlation coefficient of 0.80 (from previously 0.78), a reduced average RMS difference of 0.35‰ (down from 0.37‰), and a variance of the model data that is close to the variance of the sediment core reconstructions. Scenario GB also improves its performance in the model-data comparison, but its overall performance is still a lot worse than for GS.

For palaeoceanographers these results are encouraging as they corroborate previous findings of a shoaled positive North Atlantic overturning cell and an expanded negative overturning cell in the deep Atlantic Ocean, both from reconstructions (e.g. Adkins et al. [2002]; Curry and Oppo [2005]; Lynch-Stieglitz et al. [2007]) and modelling (e.g. Shin et al. [2003b]; Butzin et al. [2005]). The relatively small differences in the anomalies between $\delta^{13}C_{foram}$ and $\delta^{13}C_{DIC}$ further underline that, when considering anomalies rather than absolute values, the interpretation of the

data or model is less dependent on systematic uncertainties introduced by e.g. habitat effects.

The substantial absolut changes from $\delta^{13}C_{DIC}$ to $\delta^{13}C_{foram}$ introduced by the FCM can be explained in the model by the different model parameters. Yet, the strong surface to deep ocean gradient is suspicious, since such strong gradients have not been reported before. From a physiological point of view, it may be useful to introduce a temperature dependent respiration rate in the model. In a study on the impact of temperature on $\delta^{13}C_{foram}$ in planktonic foraminifera, Bemis et al. [2000] found that $\delta^{13}C_{foram}$ decreases with increasing temperature. They speculated that this might be caused by increasing respiration rates as the temperature rises, which would confirm results by Hesse et al. [in review]. As shown in Chapter 8, increasing temperature in the FCM results in higher $\delta^{13}C_{foram}$ values and increasing respiration results in lower $\delta^{13}C_{foram}$ values. Therefore, introducing a temperature dependent respiration rate should reduce the strong gradient in $\delta^{13}C_{foram}$ between the surface and the deep ocean.

Chapter 10

Conclusion and Outlook

This chapter is summarising the conclusions of Chapters 7 to 9 and discussing their main implications for the use of $\delta^{13}C_{foram}$ as a proxy for reconstructing water masses in the LGM. Finally, I will give an outlook of where further research could be carried out and what results may be expected in the future.

The model-data comparison in Chapter 7 highlights the role of the Southern Ocean in explaining glacial climate. Its main advance is methodological: the use of a database for $\delta^{13}C$ of more than 200 sediment cores from all over the Atlantic Ocean in combination with a coupled three-dimensional ocean circulation and carbon cycle model. We know from proxy records that the positive AMOC cell in the North Atlantic should have shoaled and the negative AMOC cell in the deep South Atlantic should have expanded [Lynch-Stieglitz et al., 2007]. Since inverse modelling for the LGM has been shown to be insufficiently constrained by proxy data [Huybers et al., 2007; Marchal and Curry, 2008], using different forward modelling scenarios and comparing those to the available proxy data is the best we can do at the moment. Until now, however, models have shown a large spread of possible AMOC states for the LGM [Otto-Bliesner et al., 2007]. With this study, we corroborated the findings of Butzin et al. [2005] by extending the best

model-data agreement for the GLAMAP SST-based model scenario with an altered fresh water balance in the Southern Ocean from radiocarbon to δ^{13}C.

The sensitivity study in Chapter 8 moves on to advance our understanding of the micro-environmental processes involved in forming the δ^{13}C signal in benthic foraminifera. Perhaps surprisingly, this aspect of the δ^{13}C proxy has not received much attention in the past, even though it is of crucial importance for the interpretation of δ^{13}C. This advance is possible by adapting the FCM for planktonic foraminifera developed by Wolf-Gladrow et al. [1999] and Zeebe et al. [1999] for benthic foraminifera. The adaptation involves the inclusion of the pressure dependence of the carbonate species dissociation constants, and a change in the vital parameters of the modelled foraminiferal species. We show that temperature, respiration rate and pH have a significant impact on δ^{13}C in benthic foraminifera, whereas salinity, pressure, $\delta^{13}C_{POC}$, total alkalinity and calcification rate have a limited impact. It was expected that respiration rate has an influence on the δ^{13}C signal. The relatively strong temperature response, however, is surprising. In combined sensitivity experiments, we show that two-thirds of the drop in δ^{13}C from the Holocene to the LGM can be explained by changes in temperature, pH and $\delta^{13}C_{POC}$. Finally, the study allows for the simple prediction of the benthic foraminiferal δ^{13}C value without having to use the FCM, based on the following equation:

$$\delta^{13}C_{foram} = \delta^{13}C_{DIC} + a_1(T - 7°C) - a_2(RR - 0.41 \text{ nmol } CO_2 \text{ h}^{-1}) - a_3(\text{pH} - 7.9), \quad (10.1)$$

where T is temperature in °C, RR is respiration rate in nmol CO_2 h^{-1}, a_1 is 0.045‰ per °C, a_2 is 0.4‰ per nmol CO_2 h^{-1}, and a_3 is 0.08‰. This study advances the overall aim of a more mechanistic understanding of the formation of the δ^{13}C signal in benthic foraminifera.

The third study in Chapter 9 finally combines the FCM (Chapter 5) with the glacial model scenarios from Chapter 7 in order to assess the uncertainties involved in the formation and later interpretation of δ^{13}C on an ocean-wide scale. Several conclusions can be drawn from the study.

Most important for palaeoceanographers is the fact that the glacial model scenario with a shoaled positive meridional overturning in the upper ocean and an expanded negative overturning cell at depth is still the best-fitting scenario in the model-data comparison that includes the FCM. Furthermore, the study highlights that $\delta^{13}C_{foram}$ can deviate substantially from $\delta^{13}C_{DIC}$, depending on temperature, pH, and circulation regime, although a temperature-dependent respiration rate may reduce the modelled deviations. Differences in the LGM-to-present-day anomalies between $\delta^{13}C_{DIC}$ and $\delta^{13}C_{foram}$ are on average approximately 0.10‰ in the deep ocean, with the $\delta^{13}C_{foram}$ anomalies being more negative. Respiration rate uncertainties cause uncertainties in $\delta^{13}C_{foram}$ of $\pm$(0.10 to 0.15)‰.

With this thesis, our overall understanding of $\delta^{13}C$ as a palaeoclimatological proxy has been advanced. We are now a step closer to a fully mechanistic description of $\delta^{13}C$ signal formation and can quantify the effects of processes acting in the micro-environment around a benthic foraminifer. Having said that, the cell-internal processes during shell calcification have so far not been captured quantitatively and the detailed picture of the processes is still fragmentary. Nonetheless, with the help of the FCM our understanding of uncertainties in the formation of $\delta^{13}C$ has improved and can now be taken into consideration when $\delta^{13}C$ signals are interpreted.

Regarding the assessment of the glacial ocean state, the results of the thesis corroborate previous findings of a shoaled positive meridional overturing cell in the upper North Atlantic and an extended negative overturing cell in the deep Atlantic Ocean. From a modeller's perspective it is interesting to note that this Atlantic Ocean circulation regime has been simulated by changes in the freshwater balance in the Southern Ocean (see also Shin et al. [2003b]; Butzin et al. [2005]), rather than the North Atlantic, which has dominantly been the focus for explaining/modelling the LGM ocean. In order to assess the actual transport rates in the ocean $\delta^{13}C$ is of little use. Being a non-conservative tracer, $\delta^{13}C$ only allows for reconstructing the distribution of past water masses. So in order to get a full picture of the glacial AMOC, it is necessary to consider kinematic proxies such as $\Delta^{14}C$, $^{231}Pa/^{230}Th$, or grain size distributions.

By improving the understanding of δ^{13}C, the understanding and interpretation of palaeoclimatological states is also improved. In this thesis with its focus on the LGM it is now possible to explain parts of the observed drop in oceanic δ^{13}C of 0.3 to 0.4‰ when going from the Holocene to the LGM. In the late 1970s Shackleton [1977] first described this shift and attributed it to a transfer of low-δ^{13}C terrestrial carbon to the oceans. This interpretation is still favoured by large parts of the palaeoclimate community, but there are also hints at other possible factors. Lea et al. [1999], building on laboratory studies by Spero et al. [1997] on planktonic foraminifera, argued that a carbonate ion effect also has the potential to lower foraminiferal δ^{13}C. Since the glacial ocean is thought to have been more alkaline [Hönisch and Hemming, 2005], this carbonate ion effect might have contributed to the observed drop in δ^{13}C. It is only with the study in Chapter 8 [Hesse et al., in review], however, that this carbonate ion effect has been modelled for benthic foraminifera. In the model, a small but marked effect on changes in pH is visible (Figure 8.3). More important in the FCM is the effect that temperature has on δ^{13}C: per degree of cooling there is a drop in δ^{13}C of 0.05‰. This effect has not attracted much attention in the past, perhaps because deep-sea temperatures are fairly homogeneous. Changes in deep-sea temperatures such as the average drop of 3.25 ± 0.55°C reported by Clark et al. [2009] for the LGM, however, have a marked effect on benthic foraminiferal δ^{13}C [Hesse et al., in review].

What are the possible lessons learned for the bigger picture? Palaeoclimate studies allow us to develop an understanding of the natural variability of the climate system on different spatial and temporal scales, which is of great interest for predicting possible future climate changes. The thesis highlights that only by considering and combining the many different elements of climate research are we able to reconstruct palaeoclimate in a meaningful way that allows for quantitative assessments of the involved processes. Simply put one might say: modelling needs validation by data reconstructions, data reconstructions need validation by proxy development. The thesis does exactly that. Competing LGM model scenarios are tested against δ^{13}C reconstructions, and uncertainties in these reconstructions are assessed by modelling the small scale processes

acting during proxy signal formation. Admittedly, δ^{13}C is only a small piece of the big jigsaw puzzle that is the climate system. Nonetheless, this kind of approach and the combination of many of these small pieces, should eventually allow us to gain the much desired holistic view and understanding of the climate system.

Outlook

The research presented in this thesis may encourage further investigations in the following areas:

- **Experimental research on benthic foraminifera in the laboratory and in-situ**. For further advances in our understanding of benthic foraminifera it is crucial to know more about their vital effects, their feeding behaviour and, most importantly, the way they build their chambers. In order to do so, detailed measurement efforts are needed. Studies by Chandler et al. [1996], Hintz et al. [2004], Nomaki et al. [2007], de Nooijer et al. [2009], Geslin et al. [2011], or Glas et al. [2012] are pointing in the right direction. With the help of these efforts we should eventually be able to describe the formation of δ^{13}C in benthic foraminiferal shells fully mechanistically.

- **Modelling the biochemical processes inside foraminiferal cells**. This approach should accompany the experimental research described in the previous point. Modelling internal processes should highlight which processes are the most important for chamber formation. These insights could, in turn, be used in measurement studies so that the two approaches can stimulate and benefit from each other. There are only a few studies that attempt to model cell-internal processes, but so far only for algae (e.g. Thoms et al. [2001], or Holtz et al. [2013]).

- **Modelling the carbon cycle with a fully coupled state-of-the-art Earth system model**. The work presented in this thesis is based on comparatively simple three dimensional circulation models (LSG and HAMOCC2s) that have been around for the last 15 to 20 years

already (but have their distinct advantages - see Chapter 5). The latest state-of-the-art Earth system models with their fully coupled climate components (atmosphere, ocean, land ice, sea ice, vegetation, sediments, etc.) would probably create a more realistic distribution of carbon isotopes. The Community Earth System Models (COSMOS) suite would be an ideal candidate, but it does not yet have carbon isotopes implemented in all climate system components. Once that is accomplished, however, coupling such a model to an advanced version of the FCM and, perhaps, to a sediment diagenesis model will bring us yet closer to the overall aim of modelling directly what is found in the deep-sea sediment cores. This, in turn, would allow for more rigorous model-data comparisons, not only of δ^{13}C from sediment cores, but also from other archives such as ice cores [Lourantou et al., 2010]. Additionally, other proxies such as δ^{18}O, radiocarbon, Mg/Ca, Cd/Ca, B/Ca, or alkenones, to mention but a few, could be considered.

- **Multi-proxy approaches to assessing palaeoclimate**. One of the outcomes of this thesis is that relying on one proxy only is insufficient for fully constraining a certain climate state. In my case, δ^{13}C does not fully constrain the glacial AMOC. This is nothing new, but it further highlights the need for multi-proxy approaches in palaeoceanography. In recent years there have been considerable advances in this direction already (e.g. Gersonde et al. [2003]; Kucera et al. [2005]; Waelbroeck et al. [2009]). Looking at all the different proxies available and assessing all their strengths and weaknesses is, of course, a huge task that can only be achieved through major collaborations.

- **Model intercomparison studies**. Relying on one model only is always a danger as different parameterisations may lead to different model results and interpretations. Therefore, it would be welcome to follow up on the Paleoclimate Modelling Intercomparison Project (PMIP) and PMIP2 model intercomparisons [Weber et al., 2007; Otto-Bliesner et al., 2007], which already demonstrate that different models can arrive at very different

glacial ocean circulation patterns. Looking in detail at what causes those differences should eventually lead to a much better understanding of the processes in the climate system and their parameterisations.

- **Transient modelling of glacial-interglacial cycles**. Understanding the LGM is comparatively easy in theory, as it is a well defined climate state, with known boundary conditions, and probably in climatic equilibrium. Modelling the last deglaciation, or indeed whole glacial-interglacial cycles, is a much more difficult task. In recent years, some studies have embarked on this journey (e.g. Ganopolski and Calov [2011]). With increasing computer power these efforts should be an easier task in the future.

- **Model-data comparisons**. Based on all the above points, further model-data comparisons would be desired. These integrated assessments present the most comprehensive approach to describing and understanding climate. As Lohmann [2008] points out, only by considering and analysing both models and data are we fully able to understand forcings, feedback mechanisms, and climate variability. Given the ever increasing amount of proxy data and the efforts to combine them in compilations that are suitable for model-data comparisons (e.g. the MARGO project [Kucera et al., 2005], or Oliver et al. [2010] for δ^{13}C), comparing models and data will be made easier and more meaningful in the future.

- **Extending approach to other time slices**. All of the above points can also be applied to different climate periods, such as the Last Interglacial (or Eemian), other earlier glacials and interglacials, as well as the Pliocene, Miocene and Eocene. For a better understanding of possible future climate states looking at warmer climates from the geological past may bring useful insights. The Pliocene may be a good analogue for a high CO_2 world (e.g. Haywood et al. [2013]), while the Palaeocene-Eocene Thermal Maximum (PETM) may provide important lessons regarding the rapid release of carbon to the atmosphere and ocean, and its subsequent removal from the system (e.g. Panchuk et al. [2008]).

Bibliography

Acha, E. H., M. W. Mianzan, R. A. Guerrero, M. Favero, and J. Bava. Marine fronts at the continental shelves of austral South America physical and ecological processes. *Journal of Marine Systems*, 44(1-2):83–105, 2004. doi: 10.1016/j.jmarsys.2003.09.005.

Adkins, J. F., K. McIntyre, and D. P. Schrag. The salinity, temperature, and δ^{18}O of the glacial deep ocean. *Science*, 298(5599):1769–1773, 2002. doi: 10.1126/science.1076252.

Andersen, K. K., A. Armengaud, and C. Genthon. Atmospheric dust under glacial and interglacial conditions. *Geophysical Research Letters*, 25:2281–2284, 1998. doi: 10.1029/98GL51811.

Anderson, D. M. and R. S. Webb. Paleoclimatology - ice-age tropics revisitied. *Nature*, 367 (6458):23–24, 1994.

Archer, D., M. Lyle, K. B. Rodgers, and P. Froelich. What controls opal preservation in tropical deep-sea sediments? *Paleoceanography*, 8:7–21, 1993. doi: 10.1029/92PA02803.

Arz, H. W., J. Pätzold, and G. Wefer. Correlated millennial-scale changes in surface hydrography and terrigenous sediment yield inferred from last-glacial marine deposits off northeastern Brazil. *Quaternary Research*, 50(2):157–166, 1998. doi: 10.1006/qres.1998.1992.

Bauch, H. A., H. Erlenkeuser, R. F. Spielhagen, U. Struck, J. Matthiessen, J. Thiede, and J. Heinemeier. A multiproxy reconstruction of the evolution of deep and surface waters in

the subarctic Nordic seas over the last 30,000 yr. *Quaternary Science Reviews*, 20(4):659–678, 2001. doi: 10.1016/S0277-3791(00)00098-6.

Beaulieu, S. E. Accumulation and fate of phytodetritus on the sea floor. In R. N. Gibson, M. Barnes, and R. J. A. Atkinson, editors, *Oceanography and Marine Biology, Vol 40*, pages 171–232. Taylor & Francis, 2002.

Belanger, P. E., W. B. Curry, and R. K. Matthews. Core-top evaluation of benthic foraminiferal isotopic ratios for paleo-oceanographic interpretations. *Palaeogeography Palaeoclimatology Palaeoecology*, 33(1-3):205–220, 1981. doi: 10.1016/0031-0182(81)90039-0.

Bemis, B. E., H. J. Spero, D. W. Lea, and J. Bijma. Temperature influence on the carbon isotopic composition of *Globigerina bulloides* and *Orbulina universa* (planktonic foraminifera). *Marine Micropaleontology*, 38(3-4):213–228, 2000. doi: 10.1016/S0377-8398(00)00006-2.

Bertram, C. J., H. Elderfield, N. J. Shackleton, and J. A. Macdonald. Cadmium/calcium and carbon-isotope reconstructions of the glacial northeast Atlantic Ocean. *Paleoceanography*, 10 (3):563–578, 1995. doi: 10.1029/94PA03058.

Beveridge, N. A. S., H. Elderfield, and N. J. Shackleton. Deep thermohaline circulation in the low-latitude Atlantic during the last glacial. *Paleoceanography*, 10(3):643–660, 1995. doi: 10.1029/94PA03353.

Bickert, T. and A. Mackensen. Last Glacial to Holocene changes in South Atlantic deep water circulation. In G. Wefer, S. Mulitza, and V. Ratmeyer, editors, *The South Atlantic in the Late Quaternary: Reconstruction of material budgets and current systems*, pages 671–695. Springer-Verlag, Berlin, 2004.

Bickert, T. and G. Wefer. Late Quaternary deep water circulation in the South Atlantic: Reconstruction from carbonate dissolution and benthic stable isotopes. In G. Wefer, W. H. Berger,

G. Siedler, and D. Webb, editors, *The South Atlantic: Present and Past Circulation*, pages 599–620. Springer-Verlag, Berlin, 1996.

Bickert, T. and G. Wefer. South Atlantic and benthic foraminifer δ^{13}C deviations: implications for reconstructing the Late Quaternary deep-water circulation. *Deep-Sea Research Part II: Topical Studies in Oceanography*, 46(1-2):437–452, 1999. doi: 10.1016/S0967-0645(98)00098-8.

Bijma, J., J. Erez, and C. Hemleben. Lunar and semi-lunar reproductive cycles in some spinose planktonic foraminifers. *Journal of Foraminiferal Research*, 20(2):117–127, 1990.

Bijma, J., C. Hemleben, and K. Wellnitz. Lunar-influenced carbonate flux of the planktic foraminifer *Globigerinoides sacculifer* (Brady) from the central Red Sea. *Deep-Sea Research Part I-Oceanographic Research Papers*, 41(3):511–530, 1994.

Bijma, J., H. J. Spero, and D. W. Lea. Reassessing foraminiferal stable isotope geochemistry: Impact of the oceanic carbonate system (experimental results). In G. Fischer and G. Wefer, editors, *Use of proxies in paleoceanography - Examples from the South Atlantic*, pages 489–512. Springer, Berlin, 1999.

Boyle, E. A. and L. D. Keigwin. Comparison of Atlantic and Pacific paleochemical records for the last 215,000 years - changes in deep ocean circulation and chemical inventories. *Earth and Planetary Science Letters*, 76(1-2):135–150, 1985. doi: 10.1016/0012-821X(85)90154-2.

Boyle, E. A. and L. D. Keigwin. North Atlantic thermohaline circulation during the past 20,000 years linked to high-latitude surface temperature. *Nature*, 330(6143):35–40, 1987. doi: 10.1038/330035a0.

Broecker, W. S. and E. Maier-Reimer. The influence of air and sea exchange on the carbon isotope distribution in the sea. *Global Biogeochem. Cycles*, 6(3):315–320, 1992. doi: 10.1029/92GB01672.

Broecker, W. S. and T. H. Peng. *Tracers in the Sea*. Eldigio Press, New York, 1982. ISBN 096175110X.

Butzin, M., M. Prange, and G. Lohmann. Radiocarbon simulations for the glacial ocean: The effects of wind stress, Southern Ocean sea ice and Heinrich events. *Earth and Planetary Science Letters*, 235(1-2):45–61, 2005. doi: 10.1016/j.epsl.2005.03.003.

Castañeda, I. S., S. Mulitza, E. Schefuss, R. A. L. dos Santos, J. S. S. Damste, and S. Schouten. Wet phases in the Sahara/Sahel region and human migration patterns in North Africa. *Proceedings of the National Academy of Sciences of the United States of America*, 106(48):20159–20163, 2009. doi: 10.1073/pnas.0905771106.

Chandler, G. T., D. F. Williams, H. J. Spero, and X. D. Gao. Sediment microhabitat effects on carbon stable isotopic signatures of microcosm-cultured benthic foraminifera. *Limnology and Oceanography*, 41(4):680–688, 1996.

Clark, P. U., A. S. Dyke, J. D. Shakun, A. E. Carlson, J. Clark, B. Wohlfarth, J. X. Mitrovica, S. W. Hostetler, and A. M. McCabe. The Last Glacial Maximum. *Science*, 325(5941):710–714, 2009. doi: 10.1126/science.1172873.

CLIMAP Project Members. The surface of the ice-age Earth. *Science*, 191:1131–1137, 1976.

CLIMAP Project Members. Seasonal reconstruction of the Earth's surface at the Last Glacial Maximum. *Geological Society of America Map Chart Series*, MC-36, 1981.

Culver, S. J. Early Cambrian foraminifera from West Africa. *Science*, 254(5032):689–691, 1991.

Curry, W. B. and G. P. Lohmann. Carbon isotopic changes in benthic foraminifera from the western South Atlantic - reconstruction of glacial abyssal circulation patterns. *Quaternary Research*, 18(2):218–235, 1982. doi: 10.1016/0033-5894(82)90071-0.

Curry, W. B. and D. W. Oppo. Glacial water mass geometry and the distribution of δ^{13}C of ΣCO_2 in the western Atlantic Ocean. *Paleoceanography*, 20(1), 2005. doi: 10.1029/2004PA001021.

Curry, W. B., J. C. Duplessy, L. D. Labeyrie, and N. J. Shackleton. Changes in the distribution of δ^{13}C of deep water ΣCO_2 between the last glaciation and the Holocene. *Paleoceanography*, 3 (3):317–341, 1988. doi: 10.1029/PA003i003p00317.

de Nooijer, L. J., T. Toyofuku, and H. Kitazato. Foraminifera promote calcification by elevating their intracellular pH. *Proceedings of the National Academy of Sciences of the United States of America*, 106(36):15374–15378, 2009. doi: 10.1073/pnas.0904306106.

deMenocal, P. B., D. W. Oppo, R. G. Fairbanks, and W. L. Prell. Pleistocene δ^{13}C Variability of North Atlantic Intermediate Water. *Paleoceanography*, 7(2):229–250, 1992. doi: 10.1029/92PA00420.

Duplessy, J. C. North Atlantic deep water circulation during the last climatic cycle. *Bull. Inst. Geol. Bassin d'Aquitaine*, 31:379–391, 1982.

Duplessy, J. C., N. J. Shackleton, R. K. Matthews, W. Prell, W. F. Ruddiman, M. Caralp, and C. H. Hendy. ^{13}C record of benthic foraminifera in the last interglacial ocean - implications for the carbon cycle and the global deep-water circulation. *Quaternary Research*, 21(2):225–243, 1984.

Duplessy, J. C., N. J. Shackleton, R. G. Fairbanks, L. Labeyrie, D. W. Oppo, and N. Kallel. Deep-water source variations during the last climatic cycle and their impact on the global deepwater circulation. *Paleoceanography*, 3(3):343–360, 1988. doi: 10.1029/PA003i003p00343.

England, M. H. and E. Maier-Reimer. Using chemical tracers to assess ocean models. *Reviews of Geophysics*, 39(1):29–70, 2001.

Erez, J. The source of ions for biomineralization in foraminifera and their implications for paleoceanographic proxies. *Reviews in Mineralogy and Geochemistry*, 54:115–149, 2003.

Fairbanks, R. G. A 17,000-year glacio-eustatic sea-level record - influence of glacial melting rates on the Younger Dryas event and deep ocean circulation. *Nature*, 342(6250):637–642, 1989. doi: 10.1038/342637a0.

Fichefet, T., S. Hovine, and J. C. Duplessy. A model study of the Atlantic thermohaline circulation during the Last Glacial Maximum. *Nature*, 372(6503):252–255, 1994. doi: 10.1038/372252a0.

Freudenthal, T., H. Meggers, J. Henderiks, H. Kuhlmann, A. Moreno, and G. Wefer. Upwelling intensity and filament activity off Morocco during the last 250,000 years. *Deep-Sea Research Part II: Topical Studies in Oceanography*, 49(17):3655–3674, 2002. doi: 10.1016/S0967-0645(02)00101-7.

Ganopolski, A. and R. Calov. The role of orbital forcing, carbon dioxide and regolith in 100 kyr glacial cycles. *Climate of the Past*, 7(4):1415–1425, 2011. doi: 10.5194/cp-7-1415-2011.

Garabato, A. C. N., K. L. Polzin, B. A. King, K. J. Heywood, and M. Visbeck. Widespread intense turbulent mixing in the Southern Ocean. *Science*, 303(5655):210–213, 2004.

Gersonde, R., A. Abelmann, U. Brathauer, S. Becquey, C. Bianchi, G. Cortese, H. Grobe, G. Kuhn, H. S. Niebler, M. Segl, R. Sieger, U. Zielinski, and D. K. Futterer. Last glacial sea surface temperatures and sea-ice extent in the Southern Ocean (Atlantic-Indian sector): A multiproxy approach. *Paleoceanography*, 18(3), 2003. doi: 10.1029/2002PA000809.

Gersonde, R., X. Crosta, A. Abelmann, and L. Armand. Sea-surface temperature and sea ice distribution of the Southern Ocean at the EPILOG Last Glacial Maximum - a circum-Antarctic view based on siliceous microfossil records. *Quaternary Science Reviews*, 24(7-9):869–896, 2005. doi: 10.1016/j.quascirev.2004.07.015.

Geslin, E., N. Risgaard-Petersen, F. Lombard, E. Metzger, D. Langlet, and F. Jorissen. Oxygen respiration rates of benthic foraminifera as measured with oxygen microsensors. *Journal of Experimental Marine Biology and Ecology*, 396(2):108–114, 2011.

Glas, M. S., G. Langer, and N. Keul. Calcification acidifies the microenvironment of a benthic foraminifer (*Ammonia* sp.). *Journal of Experimental Marine Biology and Ecology*, 424:53–58, 2012.

Goericke, R. and B. Fry. Variations of marine plankton δ^{13}C with latitude, temperature, and dissolved CO_2 in the world ocean. *Global Biogeochemical Cycles*, 8(1):85–90, 1994.

Gooday, A. J., C. M. Turley, and J. A. Allen. Responses by benthic organisms to inputs of organic material to the ocean-floor - a review. *Philosophical Transactions of the Royal Society of London Series a-Mathematical Physical and Engineering Sciences*, 331(1616):119–138, 1990.

Guilderson, T. P., R. G. Fairbanks, and J. L. Rubenstone. Tropical temperature variations since 20,000 years ago - modulating interhemispheric climate change. *Science*, 263(5147):663–665, 1994.

Hall, I. R., H. K. Evans, and D. J. R. Thornalley. Deep water flow speed and surface ocean changes in the subtropical North Atlantic during the last deglaciation. *Global Planet. Change*, 2011. doi: 10.1016/j.gloplacha.2010.12.001.

Hannah, F., A. Rogerson, and J. Laybournparry. Respiration rates and biovolumes of common benthic foraminifera (Protozoa). *Journal of the Marine Biological Association of the United Kingdom*, 74(2):301–312, 1994.

Havach, S. M., G. T. Chandler, A. Wilson-Finelli, and T. J. Shaw. Experimental determination of trace element partition coefficients in cultured benthic foraminifera. *Geochimica Et Cosmochimica Acta*, 65(8):1277–1283, 2001.

Haywood, A. M., D. J. Hill, A. M. Dolan, B. L. Otto-Bliesner, F. Bragg, W.-L. Chan, M. A. Chandler, C. Contoux, H. J. Dowsett, A. Jost, Y. Kamae, G. Lohmann, D. J. Lunt, A. Abe-Ouchi, S. J. Pickering, G. Ramstein, N. A. Rosenbloom, U. Salzmann, L. Sohl, C. Stepanek, H. Ueda, Q. Yan, and Z. Zhang. Large-scale features of Pliocene climate: results from the Pliocene Model Intercomparison Project. *Climate of the Past*, 9(1):191–209, 2013. doi: 10.5194/cp-9-191-2013.

Heinze, C. and E. Maier-Reimer. The Hamburg Oceanic Carbon Cycle Model Version "HAMOCC2s" for long time integrations. Technical Report 20, Max-Planck-Institut für Meteorologie, Hamburg, 1999.

Heinze, C., E. Maier-Reimer, A. M. E. Winguth, and D. Archer. A global oceanic sediment model for long-term climate studies. *Global Biogeochemical Cycles*, 13(1):221–250, 1999. doi: 10.1029/98GB02812.

Hemleben, C. and H. Kitazato. Deep-sea foraminifera under long-time observation in the laboratory. *Deep-Sea Research Part I-Oceanographic Research Papers*, 42(6):827–832, 1995.

Hesse, T., M. Butzin, T. Bickert, and G. Lohmann. A model-data comparison of δ^{13}C in the glacial Atlantic Ocean. *Paleoceanography*, 26(PA3220), 2011.

Hesse, T., G. Lohmann, M. Butzin, R. E. Zeebe, and D. Wolf-Gladrow. Towards a mechanistic interpretation of δ^{13}C: modelling calcification in benthic foraminifera and its application to palaeoceanographic model scenarios. *Climate of the Past*, in preparation.

Hesse, T., D. Wolf-Gladrow, G. Lohmann, J. Bijma, A. Mackensen, and R. E. Zeebe. Modelling δ^{13}C in benthic foraminifera: insights from model sensitivity experiments. *Marine Micropaleontology*, in review.

Hewitt, C. D., R. J. Stouffer, A. J. Broccoli, J. F. B. Mitchell, and P. J. Valdes. The effect of ocean

dynamics in a coupled GCM simulation of the Last Glacial Maximum. *Climate Dynamics*, 20 (2-3):203–218, 2003. doi: 10.1007/s00382-002-0272-6.

Hill, T. M., J. P. Kennett, and D. L. Valentine. Isotopic evidence for the incorporation of methane-derived carbon into foraminifera from modern methane seeps, Hydrate Ridge, Northeast Pacific. *Geochimica Et Cosmochimica Acta*, 68(22):4619–4627, 2004.

Hinrichs, K. U. A molecular recorder of methane hydrate destabilization. *Geochemistry Geophysics Geosystems*, 2:art. no.–2000GC000118, 2001.

Hintz, C. J., G. T. Chandler, J. M. Bernhard, D. C. McCorkle, S. M. Havach, J. K. Blanks, and T. J. Shaw. A physicochemically constrained seawater culturing system for production of benthic foraminifera. *Limnology and Oceanography-Methods*, 2:160–170, 2004.

Hodell, D. A., J. H. Curtis, F. J. Sierro, and M. E. Raymo. Correlation of late Miocene to early Pliocene sequences between the Mediterranean and North Atlantic. *Paleoceanography*, 16(2): 164–178, 2001. doi: 10.1029/1999PA000487.

Hodell, D. A., K. A. Venz, C. D. Charles, and U. S. Ninnemann. Pleistocene vertical carbon isotope and carbonate gradients in the South Atlantic sector of the Southern Ocean. *Geochemistry Geophysics Geosystems*, 4(1), 2003. doi: 10.1029/2002GC000367.

Hofmann, M., D. A. Wolf-Gladrow, T. Takahashi, S. C. Sutherland, K. D. Six, and E. Maier-Reimer. Stable carbon isotope distribution of particulate organic matter in the ocean: a model study. *Marine Chemistry*, 72(2-4):131–150, 2000.

Holtz, L.-M., S. Thoms, G. Langer, and D. A. Wolf-Gladrow. Substrate supply for calcite precipitation in *Emiliania huxleyi*: Assessment of different model approaches. *Journal of Phycology*, 49(2):417–426, 2013. doi: 10.1111/jpy.12052.

Hönisch, B. and N. G. Hemming. Surface ocean pH response to variations in pCO_2 through two full glacial cycles. *Earth and Planetary Science Letters*, 236(1-2):305–314, 2005.

Hönisch, B., T. Bickert, and N. G. Hemming. Modern and Pleistocene boron isotope composition of the benthic foraminifer *Cibicidoides wuellerstorfi*. *Earth and Planetary Science Letters*, 272 (1-2):309–318, 2008. doi: 10.1016/j.epsl.2008.04.047.

Huybers, P., G. Gebbie, and O. Marchal. Can paleoceanographic tracers constrain meridional circulation rates? *Journal of Physical Oceanography*, 37(2):394–407, 2007.

IPCC. *Climate change. The IPCC scientific assessment*. J. T. Houghton, G. J. Jenkins, and J. J. Ephraums, editors. Cambridge University Press, 1990.

IPCC. *Climate Change 2007: The physical science basis. Contribution of Working Group I to the Fourth Assessment Report of the Intergovernmental Panel on Climate Change*. S. Solomon, D. Qin, M. Manning, Z. Chen, M. Marquis, K. B. Averyt, M. Tignor, and H. L. Miller, editors. Cambridge University Press, 2007.

Jung, S. J. A. *Wassermassenaustausch zwischen NE-Atlantik und Nordmeer während der letzten 300,000/80,000 Jahre im Abbild stabiler O- und C-Isotope*. PhD thesis, University of Kiel, Germany, 1996.

Kageyama, M., J. Mignot, D. Swingedouw, C. Marzin, R. Alkama, and O. Marti. Glacial climate sensitivity to different states of the Atlantic Meridional Overturning Circulation: results from the IPSL model. *Climate of the Past*, 5(3):551–570, 2009. doi: 10.5194/cp-5-551-2009.

Keigwin, L. D. Radiocarbon and stable isotope constraints on Last Glacial Maximum and Younger Dryas ventilation in the western North Atlantic. *Paleoceanography*, 19(4):15, 2004. doi: 10.1029/2004PA001029.

Keigwin, L. D. and M. A. Schlegel. Ocean ventilation and sedimentation since the glacial maximum at 3 km in the western North Atlantic. *Geochemistry Geophysics Geosystems*, 3(6), 2002. doi: 10.1029/2001GC000283.

Key, R. M., A. Kozyr, C. L. Sabine, K. Lee, R. Wanninkhof, J. L. Bullister, R. A. Feely, F. J. Millero, C. Mordy, and T. H. Peng. A global ocean carbon climatology: Results from Global Data Analysis Project (GLODAP). *Global Biogeochemical Cycles*, 18(4), 2004. doi: 10.1029/2004GB002247.

Kroopnick, P. M. The distribution of ^{13}C of ΣCO_2 in the world oceans. *Deep-Sea Research Part a-Oceanographic Research Papers*, 32(1):57–84, 1985. doi: 10.1016/0198-0149(85)90017-2.

Kucera, M., A. Rosell-Mele, R. Schneider, C. Waelbroeck, and M. Weinelt. Multiproxy approach for the reconstruction of the glacial ocean surface (MARGO). *Quaternary Science Reviews*, 24(7-9):813–819, 2005.

Lea, D. W., J. Bijma, H. J. Spero, and D. Archer. Implications of a carbonate ion effect in shell carbon and oxygen isotopes for glacial ocean conditions. In G. Fischer and G. Wefer, editors, *Use of Proxies in Paleoceanography: Examples from the South Atlantic*, pages 513–522. Springer, Berlin, 1999.

Ledbetter, M. T. and D. A. Johnson. Increased transport of Antarctic Bottom Water in Vema Channel during the Last Ice Age. *Science*, 194(4267):837–839, 1976.

Linke, P. and G. F. Lutze. Microhabitat preferences of benthic foraminifera - a static concept or a dynamic adaptation to optimze food acquisition. *Marine Micropaleontology*, 20(3-4): 215–234, 1993.

Lohmann, G. The influence of a near-bottom transport parameterization on the sensitivity of the thermohaline circulation. *Journal of Physical Oceanography*, 28(10):2095–2103, 1998.

Lohmann, G. Linking data and models. *PAGES News*, 16(2):4–5, 2008.

Lohmann, G. and S. Lorenz. On the hydrological cycle under paleoclimatic conditions as derived from AGCM simulations. *Journal of Geophysical Research-Atmospheres*, 105(D13):17417–17436, 2000. doi: 10.1029/2000JD900189.

Lohmann, G. and M. Schulz. Reconciling Bølling warmth with peak deglacial meltwater discharge. *Paleoceanography*, 15(5):537–540, 2000. doi: 10.1029/1999PA000471.

Lourantou, A., J. V. Lavric, P. Köhler, J. M. Barnola, D. Paillard, E. Michel, D. Raynaud, and J. Chappellaz. Constraint of the CO_2 rise by new atmospheric carbon isotopic measurements during the last deglaciation. *Global Biogeochemical Cycles*, 24:15, 2010.

Lutze, G. F. and H. Thiel. Epibenthic foraminifera from elevated microhabitats - *Cibicidoides wuellerstorfi* and *Planulina ariminensis*. *Journal of Foraminiferal Research*, 19(2):153–158, 1989. doi: 10.2113/gsjfr.19.2.153.

Lynch-Stieglitz, J., T. F. Stocker, W. S. Broecker, and R. G. Fairbanks. The influence of air-sea exchange on the isotopic composition of oceanic carbon - observations and modeling. *Global Biogeochemical Cycles*, 9(4):653–665, 1995. doi: 10.1029/95GB02574.

Lynch-Stieglitz, J., W. B. Curry, D. W. Oppo, U. S. Ninnemann, C. D. Charles, and J. Munson. Meridional overturning circulation in the South Atlantic at the Last Glacial Maximum. *Geochemistry Geophysics Geosystems*, 7(10), 2006. doi: 10.1029/2005GC001226.

Lynch-Stieglitz, J., J. F. Adkins, W. B. Curry, T. Dokken, I. R. Hall, J. C. Herguera, J. J. M. Hirschi, E. V. Ivanova, C. Kissel, O. Marchal, T. M. Marchitto, I. N. McCave, J. F. McManus, S. Mulitza, U. S. Ninnemann, F. Peeters, E. F. Yu, and R. Zahn. Atlantic meridional overturning circulation during the Last Glacial Maximum. *Science*, 316(5821):66–69, 2007. doi: 10.1126/science.1137127.

Mackensen, A. On the use of benthic foraminiferal δ^{13}C in palaeoceanography: constraints from primary proxy relationships. In W. E. N. Austin and R. H. James, editors, *Biogeochemical controls on palaeoceanographic environmental proxies*, volume 303, pages 121–133. Geological Society, London, 2008. doi: 10.1144/SP303.9.

Mackensen, A., H. W. Hubberten, T. Bickert, G. Fischer, and D. K. Futterer. The δ^{13}C in benthic foraminiferal tests of *Fontbotia wuellerstorfi* (Schwager) relative to the δ^{13}C of dissolved inorganic carbon in Southern Ocean deep-water - implications for glacial ocean circulation models. *Paleoceanography*, 8(5):587–610, 1993. doi: 10.1029/93PA01291.

Mackensen, A., H. Grobe, H. W. Hubberten, and G. Kuhn. Benthic foraminiferal assemblages and the δ^{13}C signal in the Atlantic sector of the Southern Ocean: Glacial-to-interglacial contrasts. In R. Zahn, T. F. Pedersen, M. A. Kaminski, and L. Labeyrie, editors, *Carbon Cycling in the Glacial Ocean: Constraints on the Ocean's Role in Global Change*, volume 17 of *NATO ASI Series I*, pages 105–144. Springer-Verlag, New York, 1994.

Mackensen, A., H. W. Hubberten, N. Scheele, and R. Schlitzer. Decoupling of $\delta^{13}C_{\Sigma CO_2}$ and phosphate in recent Weddell Sea deep and bottom water: Implications for glacial southern ocean paleoceanography. *Paleoceanography*, 11(2):203–215, 1996. doi: 10.1029/95PA03840.

Mackensen, A., M. Rudolph, and G. Kuhn. Late Pleistocene deep-water circulation in the subantarctic eastern Atlantic. *Global and Planetary Change*, 30(3-4):197–229, 2001.

Mackensen, A., J. Wollenburg, and L. Licari. Low δ^{13}C in tests of live epibenthic and endobenthic foraminifera at a site of active methane seepage. *Paleoceanography*, 21(2), 2006. doi: 10.1029/2005PA001196.

Maier-Reimer, E., U. Mikolajewicz, and K. Hasselmann. Mean circulation of the Hamburg LSG OGCM and its sensitivity to the thermohaline surface forcing. *Journal of Physical Oceanography*, 23(4):731–757, 1993.

Marchal, O. and W. B. Curry. On the abyssal circulation in the glacial Atlantic. *Journal of Physical Oceanography*, 38(9):2014–2037, 2008. doi: 10.1175/2008JPO3895.1.

Matthies, M., T. Bickert, and A. Paul. Last glacial δ^{13}C distribution and deep-sea circulation in the Atlantic Ocean: A model - data comparison. In G. Wefer, S. Mulitza, and V. Ratmeyer, editors, *The South Atlantic in the Late Quaternary: Reconstruction of material budgets and current systems*, pages 695–722. Springer-Verlag, Berlin, 2004.

McManus, J. F., D. W. Oppo, and J. L. Cullen. A 0.5-million-year record of millennial-scale climate variability in the North Atlantic. *Science*, 283(5404):971–975, 1999. doi: 10.1126/science.283.5404.971.

Meissner, K. J., A. Schmittner, A. J. Weaver, and J. F. Adkins. Ventilation of the North Atlantic Ocean during the Last Glacial Maximum: A comparison between simulated and observed radiocarbon ages. *Paleoceanography*, 18(2), 2003. doi: 10.1029/2002PA000762.

Michaels, A. F., D. A. Caron, N. R. Swanberg, F. A. Howse, and C. M. Michaels. Planktonic sarcodines (Acantharia, radiolaria, foraminifera) in surface waters near Bermuda - abundance, biomass and vertical flux. *Journal of Plankton Research*, 17(1):131–163, 1995.

Millero, F. J. Thermodynamics of the carbon dioxode system in the oceans. *Geochimica Et Cosmochimica Acta*, 59(4):661–677, 1995.

Millo, C., M. Sarnthein, A. Voelker, and H. Erlenkeuser. Variability of the Denmark Strait Overflow during the Last Glacial Maximum. *Boreas*, 35(1):50–60, 2006. doi: 10.1080/03009480500359244.

Mix, A. C. and R. G. Fairbanks. North-Atlantic surface-ocean control of Pleistocene deep-ocean circulation. *Earth and Planetary Science Letters*, 73(2-4):231–243, 1985. doi: 10.1016/0012-821X(85)90072-X.

Mix, A. C., A. E. Morey, N. G. Pisias, and S. W. Hostetler. Foraminiferal faunal estimates of paleotemperature: Circumventing the no-analog problem yields cool ice age tropics. *Paleoceanography*, 14(3):350–359, 1999.

Mix, A. C., E. Bard, and R. Schneider. Environmental processes of the ice age: land, oceans, glaciers (EPILOG). *Quaternary Science Reviews*, 20(4):627–657, 2001. doi: 10.1016/S0277-3791(00)00145-1.

Mollenhauer, G., R. R. Schneider, P. J. Muller, V. Spiess, and G. Wefer. Glacial/interglacial variablity in the Benguela upwelling system: Spatial distribution and budgets of organic carbon accumulation. *Global Biogeochemical Cycles*, 16(4), 2002. doi: 10.1029/2001GB001488.

Moodley, L., J. J. Middelburg, H. T. S. Boschker, G. C. A. Duineveld, R. Pel, P. M. J. Herman, and C. H. R. Heip. Bacteria and Foraminifera: key players in a short-term deep-sea benthic response to phytodetritus. *Marine Ecology-Progress Series*, 236:23–29, 2002.

Mook, W. G. ^{13}C in atmospheric CO_2. *Netherlands Journal of Sea Research*, 20(2-3):211–223, 1986.

Mulitza, S., M. Prange, J. B. Stuut, M. Zabel, T. von Dobeneck, A. C. Itambi, J. Nizou, M. Schulz, and G. Wefer. Sahel megadroughts triggered by glacial slowdowns of Atlantic meridional overturning. *Paleoceanography*, 23(4), 2008. doi: 10.1029/2008PA001637.

Murray, J. W. *Ecology and application of benthic foraminifera*. Cambridge University Press, Cambridge, 2006.

Negre, C., R. Zahn, A. L. Thomas, P. Masque, G. M. Henderson, G. Martinez-Mendez, I. R. Hall, and J. L. Mas. Reversed flow of Atlantic deep water during the Last Glacial Maximum. *Nature*, 468(7320):84–88, 2010. doi: 10.1038/nature09508.

Ninnemann, U. S. and C. D. Charles. Changes in the mode of Southern Ocean circulation over the last glacial cycle revealed by foraminiferal stable isotopic variability. *Earth Planet. Sci. Lett.*, 201(2):383–396, 2002. doi: 10.1016/S0012-821X(02)00708-2.

Nomaki, H., A. Yamaoka, Y. Shirayama, and H. Kitazato. Deep-sea benthic foraminiferal respiration rates measured under laboratory conditions. *Journal of Foraminiferal Research*, 37(4): 281–286, 2007.

Oliver, K. I. C., B. A. A. Hoogakker, S. Crowhurst, G. M. Henderson, R. E. M. Rickaby, N. R. Edwards, and H. Elderfield. A synthesis of marine sediment core δ^{13}C data over the last 150,000 years. *Clim. Past*, 6(5):645–673, 2010. doi: 10.5194/cp-6-645-2010.

Olsen, A. and U. Ninnemann. Large δ^{13}C gradients in the preindustrial North Atlantic revealed. *Science*, 330(6004):658–659, 2010. doi: 10.1126/science.1193769.

Oppo, D. W. and R. G. Fairbanks. Variability in the deep and intermediate water circulation of the Atlantic Ocean during the past 25,000 years - Northern Hemisphere modulation of the Southern Ocean. *Earth and Planetary Science Letters*, 86(1):1–15, 1987. doi: 10.1016/0012-821X(87)90183-X.

Oppo, D. W. and M. Horowitz. Glacial deep water geometry: South Atlantic benthic foraminiferal Cd/Ca and δ^{13}C evidence. *Paleoceanography*, 15(2):147–160, 2000. doi: 10.1029/1999PA000436.

Oppo, D. W. and S. J. Lehman. Mid-depth circulation of the subpolar North Atlantic during the Last Glacial Maximum. *Science*, 259(5098):1148–1152, 1993. doi: 10.1126/science.259.5098.1148.

Oppo, D. W., M. Horowitz, and S. J. Lehman. Marine core evidence for reduced deep water production during Termination II followed by a relatively stable substage 5e (Eemian). *Paleoceanography*, 12(1):51–63, 1997. doi: 10.1029/96PA03133.

Oppo, D. W., J. F. McManus, and J. L. Cullen. Deepwater variability in the Holocene epoch. *Nature*, 423(6938):400–400, 2003. doi: 10.1038/422277b.

Otto-Bliesner, B. L. and E. C. Brady. The sensitivity of the climate response to the magnitude and location of freshwater forcing: last glacial maximum experiments. *Quaternary Science Reviews*, 29(1-2):56–73, 2010. doi: 10.1016/j.quascirev.2009.07.004.

Otto-Bliesner, B. L., C. D. Hewitt, T. M. Marchitto, E. Brady, A. Abe-Ouchi, M. Crucifix, S. Murakami, and S. L. Weber. Last Glacial Maximum ocean thermohaline circulation: PMIP2 model intercomparisons and data constraints. *Geophysical Research Letters*, 34(12), 2007. doi: 10.1029/2007GL029475.

Panchuk, K., A. Ridgwell, and L. R. Kump. Sedimentary response to Paleocene-Eocene Thermal Maximum carbon release: A model-data comparison. *Geology*, 36(4):315–318, 2008.

Paul, A. and C. Schäfer-Neth. Modeling the water masses of the Atlantic Ocean at the Last Glacial Maximum. *Paleoceanography*, 18(3), 2003. doi: 10.1029/2002PA000783.

Pierre, C., J. F. Saliege, M. J. Urrutiaguer, and J. Giraudeau. Stable isotope record of the last 500 k.y. at Site 1087 (Southern Cape Basin). In G. Wefer, W. H. Berger, and C. Richter, editors, *Proceedings of the Ocean Drilling Program*, volume 175 of *Scientific Results*, 2001.

Prange, M., G. Lohmann, and A. Paul. Influence of vertical mixing on the thermohaline hysteresis: Analyses of an OGCM. *Journal of Physical Oceanography*, 33:1707–1721, 2003.

Prange, M., G. Lohmann, V. Romanova, and M. Butzin. Modelling tempo-spatial signatures of Heinrich Events: influence of the climatic background state. *Quaternary Science Reviews*, 23: 521–527, 2004. doi: 10.1016/j.quascirev.2003.11.004.

Rae, J. W. B., G. L. Foster, D. N. Schmidt, and T. Elliott. Boron isotopes and B/Ca in benthic

foraminifera: Proxies for the deep ocean carbonate system. *Earth Planet. Sci. Lett.*, 302(3-4): 403–413, 2011. doi: 10.1016/j.epsl.2010.12.034.

Rahmstorf, S. and J. Willebrand. The role of temperature feedback in stabilizing the thermohaline circulation. *Journal of Physical Oceanography*, 25(5):787–805, 1995.

Rau, G. H., T. Takahashi, and D. J. D. Marais. Latitudinal variations in plankton δ^{13}C - implications for CO_2 and productivity in past oceans. *Nature*, 341(6242):516–518, 1989.

Robinson, L. F., J. F. Adkins, L. D. Keigwin, J. Southon, D. P. Fernandez, S. L. Wang, and D. S. Scheirer. Radiocarbon variability in the western North Atlantic during the last deglaciation. *Science*, 310(5753):1469–1473, 2005. doi: 10.1126/science.1114832.

Roche, D. M., T. M. Dokken, H. Goosse, H. Renssen, and S. L. Weber. Climate of the Last Glacial Maximum: sensitivity studies and model-data comparison with the LOVECLIM coupled model. *Climate of the Past*, 3(2):205–224, 2007. doi: 10.5194/cp-3-205-2007.

Romanova, V., M. Prange, and G. Lohmann. Stability of the glacial thermohaline circulation and its dependence on the background hydrological cycle. *Climate Dynamics*, 22(5):527–538, 2004. doi: 10.1007/s00382-004-0395-z.

Sabine, C. L., R. M. Key, A. Kozyr, R. A. Feely, R. Wanninkhof, F. J. Millero, T. H. Peng, J. L. Bullister, and L. Kitack. Global Ocean Data Analysis Project (GLODAP): Results and Data. Technical Report ORNL/CDIAC-145, NDP-083, Carbon Dioxide Information Analysis Center, Oak Ridge National Laboratory, Oak Ridge, Tennessee, United States, 2005.

Sanyal, A., N. G. Hemming, W. S. Broecker, and G. N. Hanson. Changes in pH in the eastern equatorial Pacific across stage 5-6 boundary based on boron isotopes in foraminifera. *Global Biogeochemical Cycles*, 11(1):125–133, 1997.

Sarnthein, M., K. Winn, S. J. A. Jung, J. C. Duplessy, L. Labeyrie, H. Erlenkeuser, and G. Ganssen. Changes in east Atlantic deep-water circulation over the last 30,000 years: Eight time slice reconstructions. *Paleoceanography*, 9(2):209–267, 1994. doi: 10.1029/93PA03301.

Sarnthein, M., R. Gersonde, S. Niebler, U. Pflaumann, R. Spielhagen, J. Thiede, G. Wefer, and M. Weinelt. Overview of Glacial Atlantic Ocean Mapping (GLAMAP 2000). *Paleoceanography*, 18(2):6, 2003. doi: 10.1029/2002PA000769.

Schäfer-Neth, C. and A. Paul. Circulation of the glacial Atlantic: A synthesis of global and regional modeling. In P. Schäfer, W. Ritzrau, M. Schlüter, and J. Thiede, editors, *The northern North Atlantic: A changing environment*, pages 441–462. Springer-Verlag, Berlin, 2001.

Schmittner, A. Southern Ocean sea ice and radiocarbon ages of glacial bottom waters. *Earth and Planetary Science Letters*, 213(1-2):53–62, 2003. doi: 10.1016/S0012-821X(03)00291-7.

Schmitz, W. J. The Pacific and Indian Oceans / A global update. Technical report, Woods Hole Oceanographic Institution, 1996.

Schönfeld, J., R. Zahn, and L. de Abreu. Surface and deep water response to rapid climate changes at the Western Iberian Margin. *Global and Planetary Change*, 36(4):237–264, 2003. doi: 10.1016/S0921-8181(02)00197-2.

Seidov, D., E. Barron, and B. J. Haupt. Meltwater and the global ocean conveyor: northern versus southern connections. *Global and Planetary Change*, 30(3-4):257–270, 2001. doi: 10.1016/S0921-8181(00)00087-4.

Shackleton, N. J. Tropical rainforest history and the equatorial Pacific carbonate dissolution cycles. In N. R. Malahoff and A. Andersen, editors, *Fate of fossil fuel CO_2 in the oceans*, pages 401–427. Plenum Press, New York, 1977.

Shin, S. I., Z. Liu, B. L. Otto-Bliesner, E. C. Brady, J. E. Kutzbach, and S. P. Harrison. A simulation of the Last Glacial Maximum climate using the NCAR-CCSM. *Climate Dynamics*, 20(2-3):127–151, 2003a. doi: 10.1007/s00382-002-0260-x.

Shin, S. I., Z. G. Liu, B. L. Otto-Bliesner, J. E. Kutzbach, and S. J. Vavrus. Southern Ocean sea-ice control of the glacial North Atlantic thermohaline circulation. *Geophysical Research Letters*, 30(2), 2003b. doi: 10.1029/2002GL015513.

Sigman, D. M. and E. A. Boyle. Glacial/interglacial variations in atmospheric carbon dioxide. *Nature*, 407(6806):859–869, 2000.

Skinner, L. C. and N. J. Shackleton. Rapid transient changes in northeast Atlantic deep water ventilation age across Termination I. *Paleoceanography*, 19(2), 2004. doi: 10.1029/2003PA000983.

Slowey, N. C. and W. B. Curry. Glacial-interglacial differences in circulation and carbon cycling within the upper western North Atlantic. *Paleoceanography*, 10(4):715–732, 1995. doi: 10.1029/95PA01166.

Spero, H. J. and D. W. Lea. Experimental determination of stable isotope variability in *Globigerina bulloides*: Implications for paleoceanographic reconstructions. *Marine Micropaleontology*, 28(3-4):231–246, 1996. doi: 10.1016/0377-8398(96)00003-5.

Spero, H. J., J. Bijma, D. W. Lea, and B. E. Bemis. Effect of seawater carbonate concentration on foraminiferal carbon and oxygen isotopes. *Nature*, 390(6659):497–500, 1997. doi: 10.1038/37333.

Stocker, T. F., D. G. Wright, and W. S. Broecker. The influence of high-latitude surface forcing on the global thermohaline circulation. *Paleoceanography*, 7(5):529–541, 1992. doi: 10.1029/92PA01695.

Tagliabue, A., L. Bopp, D. M. Roche, N. Bouttes, J. C. Dutay, R. Alkama, M. Kageyama, E. Michel, and D. Paillard. Quantifying the roles of ocean circulation and biogeochemistry in governing ocean carbon-13 and atmospheric carbon dioxide at the Last Glacial Maximum. *Climate of the Past*, 5(4):695–706, 2009. doi: 10.5194/cp-5-695-2009.

Taylor, K. E.. Summarizing multiple aspects of model performance in a single diagram. *Journal of Geophysical Research-Atmospheres*, 106(D7):7183–7192, 2001. doi: 10.1029/2000JD900719.

Thoms, S., M. Pahlow, and D. A. Wolf-Gladrow. Model of the carbon concentrating mechanism in chloroplasts of eukaryotic algae. *Journal of theoretical Biology*, 208:295–313, 2001.

Tiedemann, R. *Climatic history of northwest Africa during the last 8 million years and paleoceanography of the adjacent Atlantic*. PhD thesis, University of Kiel, Germany, 1991.

Tjallingii, R., M. Claussen, J. B. W. Stuut, J. Fohlmeister, A. Jahn, T. Bickert, F. Lamy, and U. Röhl. Coherent high- and low-latitude control of the northwest African hydrological balance. *Nature Geoscience*, 1(10):670–675, 2008. doi: 10.1038/ngeo289.

Turley, C. M., R. C. Newell, and D. B. Robins. Survival strategies of two small marine ciliates and their role in regulating bacterial community structure under experimental conditions. *Marine Ecology-Progress Series*, 33(1):59–70, 1986.

Venz, K. A., D. A. Hodell, C. Stanton, and D. A. Warnke. A 1.0 Myr record of Glacial North Atlantic Intermediate Water variability from ODP site 982 in the northeast Atlantic. *Paleoceanography*, 14(1):42–52, 1999. doi: 10.1029/1998PA900013.

Vidal, L., R. R. Schneider, O. Marchal, T. Bickert, T. F. Stocker, and G. Wefer. Link between the North and South Atlantic during the Heinrich events of the last glacial period. *Climate Dynamics*, 15(12):909–919, 1999. doi: 10.1007/s003820050321.

Waelbroeck, C., A. Paul, M. Kucera, A. Rosell-Melee, M. Weinelt, R. Schneider, A. C. Mix, A. Abelmann, L. Armand, E. Bard, S. Barker, T. T. Barrows, H. Benway, I. Cacho, M. T. Chen, E. Cortijo, X. Crosta, A. de Vernal, T. Dokken, J. Duprat, H. Elderfield, F. Eynaud, R. Gersonde, A. Hayes, M. Henry, C. Hillaire-Marcel, C. C. Huang, E. Jansen, S. Juggins, N. Kallel, T. Kiefer, M. Kienast, L. Labeyrie, H. Leclaire, L. Londeix, S. Mangin, J. Matthiessen, F. Marret, M. Meland, A. E. Morey, S. Mulitza, U. Pflaumann, N. G. Pisias, T. Radi, A. Rochon, E. J. Rohling, L. Sbaffi, C. Schafer-Neth, S. Solignac, H. Spero, K. Tachikawa, and J. L. Turon. Constraints on the magnitude and patterns of ocean cooling at the Last Glacial Maximum. *Nature Geoscience*, 2(2):127–132, 2009.

Wanninkhof, R. and W. R. McGillis. A cubic relationship between air-sea CO_2 exchange and wind speed. *Geophysical Research Letters*, 26(13):1889–1892, 1999.

Wanninkhof, R., W. E. Asher, D. T. Ho, C. Sweeney, and W. R. McGillis. Advances in Quantifying Air-Sea Gas Exchange and Environmental Forcing. *Annual Review of Marine Science*, 1:213–244, 2009.

Weber, S. L., S. S. Drijfhout, A. Abe-Ouchi, M. Crucifix, M. Eby, A. Ganopolski, S. Murakami, B. L. Otto-Bliesner, and W. R. Peltier. The modern and glacial overturning circulation in the Atlantic Ocean in PMIP coupled model simulations. *Climate of the Past*, 3(1):51–64, 2007. doi: 10.5194/cp-3-51-2007.

Wilson-Finelli, A., G. T. Chandler, and H. J. Spero. Stable isotope behavior in paleoceanographically important benthic foraminifera: Results from microcosm culture experiments. *Journal of Foraminiferal Research*, 28(4):312–320, 1998.

Winguth, A. M. E., D. Archer, J. C. Duplessy, E. Maier-Reimer, and U. Mikolajewicz. Sensitivity of paleonutrient tracer distributions and deep-sea circulation to glacial boundary conditions. *Paleoceanography*, 14(3):304–323, 1999. doi: 10.1029/1999PA900002.

Winn, K., M. Sarnthein, and H. Erlenkeuser. δ^{18}O stratigraphy and chronology of Kiel sediment cores from the East Atlantic. Kiel, 1991.

Wolf-Gladrow, D. A., J. Bijma, and R. E. Zeebe. Model simulation of the carbonate chemistry in the microenvironment of symbiont bearing foraminifera. *Marine Chemistry*, 64(3):181–198, 1999.

Wollenburg, J. E., W. Kuhnt, and A. Mackensen. Changes in Arctic Ocean paleoproductivity and hydrography during the last 145 kyr: The benthic foraminiferal record. *Paleoceanography*, 16 (1):65–77, 2001. doi: 10.1029/1999PA000454.

Woodruff, F., S. M. Savin, and R. G. Douglas. Biological fractionation of oxygen and carbon isotopes by recent benthic foraminifera. *Marine Micropaleontology*, 5(1):3–11, 1980. doi: 10.1016/0377-8398(80)90003-1.

Yu, J. M., H. Elderfield, and A. M. Piotrowski. Seawater carbonate ion-δ^{13}C systematics and application to glacial-interglacial North Atlantic ocean circulation. *Earth and Planetary Science Letters*, 271(1-4):209–220, 2008. doi: 10.1016/j.epsl.2008.04.010.

Zabel, M., T. Bickert, and L. Dittert. Significance of the sedimentary Al:Ti ratio as an indicator for variations in the circulation patterns of the equatorial North Atlantic. *Paleoceanography*, 14(6):789–799, 1999. doi: 10.1029/1999PA900027.

Zahn, R. and R. Keir. Tracer-nutrient correlations in the upper ocean: observational and box model constraints on the use of benthic foraminiferal δ^{13}C and Cd/Ca as paleo-proxies for the intermediate-depth ocean. In R. Zahn, T. F. Pedersen, M. A. Kaminski, and L. Labeyrie, editors, *Carbon Cycling in the Glacial Ocean: Constraints on the Ocean's role in Global Change*, pages 195–221. Springer-Verlag, 1994.

Zahn, R. and A. Stüber. Suborbital intermediate water variability inferred from paired benthic foraminiferal Cd/Ca and δ^{13}C in the tropical West Atlantic and linking with North Atlantic

climates. *Earth and Planetary Science Letters*, 200(1-2):191–205, 2002. doi: 10.1016/S0012-821X(02)00613-1.

Zahn, R., K. Winn, and M. Sarnthein. Benthic foraminiferal δ^{13}C and accumulation rates of organic carbon: *Uvigerina peregrina* group and *Cibicidoides wuellerstorfi*. *Paleoceanography*, 1(1):27–42, 1986. doi: 10.1029/PA001i001p00027.

Zahn, R., M. Sarnthein, and H. Erlenkeuser. Benthic isotope evidence for changes of the Mediterranean outflow during the Late Quaternary. *Paleoceanography*, 2(6):543–559, 1987. doi: 10.1029/PA002i006p00543.

Zarriess, M. and A. Mackensen. Testing the impact of seasonal phytodetritus deposition on δ^{13}C of epibenthic foraminifer *Cibicidoides wuellerstorfi*: A 31,000 year high-resolution record from the northwest African continental slope. *Paleoceanography*, 26:8, 2011.

Zeebe, R. E.. Modeling CO_2 chemistry, δ^{13}C, and oxidation of organic carbon and methane in sediment porewater: Implications for paleo-proxies in benthic foraminifera. *Geochimica Et Cosmochimica Acta*, 71(13):3238–3256, 2007.

Zeebe, R. E. and D. Wolf-Gladrow. *CO_2 in seawater: equilibrium, kinetics, isotopes*, volume 65 of *Elsevier Oceanography Series*. Elsevier, 2001.

Zeebe, R. E., J. Bijma, and D. A. Wolf-Gladrow. A diffusion-reaction model of carbon isotope fractionation in foraminifera. *Marine Chemistry*, 64(3):199–227, 1999. doi: 10.1016/S0016-7037(99)00091-5.

Appendix A

List of abbreviations and geological time periods

AABW Antarctic Bottom Water

AAIW Antarctic Intermediate Water

ACC Antarctic Circumpolar Current

AMOC Atlantic meridional overturning circulation

CB basic glacial model scenario based on CLIMAP reconstructions

CLIMAP Climate Long Range Investigation, Mapping, and Prediction

COSMOS Community Earth System Models

CS glacial model scenario based on CLIMAP reconstructions with altered fresh water balance in the Southern Ocean

DIC Dissolved inorganic carbon

ECHAM European Centre for Medium-Range Weather Forecasts/Hamburg atmospheric general circulation model

Eemian Previous Interglacial, ca. 130,000 - 114,000 years ago

Eocene 55.8 to 33.9 million years ago

FCM foraminifera calcification model

GB basic glacial model scenario based on GLAMAP reconstructions

GEOSECS Geochemical Ocean Sections Study

GLAMAP Glacial Atlantic Ocean Mapping

GLODAP Global Ocean Data Analysis Project

GNAIW Glacial North Atlantic Intermediate Water

GS glacial model scenario based on GLAMAP reconstructions with altered fresh water balance in the Southern Ocean

HAMOCC Hamburg Oceanic Carbon Cycle circulation model

Holocene Present Interglacial, the last 10,000 years

IPCC Intergovernmental Panel on Climate Change

LGM Last Glacial Maximum, 23,000 - 19,000 years ago

LH Late Holocene

LSG Large Scale Geostrophic ocean general circulation model

MARGO Multiproxy Approach for the Reconstruction of the Glacial Ocean Surface

Miocene 23.0 to 5.3 million years ago

MOW Mediterranean Outflow Water

NADW North Atlantic Deep Water

OGCM ocean general circulation model

PETM Palaeocene-Eocene Thermal Maximum, ca. 55 million years ago

PF Polar Front

Pleistocene 2.6 to 0.01 million years ago

Pliocene 5.3 to 2.6 million years ago

PMIP Paleoclimate Modelling Intercomparison Project

POC Particulate organic carbon

SAF Sub-Antarctic Front

SSS sea surface salinity

SST sea surface temperature

STF Sub-tropical Front

TA total alkalinity

WHP World ocean circulation experiment Hydrographic Programme

Appendix B

Supplementary material for Chapter 7

The auxiliary material consists of five figures. They contain zonal sections for the control and LGM runs in the North Atlantic (Figure B.1a, B.1c, B.3) and South Atlantic (Figure B.1b, B.1d, B.3), $\delta^{13}C_{as}$ plots (Figure B.4), and $\delta^{13}C$ scatter plots comparing various datasets and model output (Figure B.5).

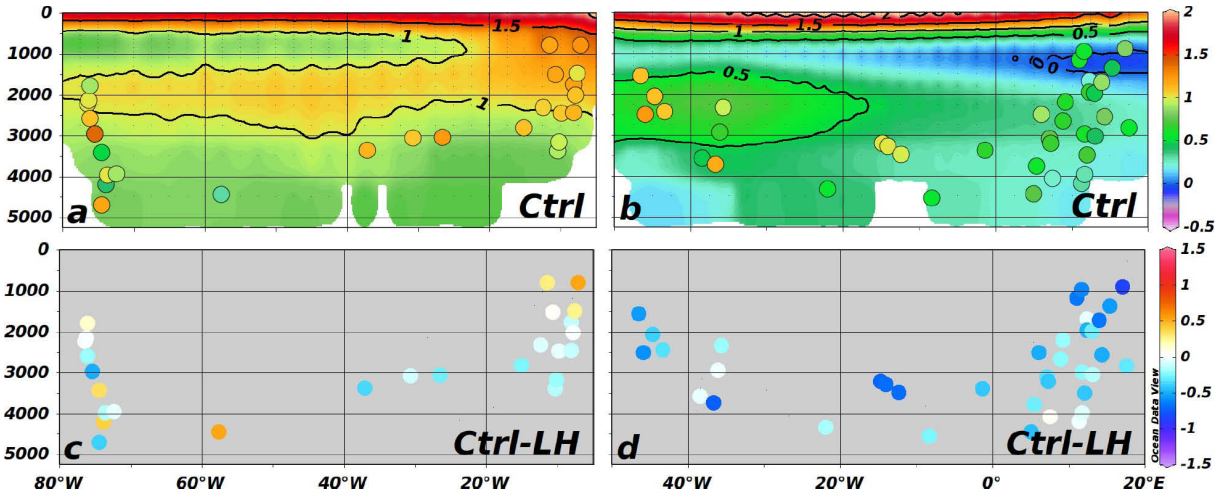

Figure B.1: Control run with Late Holocene $\delta^{13}C$ sediment core data overlay for the North Atlantic (a), and the difference in $\delta^{13}C$ between the control run and sediment values (c). (b, d) like in (a, c) along the South Atlantic section. Positive numbers in (c, d) indicate model $\delta^{13}C_{DIC}$ values that are higher than sediment $\delta^{13}C_{foram}$ values.

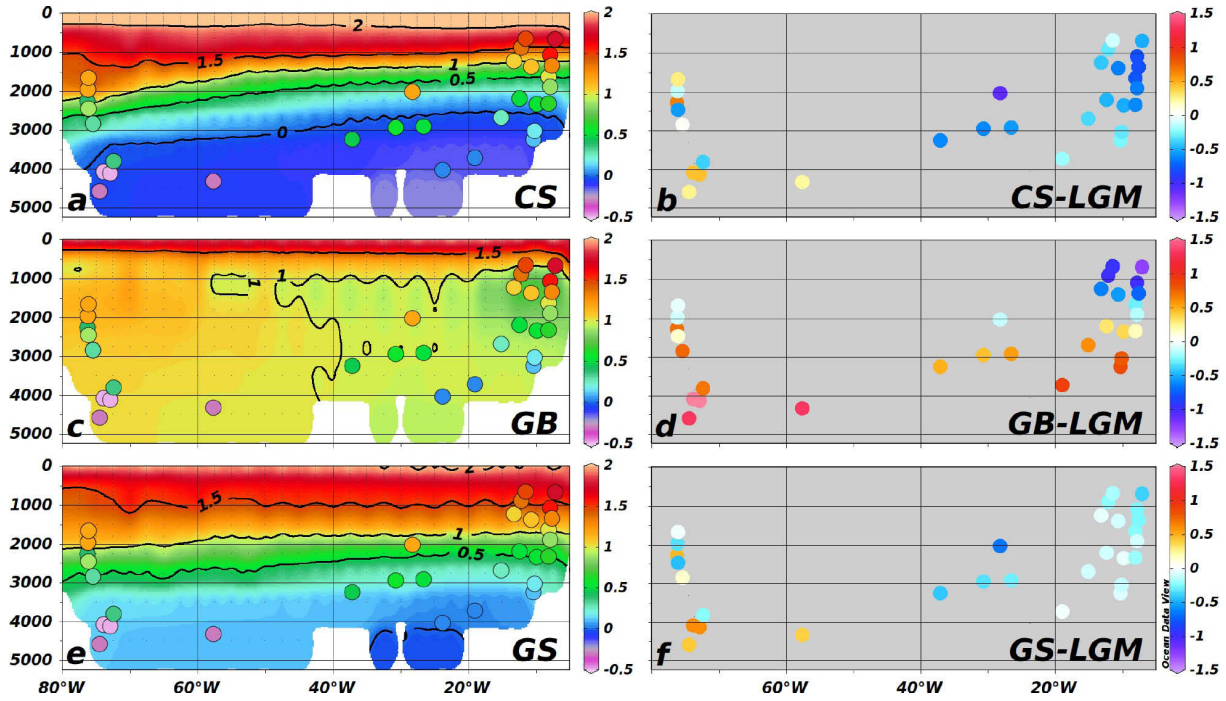

Figure B.2: North Atlantic section: CS δ^{13}C with LGM δ^{13}C sediment data overlay (a), and model-data differences (b). In (b): Positive numbers indicate model δ^{13}C values that are higher than sediment δ^{13}C values. (c, d) and (e, f) like in (a, b), but for model runs GB and GS

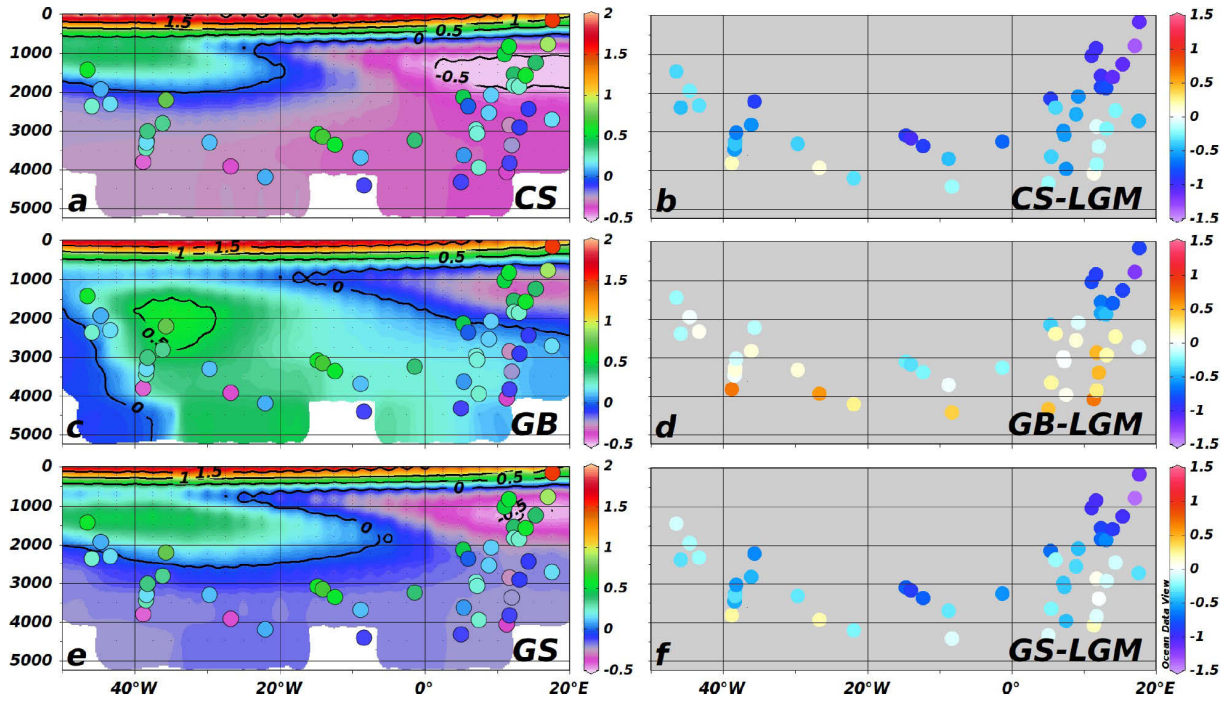

Figure B.3: Like Figure B.2, but along the South Atlantic section.

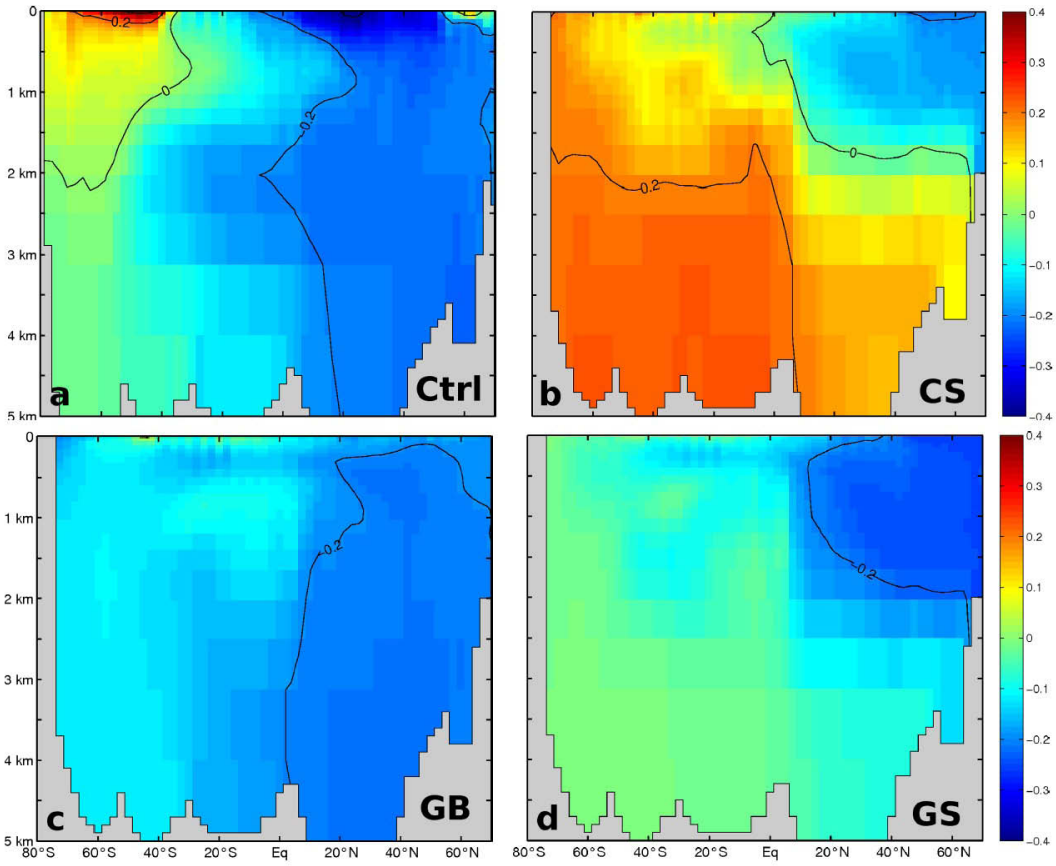

Figure B.4: $\delta^{13}C_{as}$ plots for the control run (a) and the LGM scenarios CS (b), GB (c), and GS (d).

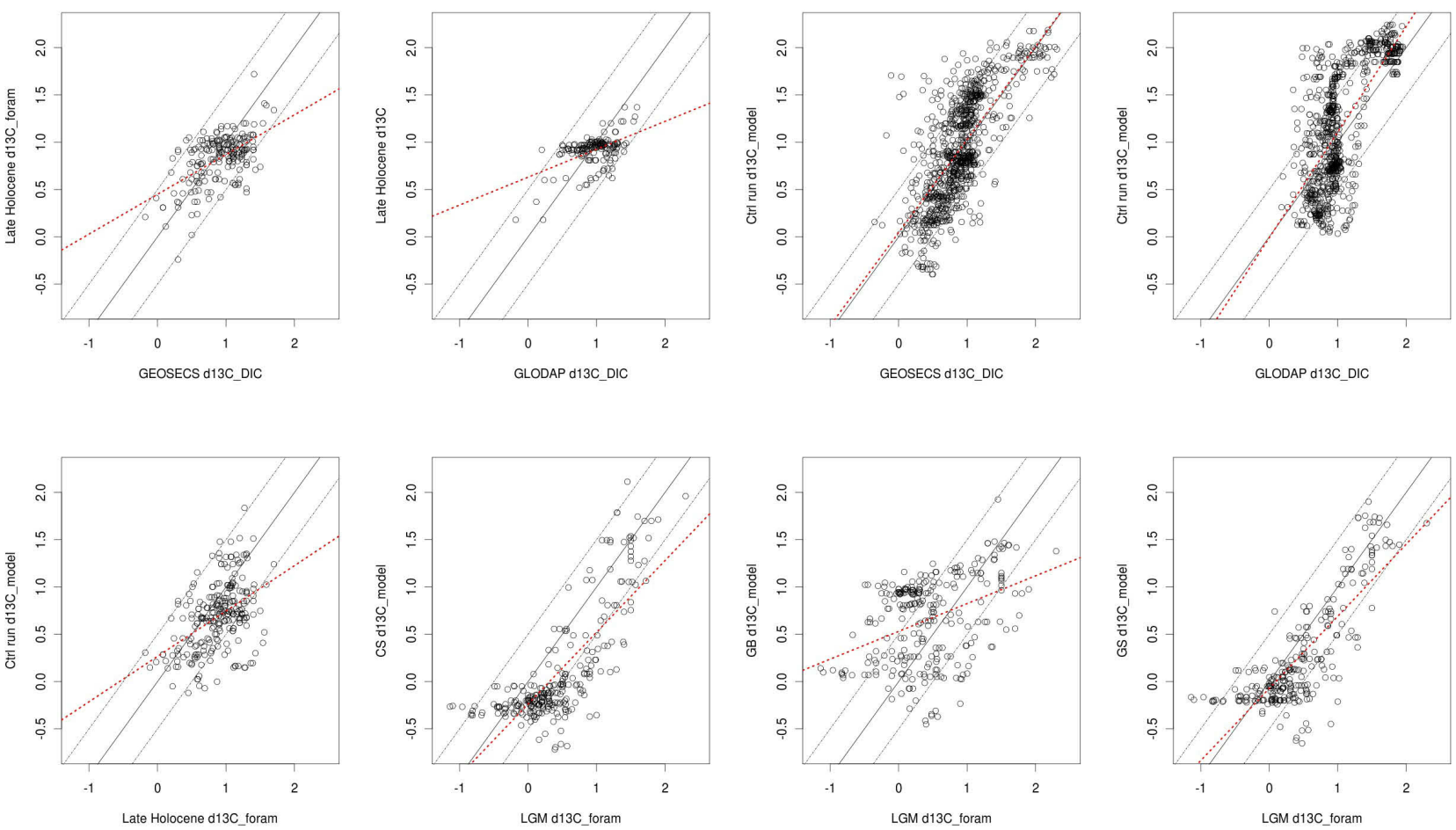

Figure B.5: δ^{13}C scatter plots for eight different data-data or model-data comparisons: the top row shows the relation of the two DIC measurement campaigns/compilations GEOSECS and GLODAP to Late Holocene foraminiferal data as well as the control run. The bottom row shows the relation between control run and Late Holocene δ^{13}C (bottom row, left), and the relation between the different LGM scenarios and LGM $\delta^{13}C_{foram}$ (bottom row, three right hand side plots).